LIQUID CRYSTAL SHUTTERED PASSIVE INFRARED SENSORS FOR TRUE PRESENCE DETECTION

A Dissertation

by

LIBO WU

Submitted to the Office of Graduate and Professional Studies of
Texas A&M University
in partial fulfillment of the requirements for the degree of

DOCTOR OF PHILOSOPHY

Chair of Committee,	Ya Wang
Committee Members,	M Cynthia Hipwell
	Xia Hu
	James E. Hubbard, Jr.
Head of Department,	Andreas Polycarpou

May 2021

Major Subject: Mechanical Engineering

ABSTRACT

PIR sensors, known as motion detectors, are widely used for moving occupancy detection. Made of pyroelectric materials, such as $LiTaO_3$, generating pyroelectric current when the received infrared radiation changes, PIR sensors only respond to the motion of occupants. This results in frequent false negative detections when stationary occupancy detection is also desired, such as occupancy-based building lighting control.

To enable stationary occupancy detection, in this dissertation, we develop optical shutters to actively modulate the radiation received by the PIR sensors in the long-wave infrared (LWIR) region (8-12 μm) where human skin radiates the most. The optical shutter is made of polymer dispersed liquid crystal (PDLC) sandwiched by two germanium substrates. Each germanium substrate has an anti-reflected film on one side (the non-conductive side) to reduce the reflection.

The PDLC infrared shutter, a PIR sensor, and a driving circuit forms a synchronized low-energy electronically chopped PIR (SLEEPIR) sensor module. To better improve its performance, we devised SLEEPIR sensor nodes, and formed a SLEEPIR sensor network system with advanced machine learning algorithms.

The main contributions of this dissertation include: (i) modeling the SLEEPIR output as a function of the effective modulation, the response time of the PDLC shutter, and the time constants of the PIR sensor; (ii) quantifying the impact of the driving voltage, the mass ratio, the cell gap, and the cooling rate on the effective modulation and the response time of the PDLC shutter to obtain the optimal driving voltage and fabrication

conditions that maximize SLEEPIR module's output; and (iii) experimental validation of the SLEEPIR sensor nodes for presence detection in the lab and uncontrolled environment settings.

DEDICATION

To my wife, my parents, and my sister

ACKNOWLEDGEMENTS

I want to express my gratitude to all those people who have helped me to accomplish this dissertation.

The most credit should go to my advisor, Dr. Ya Wang, for her guidance, support, encouragement, and the countless opportunities she afforded me. I feel so lucky to join her lab. I learned a lot from her to be an engineer and a researcher. Without her patience and support, I would not have successfully completed the graduate program.

I am thankful to my committee members, Dr. M Cynthia Hipwell, Dr. James E. Hubbard, Jr., and Dr. Xia Hu, for providing many thoughtful and constructive comments on this dissertation.

I want to thank Professor Shin-Tson Wu of the University of Central Florida for the help and kind guidance on liquid crystal materials.

I am thankful to my labmates and other friends for their comments, discussions, support, and inspirations: Zhangjie Chen, Rui Hua, Qijie Shen, Jingfan Chen, and Tianhao Yan.

I am deeply grateful to my wife Xiaoyu Li for her understanding and support. She is not only my wife but also a good friend, a listener, a supporter. We share joy and sadness in our lives. Without her encouragement, my research life will not be so enjoyable.

Finally, thanks to my parents and my sister for their selfless support during my study overseas.

CONTRIBUTORS AND FUNDING SOURCES

Contributors

This work was supervised by a dissertation committee consisting of Dr. Ya Wang, as the advisor, Dr. M Cynthia Hipwell, and Dr. James E. Hubbard, Jr. of the Department of Mechanical Engineering, and Dr. Xia Hu of the Department of Computer Science and Engineering.

The samples in Chapter 4 were partially prepared by Tianhao Yan of the Department of Chemistry. The software to construct the wireless sensor network in Chapter 5 was provided by Qijie Shen of the Department of Electrical and Computer Engineering.

All other work conducted for the dissertation was completed by the student independently.

Funding Sources

This research was supported funded by DOE ARPAE DE-AR0000531 (2015-2018) and DE-AR0000945 (2018-2022).

TABLE OF CONTENTS

Page

LIST OF FIGURES

Page

LIST OF TABLES

Page

1. INTRODUCTION

1.1. Background and Motivation

1.1.1. Occupancy Detection

Occupancy detection is essential for power usage management in commercial and residential buildings. For instance, accurate occupancy information for lighting, heating, ventilation, and air-conditioning (HVAC) systems can reduce energy consumption and preserve user comfort [1-4].

There are two types of occupancy detection systems: terminal-based and non-terminal-based [5]. Terminal-based detection systems need a terminal such as a mobile phone [6] or radio frequency identification tag [4]. Such terminals should be carried by the occupant, resulting in high deployment costs, privacy invasions, and inconveniences.

Non-terminal based systems utilize remote occupancy sensors, such as passive infrared (PIR) sensors [7-17], carbon-dioxide (CO_2) sensors [18, 19], ultrasonic sensors [20, 21], image recording devices [22-24], thermopile array sensors [25, 26] or the combination of them. CO_2 sensors predict the occupancy presence and counting by measuring indoor gas concentration [18, 19]. Their accuracy is largely disturbed by environmental conditions such as sensor locations and airflow. Ultrasonic sensors predict the occupancy presence and location by measuring the echo intensity of the transmitted signal [20, 21]. However, they frequently report false positive detections due to the vibrations in the surrounding environment [20]. Image-based detection systems such as video cameras are also popularly used to detect occupancy presence, location,

identification and activity tracking [22-24]. However, their application is limited by environmental light, sensor position, cost, complicated signal processing process, and privacy invasions [27]. Thermopile array sensors, containing multiple thermopile point detectors, detect occupancy presence, localization, and facing direction [25, 26], by analyzing the received infrared radiation through Seebeck effect [28]. However, their application is restricted by their cost, detection range, and power consumption.

1.1.2. PIR Sensors

The PIR sensor typically has two or four sensing elements, made of pyroelectric materials, such as $LaTiO_3$ [7, 29]. Each sensing element has an opposite polarization to its neighboring one. Take a PIR sensor with four sensing beams as an example. As shown in Figure 1.1, when a person moves into its field of view (FOV), the incident infrared radiation received by each sensing element changes due to motion. The resulted temperature change of the sensing elements will generate a pyroelectric current. The pyroelectric current could be converted to a voltage signal with an amplifier. The detailed working principle of PIR sensors can be found in Chapter 2.1. There are two types of PIR sensors on the market, digital PIR sensors and analog PIR sensors. The digital PIR sensor has a comparator behind the amplifier so that once the voltage signal exceeds a certain level, the sensor will fire a high digital signal. The analog PIR sensors utilize several stages of amplifiers to convert the small pyroelectric current (several pA) to a voltage signal that could be collected by other devices, such as analog-digital converters (ADC).

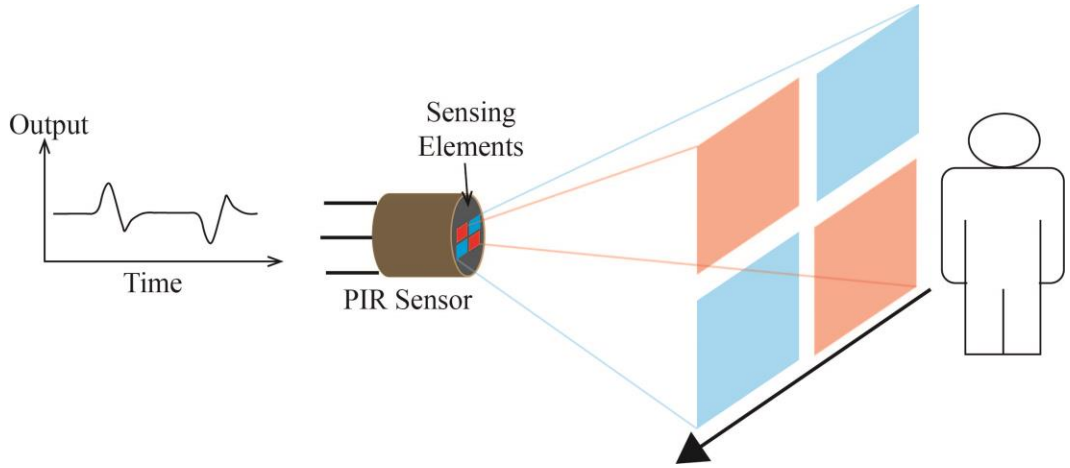

Figure 1.1 The operation principle of a PIR sensor.

As motion detectors, PIR sensors are widely used for moving occupancy detection in door automation [30, 31], security surveillance [32, 33], lighting [34], or HVAC [35, 36] control. Lately, the literature also explores their applications in indoor occupancy tracking [13, 14] and positioning [12, 37] due to some obvious advantages of PIR sensors: (i) low cost, large pyroelectric coefficient, and great chemical stability [38], (ii) high responsivity to long-wave infrared radiation from the human skin (8-12μm) [39-41], (iii) the output signal (analog) is proportional to the received LWIR infrared radiation [42-44], and (iv) the FOV is large and controllable.

The major bottleneck PIR sensors are currently facing is that they could not detect stationary occupants, which limits their applications that require accurate occupancy information, such as indoor lighting and/or HVAC control [1, 45]. According to the survey conducted by the United States Department of Labor, for an average of 11.7 hours per day,

the occupancy state of a full-time employee is considered stationary [46]. As aforementioned, as motion detectors, PIR sensors could not detect stationary status, such as lying, sitting, or standing, without noticeable movements [1, 47]. This results in frequent false-negative detection of current PIR sensors used in building lighting control. For example, the light will turn off in modern offices when the occupant inside is not moving for a while, typically 15 – 30 mins. This leads to uncomfortable light swings, energy waste, and shortened lifetime of the equipment.

1.1.3. Optical Shutters and the SLEEPIR Sensor Module

The motivation of this dissertation is to extend the functionality of the PIR sensor to detect both stationary and moving occupants. The infrared radiation emitted by stationary occupants does not change and thus cannot be detected by PIR sensors. However, if we introduce an optical shutter to actively change its transmission so that the radiation received by the PIR sensor is changing, this will enable the detection of stationary occupants. This is the basic working principle of our synchronized low-energy electronically chopped PIR (SLEEPIR) sensor module, as shown in Figure 1.2.

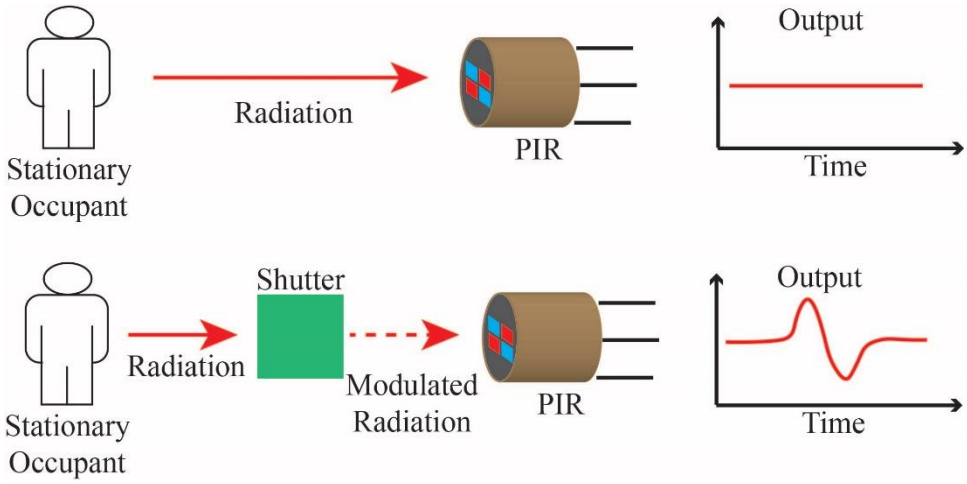

Figure 1.2 The optical shutter enables the detection of stationary occupants. Top: existing PIR sensor. Bottom: SLEEPIR sensor module.

The bottom line is that the SLEEPIR sensor module should still be able to detect moving occupants. The transmission rate of the optical shutter needs to be highly tunable and stays high in the LWIR region. Some researchers, including our group, developed mechanical shutters as LWIR optical shutters [43, 44, 48-51], which will be reviewed in Chapter 2.2. Their high-power consumption, noise level, size, and reliability limit their practical applications. Thus, in this dissertation, we developed LWIR liquid crystal shutters for the SLEEPIR sensor module.

1.2. LWIR Liquid Crystal Shutters

Liquid crystal (LC) is a thermodynamic phase of a condensed matter between the conventional liquid and the solid crystal [52]. LC material has the optically anisotropic property and shows birefringence. An external electrical field can change the direction of the LC molecules and thus impacts the propagation of the light transmitted through the

LC material. If we define its ordinary refractive index as n_o and its extraordinary refractive index as n_e, their birefringence can be defined as:

$$\Delta n = n_e - n_o \tag{1.1}$$

Due to this unique electro-optical property in response to an external electrical field, LC materials are widely used in displays [53] and spatial light modulators [54] [55]. In particular, many researchers have investigated LC with high birefringence in the LWIR region, which can be potentially used to fabricate LWIR LC shutters for the SLEEPIR sensor module. These LWIR LC materials can be grouped in two categories based on the light transmission modes. The first is the transmissive mode based, which includes the retardation effect based twisted nematic LC (TNLC) [56], and the anisotropic absorption LC (AALC) [57]. The second category is the trans-reflective mode based, which includes the scattering mode and the reflection mode. Among them, polymer dispersed LC (PDLC) utilizes the scattering effect when the LC and the polymer's refractive indices are different [58, 59]. Ferroelectric LC (FLC) with a large dipole also utilizes the scattering effect when the external field switches the direction. Cholesteric LC (CLC) utilizes the Bragg effect to reflect the light with a specific wavelength according to the chiral pitch of the LC in the cell. The comparison of these LWIR LC materials is shown in Table 1.1.

The transmission difference in Table 1.1 is calculated by subtracting the transmission rate at λ=10μm of the OFF state from that of the ON state. Here, the ON and the OFF states represent the states when the LWIR LC shutter has the higher transmission rate and the lower transmission rate, respectively. Among all these potential LWIR LC

material candidates, PDLC material has the advantage of low cost, high transmission difference, and relatively simple fabrication process.

Table 1.1 LWIR LC material candidates.

Liquid Crystal Type	Properties	Reference
TNLC	• Low transmission difference (12%) • Low transmission rate (<40% even in the ON state) • LWIR polarizers required and thus high cost to fabricate the shutter • Large cell gap (46 μm) and thus long response time in LWIR (4 seconds)	[56, 60-63]
FLC	• Low transmission difference (6%-8%) • High driving voltage (>25V)	[64, 65]
CLC	• Narrow wave band (9.5-10.5 μm) • Low transmission difference (11%) • Complicate fabrication process	[66]
AALC	• No commercialized LC material • Low transmission difference (10%)	[57]
PDLC	• No polarizers required and thus low cost • High transmission difference (~20%)	[67, 68]

In Chapter 2.2.4, effective modulation, which reflects the difference of the transmitted radiation, will be introduced to better characterize the property of the PDLC shutters compared to the transmission difference at the wavelength of $10\mu m$.

In this dissertation, the property and application of the PDLC shutters will be studied.

1.3. Scope and Objectives of the Dissertation

As shown in Figure 1.3, the SLEEPIR sensor module consists of a PDLC shutter, a driving circuit, and a PIR sensor. The PDLC shutter consists of the PDLC material sandwiched between two germanium (Ge) substrates. Each Ge substrate has an anti-reflected film on one side (inner side, non-conductive side) to reduce the reflection as Ge has a high refractive index [69]. A pulse-width-modulation (PWM) driving circuit controls the transmission of the PDLC shutter to modulate the radiation received by the PIR sensor.

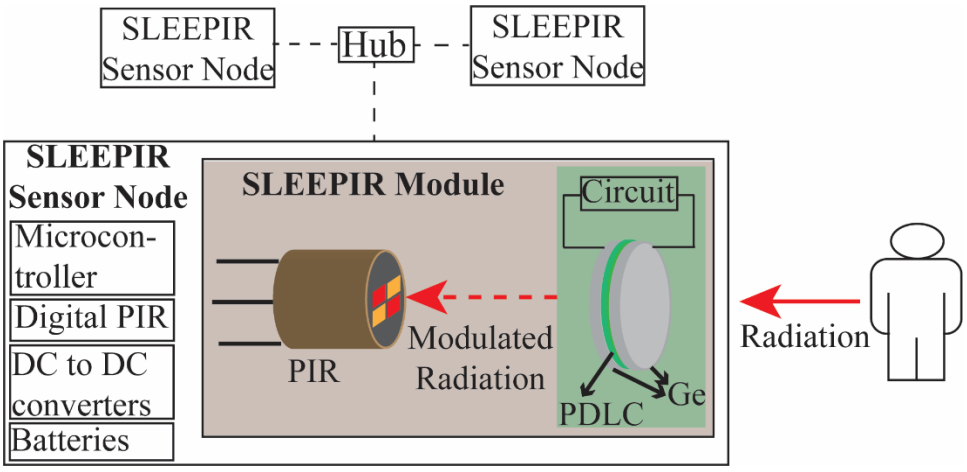

Figure 1.3 The proposed SLEEPIR sensor system for presence detection.

A SLEEPIR sensor node is made of a SLEEPIR sensor module, a digital PIR sensor, a microcontroller unit (MCU), batteries, and direct current (DC) to DC converters. Adding a digital PIR sensor is to reduce the energy consumption and to increase the detection accuracy during the sleep stage. The sensor node will not only periodically wake

up and drive the SLEEPIR module to detect the stationary occupants, but also wake up by the motion detected by the digital PIR sensor. The DC-to-DC converters on the sensor node convert the voltage to the desired level. Multiple SLEEPIR sensor nodes and a hub form a wireless sensor network. The central hub is used to collect the data from each sensor node. Using fixed threshold values from the PIR sensors to detect occupancy status is a widely used method [16, 70, 71]. However, using the threshold value determined from one dataset on another dataset will lead to low performance due to the environmental change. Machine learning approach could help to improve the detection accuracy by analyzing the statistical features of the signals. When the environment factors change significantly, adaptively calibrating the output of the SLEEPIR module, which is related to the environmental temperature, will also have a high accuracy.

The main objective of this dissertation is to systematically study the factors that impact the effective modulation and the response time of the PDLC infrared shutters, and thus impact the SLEEPIR module's output. In the end, the performance of the SLEEPIR sensor system is evaluated in both controlled and uncontrolled environmental settings.

In Chapter 2, we model the output of an analog PIR sensor as a function of sinusoidally modulated infrared radiation. The development of mechanical shutters from our group are reviewed, including the chopped PIR sensor (C-PIR) [51], the rotational chopped PIR sensor (Ro-PIR) [43], and the Lavet motor-driven PIR sensor (LAMPIR) [44]. The working principles of TNLC, FLC, CLC, AALC, and PDLC are introduced and compared. PDLC infrared shutters are chosen for the SLEEPIR sensor module due to the high modulation. Compared to references in the literature [67, 68], we improve the

contrast ratio and the transmission difference of our PDLC shutters by 16% and 165%, respectively. Finally, the fabrication process of the PDLC shutters is described.

In Chapter 3, the SLEEPIR sensor module is devised and characterized. Its output is theoretically modeled as a function of the effective modulation and the response time of a PDLC shutter, and the time constants of the PIR sensor. The time constants of the analog PIR sensor are calculated by measuring the frequency response of the PIR sensor. Finally, the effective modulation and response time of the PDLC shutters are defined and characterized.

In Chapter 4, our goal is to find the optimal fabrication and driving conditions of the PDLC shutters that optimize the SLEEPIR sensor module's output. Firstly, we study the morphology of glass based PDLC shutters via microscope images. The results show that at the same mass ratio, the droplet size will increase with a slower cooling rate. At the same cooling rate, the droplet size will increase when the mass ratio increases. Secondly, we systematically study the impact of the driving amplitude, the driving frequency, and the fabrication conditions on the effective modulation of the PDLC shutters. The effective modulation represents the difference of the transmitted radiation before and after removing the applied driving voltage. The effective modulation will increase with larger voltage amplitude until reaching the saturation level. Then, due to the dielectric property of the PDLC shutter, the optimal driving frequency is found to be below than 980Hz. With the same driving condition, the fabrication condition, including cell gap, mass ratio, and cooling rate, is discussed. The optimal fabrication condition that maximizes the effective modulation is $\eta = 0.8$, $d = 22\mu m$ at the cool rate between 1 and 1.25°C/min. The study

on the cycling effect shows that cycling could help reduce the hysteresis, the persistence and/or the semi-permanent persistence (memory effect). Thirdly, the response time is studied. The results show that the rising time will decrease with the increased voltage amplitude, while the decay time τ_d does not have obvious changes. The impact of the fabrication condition on the response time is also studied systematically, which shows that when the cell gap *d* and the mass ratio η increases, the response time will increase. A faster cooling rate will decrease the response time. Fourthly, several PDLC shutters are fabricated under different conditions to verify the theoretical model of the SLEEPIR sensor module described in Chapter 3. Meanwhile, the optimal fabrication condition that generates the highest voltage amplitude is still $\eta = 0.8$, $d = 22\mu m$ at the cool rate between 1 and 1.25°C/min. Finally, the lifetime of the PDLC shutters is discussed. The result shows that the output of the SLEEPIR sensor module is stable after more than 250,000 cycles, which represents five years of usage if the measurement period is every 10 minutes.

In Chapter 5, we developed the SLEEPIR sensor node consisting of a SLEEPIR sensor module, a traditional motion sensor, an MCU, and related electronics. The power consumption is 95% reduced compared to mechanical shutter prototypes. Next, lab tests are performed where the occupants perform activities under instructions. In the end, uncontrolled tests are carried out where no instructions are provided, and environmental factors are considered. The machine learning model is applied for controlled experiments, which shows an average accuracy of 99.38%, 2.67% higher than that using the traditional threshold method. For uncontrolled experiments, the thermal transfer model of the

SLEEPIR sensor module is developed, considering environmental factors. An adaptive detection algorithm is introduced to improve the detection accuracy further. The results show that the adaptive detection algorithm reaches an accuracy of 97.8%, which is 28.66% and 35.46% higher than that using a stand-alone PIR sensor and that using the SLEEPIR sensor module with a fixed threshold, respectively. Finally, the proposed SLEEPIR sensor system is compared with commercial products.

Chapter 6 summarizes the result of the dissertation, which shows the feasibility and high potential of using the SLEEPIR sensor system for building occupancy detection.

2. RELATED WORK[*†‡§**]

This chapter starts with introducing the working principle of the PIR sensor and the mechanically chopped PIR sensors. Then, we reviewed and compared the working principles of different types of LWIR LC infrared shutters.

2.1. Working Principle of the PIR Sensor

2.1.1. The Pyroelectric Effect

As shown in Figure 1.1, PIR sensors detect moving occupants based on the pyroelectric effect. The pyroelectric effect, or pyroelectricity, refers to the change of internal polarization of a material due to small changes in heat flux [7]. As shown in Figure 2.1, if the pyroelectric material has a temperature change due to the incident radiation variation it has received, an electrical charge will be released at the surface of this pyroelectric material.

---

[*] Part of this chapter is reprinted from "Turning a pyroelectric infrared motion sensor into a high-accuracy presence detector by using a narrow semi-transparent chopper" by H. Liu, Y. Wang, K. Wang, and H. Lin, 2017. *Applied Physics Letters*, vol. 111, no. 24, p. 243901, with the permission of AIP Publishing.

[†] Part of this chapter is reprinted, with permission, from L. Wu, Y. Wang, and H. Liu, "Occupancy detection and localization by monitoring nonlinear energy flow of a shuttered passive infrared sensor", *IEEE Sensors Journal*, vol. 18, no. 21, pp. 8656-8666, 2018. Copyright © 2018 IEEE.

[‡] Part of this chapter is reprinted, with permission, from L. Wu, and Y. Wang, "A Low-power electric-mechanical driving approach for true occupancy detection using a shuttered passive infrared sensor", *IEEE Sensors Journal*, vol. 19, no. 1, pp. 47-57, 2019. Copyright © 2019 IEEE.

[§] Part of this chapter is reprinted, with permission, from L. Wu, F. Gou, S-T. Wu, and Y. Wang, "SLEEPIR: Synchronized low-energy electronically chopped PIR sensor for true presence detection", *IEEE Sensors Letters*, vol. 4, no. 3, pp. 1-4, 2020. Copyright © 2020 IEEE.

[**] Part of this chapter is reprinted with permission, from L. Wu, Y. Wang, "True Presence Detection via Passive Infrared Sensor Network Using Liquid Crystal Infrared Shutters", *Proceedings of the ASME 2020 Conference on Smart Materials, Adaptive Structures and Intelligent Systems*, 2020.

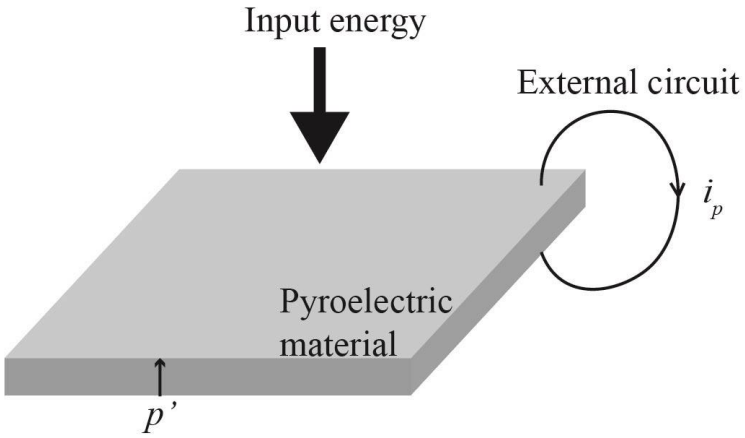

Figure 2.1 The pyroelectric material shows a flow of current due to the temperature change.

Since the pyroelectric element in the PIR sensor is very thin, if the pyroelectric coefficient perpendicular to its surface is denoted as p', which is the perpendicular component of the pyroelectric coefficient $\boldsymbol{p}$, then the current flow becomes

$$i_p = Ap' \frac{d\Theta}{dt} \tag{2.1}$$

where A is the surface area, and $d\Theta/dt$ is the temperature changing rate of the pyroelectric element. For most pyroelectric detectors, we could consider $p' = \boldsymbol{p}$.

2.1.2. The Output of the PIR Sensor

Consider the radiation power received by the PIR sensor is modulated at a frequency ω:

$$W(t) = W_0 e^{i\omega t} \tag{2.2}$$

Here, W_0 is the amplitude of the radiation power.

Consider the thermal transfer model of the pyroelectrical element of the PIR sensor, as shown in Figure 2.2(a). If its capacitance is C_E, emissivity is α, thermal capacity is H, its thermal conductance to its surroundings (heat sink) is G_T, and the temperature difference from the heat sink is $\Delta\Theta$, then the thermo-electrical analogy of this thermal transfer model is shown in Figure 2.2(b) [72].

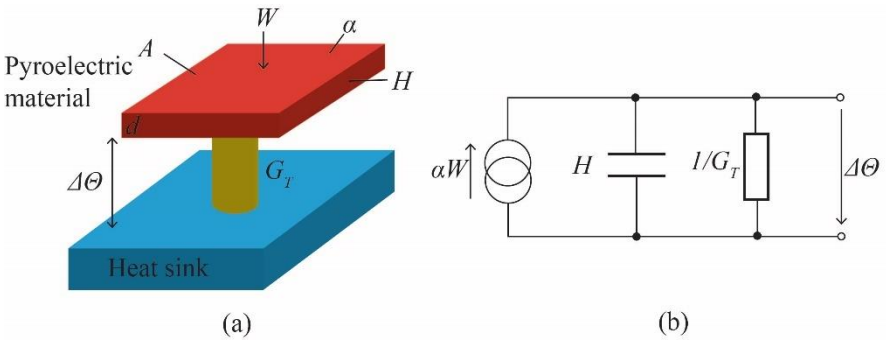

Figure 2.2 (a) The thermal transfer model of the pyroelectric element of the PIR sensor after exposure to the incident radiation power. (b) The equivalent thermo-electrical analogy of the thermal transfer model.

The received incident radiation αW functions as a current source. The thermal capacity H and the thermal conductance G_T are represented by a capacitor and a resistor, respectively. Then the temperature difference $\Delta\Theta$ is [7]

$$\Delta\Theta = \frac{\alpha W}{G_T} \cdot \frac{1}{\sqrt{1+\omega^2\tau_T^2}} \exp(i\omega t) \tag{2.3}$$

where $\tau_T = H/G_T$ represents the thermal time constant.

Substituting Equation (2.3) to Equation (2.1) leads to [7]

$$i_p(t) = Ap' \frac{\alpha W}{G_T} \frac{\omega}{\sqrt{1+\omega^2\tau_T^2}} \exp(i\omega t) \tag{2.4}$$

The current in Equation (2.4) is extremely low (several pA), and the source's impedance is high. Thus, a preamplifier with a high impedance is required to convert the current to voltage. The preamplifier circuit is shown in Figure 2.3.

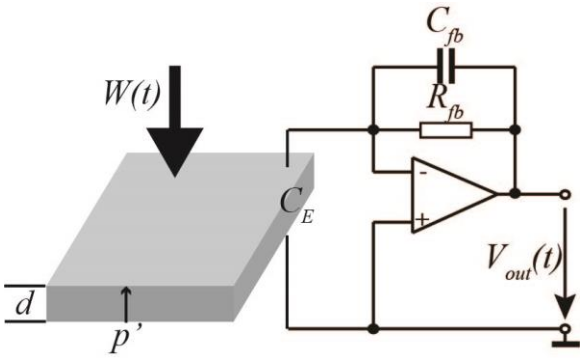

Figure 2.3 Preamplifier circuit of a passive infrared sensor.

For the circuit illustrated in Figure 2.3, R_{fb} and C_{fb} correspond to the feedback resistor and capacitor, respectively. Here, $\tau_E = R_{fb}C_{fb}$ represents the electrical time constant. The amplifier performs as a current-voltage converter. The relationship between the output current i_p, the temperature difference $\Delta\Theta$ between the sensing elements and the surrounding environment, the radiation power $W(t)$ and the output voltage $V_{out}(t)$ can be expressed as [7]:

$$\begin{cases} i_p(t) = Ap' \dfrac{d(\Delta\Theta)}{dt} \\ \alpha W(t) = H \dfrac{d(\Delta\Theta)}{dt} + G_T \Delta\Theta \\ V_{out}(t) = \dfrac{i_p(t)}{\dfrac{1}{R_{fb}} + i\omega C_{fb}} \end{cases} \tag{2.5}$$

By solving Equation (2.5), the output voltage of the preamplifier stage is:

$$V_{out}(t) = \frac{R_{fb}\alpha p' A i\omega e^{-i(\arctan \omega\tau_T + \arctan \omega\tau_E)}}{G_T(1+\omega^2\tau_T^2)^{1/2}(1+\omega^2\tau_{\mathrm{E}}^2)^{1/2}} W(t) \tag{2.6}$$

Equation (2.6) shows that there is a phase change between $V_{out}(t)$ and $W(t)$. If we only focus on the magnitudes, the output of the PIR sensor is:

$$V_{out}(t) = \frac{R_{fb}\alpha p' A\omega}{G_T(1+\omega^2\tau_T^2)^{1/2}(1+\omega^2\tau_{\mathrm{E}}^2)^{1/2}} W(t) \tag{2.7}$$

In Equation (2.7), once the modulation angular frequency ω is fixed, the output voltage of the preamplifier stage $V_{out}(t)$ is proportional to incident radiation.

Next, we simulate the frequency response of the amplitude of the pyroelectric current $i_p(t)$ and output voltage $V_{out}(t)$ of the PIR sensor using parameters and their values shown in Table 2.1. The values are from a handbook of InfraTec® [73].

Table 2.1 Parameters and their values used in the PIR sensor model.

Parameter	Value	Unit	Parameter	Value	Unit
$\boldsymbol{\alpha}$	1	N/A	τ_T	159	ms
$\boldsymbol{W_0}$	1	μW	τ_E	3	s
$\boldsymbol{G_T}$	1.95	mW/K	d	25	μm
$\boldsymbol{H}$	310	μWs/K	A	4	mm^2
$\boldsymbol{R_{fb}}$	24	GΩ	p'	17	$nC/cm^2/K$
$\boldsymbol{C_{fb}}$	125	pF			

The simulated result is shown in Figure 2.4, with the frequency range from 0.001Hz to 1kHz. The blue and orange curves represent the amplitudes of i_p and V_{out}, respectively. The pyroelectric current i_p shows the typical high pass characteristics. The cutoff frequency is $f_T = 1/2\pi\tau_T$, with the value of 1Hz. Above this frequency, i_p reaches the saturation value. Due to the addition of the amplifier, the amplitude of the output voltage V_{out} shows the band pass property, with the pass band being from $f_E = 1/2\pi\tau_E$ to $f_T = 1/2\pi\tau_T$. Within this range, the voltage value is flat.

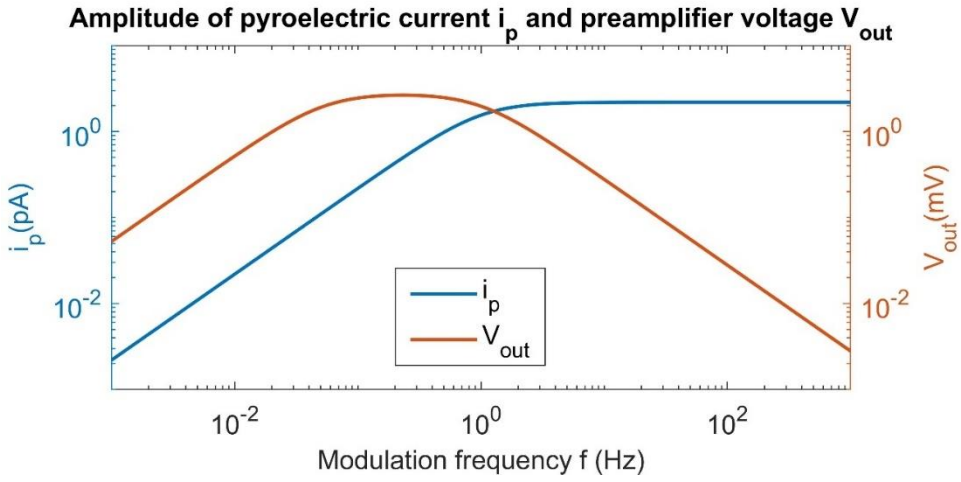

Figure 2.4 The simulated frequency response of pyroelectric current (left y-axis) and the preamplifier voltage (right y-axis).

If there is only one pyroelectric element in the PIR sensor, as long as the environmental temperature changes, even though the occupancy status, no matter occupied or unoccupied, is not changing, there will still be a voltage output. Therefore, all

commercialized PIR sensors, to our best knowledge, have an even number of pyroelectric elements to eliminate the environmental disturbances. The number of elements with a positive polarization is equal to those with a negative polarization.

2.2. LWIR Optical Shutters

From Equation (2.7), for traditional PIR sensors, the voltage output $V_{out}(t)$ is zero if the incident radiation is not changing, where $\omega = 0$. However, according to the survey conducted by the U.S. department of labor in 2018 [46], indoor occupants spend an average of 11.8h a day doing stationary activities, such as sleeping or sitting. This results in frequent false-negative detection of existing PIR sensors as they only respond to motion [1, 47]. This issue could be resolved by utilizing an LWIR optical shutter to modulate the incident radiation received by the PIR sensor, which is expressed in the form of Equation (2.2).

2.2.1. The Chopped PIR Sensor (C-PIR)

Using a mechanical optical shutter in front of a PIR sensor is not a new idea. In [48], the authors used a chopper in front of a PIR sensor as a thermometer. However, their work had not proved to be able to detect stationary occupants. Also, the detection range is limited to 50cm. In [74], Juan *et al.* used a camera iris shutter to control infrared radiation transmission. But the speed to shutter to close or open is fixed. Before we dive into the LC infrared shutter, there is some related work done by our group that uses mechanical shutters.

H. Liu *et al.* [51] from our research group use a semitransparent shutter in front of the PIR sensor, which is named as Chopped PIR (C-PIR) sensor. The shutter is made of

high-density polyethylene (HDPE). The shutter is driven by a servo motor and periodically shutter LWIR radiation across the FOV of the C-PIR, as shown in Figure 2.5.

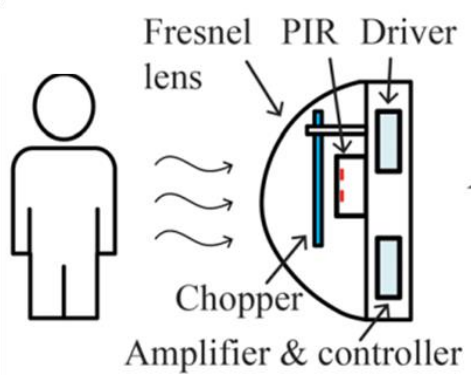

Figure 2.5 Schematic of the Chopped PIR sensor (C-PIR). Reprinted from [51], with the permission of AIP Publishing.

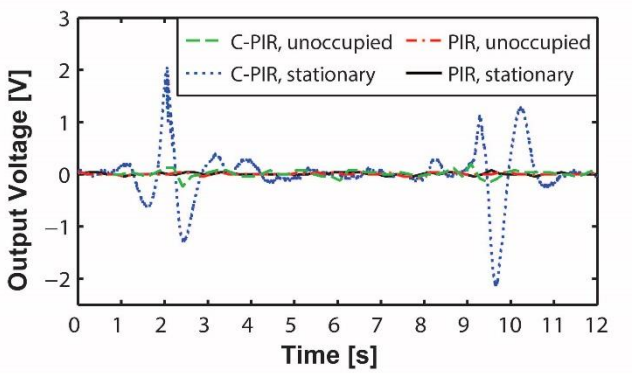

Figure 2.6 Output voltage waveforms induced by the C-PIR and its PIR counterpart when unoccupied and occupied by an occupant sitting at 1m away, at the chopping period of 7 s. Reprinted from [51], with the permission of AIP Publishing.

Figure 2.6 shows the output voltage of the PIR sensor when the HDPE shutter is rotating at the chopping period of 7 seconds. The blue dotted line is the output signal when there is a stationary occupant before the C-PIR. The polarity peaks generated show a higher magnitude than the unoccupied scenario. The authors use this magnitude (also known as peak-to-peak values) to classify the presence status. When placing the C-PIR on a desk and facing front, the C-PIR could maintain the accuracy of 100% within the range of 8 m.

2.2.2. The Rotational Chopped PIR Sensor (Ro-PIR)

In [43], I modified the way how the mechanical shutter rotates. Unlike C-PIR, Ro-PIR rotates the optical shutter around the center of the PIR sensor, as shown in Figure 2.7. This work reports that the Ro-PIR sensor, a stand-alone smart sensor node that uses an HDPE shutter to monitor infrared energy flow received by a traditional PIR sensor for localization, tracking, and facing direction detection.

Figure 2.8 illustrates the structure and diagram of the Ro-PIR sensor, respectively. An Arduino Nano MCU is powered by a 6V, 3W solar panel, and a Lithium-ion rechargeable battery. The MCU powers a stepper motor (28-BYJ48), a PIR sensor (PaPIR® AMN24112, Panasonic), and a Bluetooth module (HC-06) via the output pin. The HDPE shutter is attached to a ball bearing driven by the stepper motor and rotates periodically. The PIR sensor is placed at the center of the ball bearing. The MCU samples the analog signals of the PIR sensor through an ADC and sends data to a computer by a Bluetooth module. The Fresnel lens is placed between the PIR sensor and the shutter.

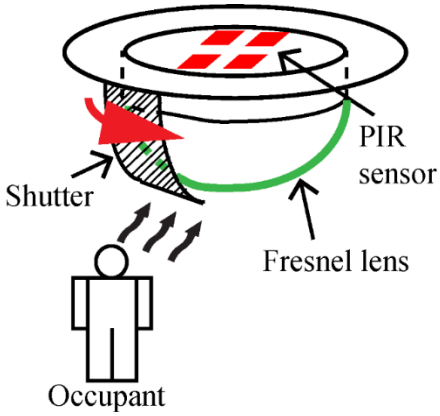

Figure 2.7 Schematic diagram of Ro-PIR sensor for occupancy detection. © 2018 IEEE. Reprinted with permission from [43].

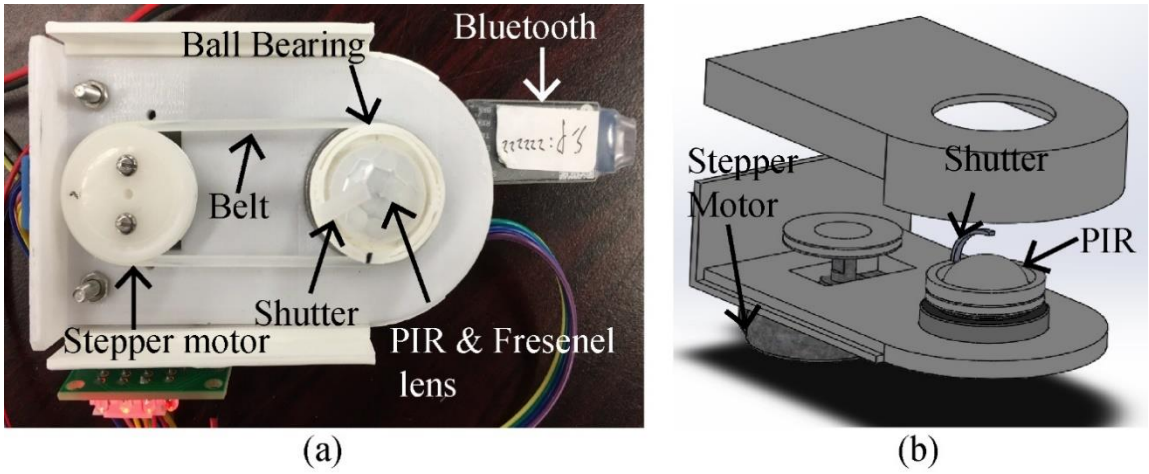

Figure 2.8 Prototype of Ro-PIR sensor. (b) 3D diagram of Ro-PIR sensor. © 2018 IEEE. Reprinted with permission from [43].

For most application scenarios, only zone-level detection is required. Thus, for this experiment, the testing area, with a height H = 2.8 m and a radial distance D = 2 m, is segmented into 2×6 = 12 zones (as shown in Figure 2.9(a)). The Ro-PIR sensor node is

placed on the ceiling, and an occupant stands at the cross points shown in Figure 2.9(b): D = 1 m, 2 m with 60° angular distance apart. Note that, the reason for not extending the test radius beyond 2 m is that the output signal will be too weak to differentiate from unoccupied scenarios.

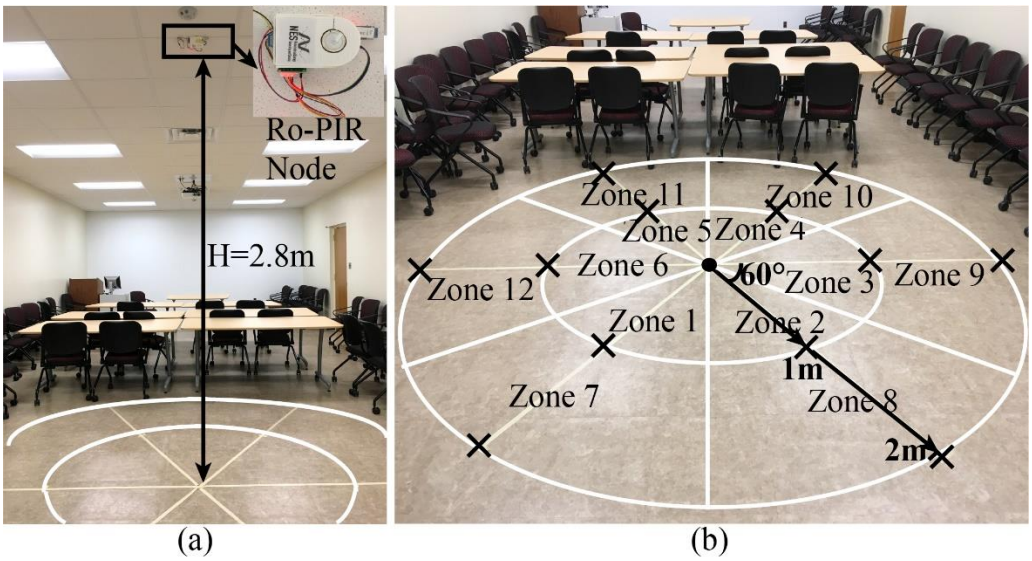

Figure 2.9 (a) Experiment setup, the sensor node was mounted on the ceiling with a height of 2.8 m with a radial floor size of 2 m. (b) Twelve zone-level segments numbered from 1 to 12 are created, which have a radial distance of 1m, 2m, and an angular distance of 60˚. Cross signs represent the standing positions of an occupant. © 2018 IEEE. Reprinted with permission from [43].

Figure 2.10 illustrates five consecutive periods when one occupant stands at D = 1 m and different angular positions, suggesting that the polarity-phase shifts with different angular positions. For each polarity peak, two features can be extracted:

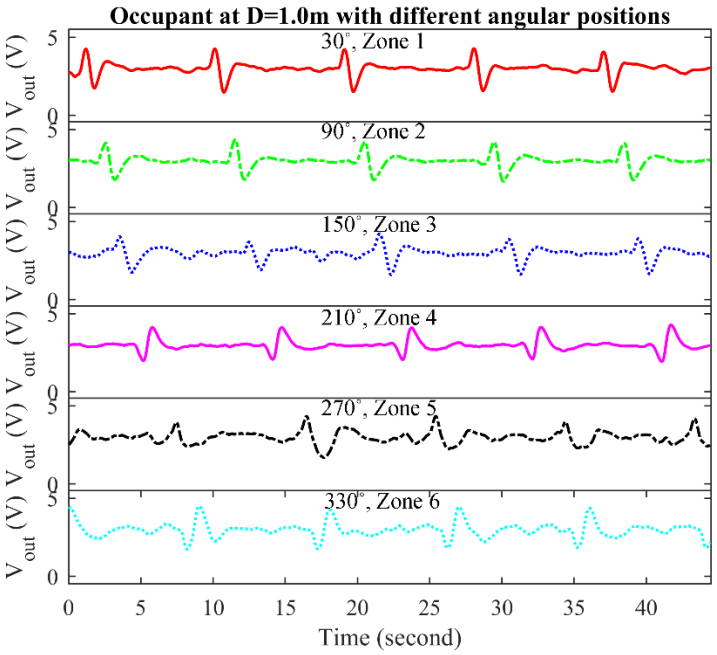

Figure 2.10 Voltage output from 5 consecutive shuttering periods when an occupant stands at radial distance D = 1 m, and different zone-level angular positions. © 2018 IEEE. Reprinted with permission from [43].

1) Peak-to-peak value V_{pp}: From Equation (2.7), V_{pp} is associated with radiant energy density W and the three covering configurations. The distance of an occupant to the Ro-PIR sensor will affect the energy density received by the sensor. Thus, V_{pp} can reflect the distance information of the occupant.
2) Intersection point position: As shown in Figure 2.10, the occupant's positions will affect the positions of the polarity phase peak pairs. We use intersection points, which are the points where the voltage signals between peak and valley meet with half of the supply voltage, to reflect the occupant's positions. From (2.7), the

intersection points are the time when the radiant energy reaches 0 W, and output voltage reaches half of the supply voltage.

These two features can be used for localization using machine learning classification algorithms. We take the following steps to extract these two features from the output voltage signals. Firstly, we find peaks and valleys with a minimum peak height (MPH) equals 3.3 V, and a maximum valley height (MVH) equals 2.0 V. Next, the intersection points, and peak-to-peak value V_{pp} are found for each peak pair.

We get two features for all peak pairs from different zone-level areas. The 720 instances in the feature space are shown in Figure 2.11. The V_{pp} values are different for the occupant at D = 1 m (Zone 1/2/3/4/5/6) because the Fresnel lens is not symmetrically segmented in a sphere, and the covered sensing beams may vary for different occupancy positions. This step is done using a Matlab program on a computer with an Intel i7-5600U CPU. The runtime of this preprocessing is 1.5 seconds.

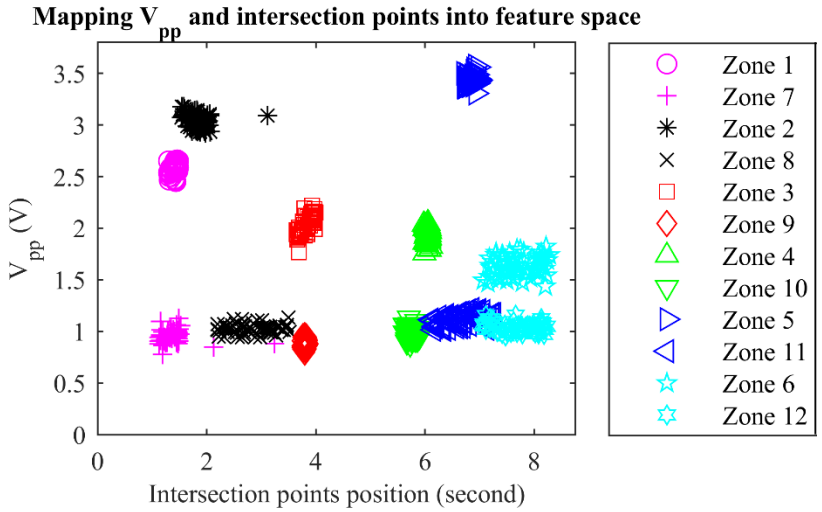

Figure 2.11 The peak-to-peak value V_{pp} and the position of intersection points are mapped into the feature space for 12 different zone-level areas. © 2018 IEEE. Reprinted with permission from [43].

Next, the training sets are fed into machine learning classifiers. We use four supervised classifiers: support vector machine (SVM), k-nearest neighbor (k-NN), Naïve Bayes, and Decision Trees. SVM is a discriminative classifier formally defined by separating hyperplanes [75, 76]. Given the training data, the algorithm gives optical hyperplanes which categorize new data. The SVM uses kernel functions to project input data into a high-dimensional space to make classification much easier. The k-NN classifier, a non-parametric classifier, categorizes new data to the most common class among its *k* nearest neighbors [77]. By using the Bayes theorem, the Naïve Bayes classifier assumes that the input features are independent. In this classifier, the posterior probability is computed from all input data based on all classes. Then the new data is assigned to the class with the highest posterior probability. Decision Trees (DTs) is a non-parametric

supervised learning method for classification and regression by making a series of decision rules from input data [78].

We adopt a free software machine learning library, scikit-learn [79], using Python programming language to test the selected classification algorithms. The following algorithms are tested: SVM, k-NN, Gaussian NB, and Decision Trees. For the SVM classifier, we choose three types of kernels: linear, polynomial, and radial basis function (RBF). For the k-NN classifier, we select k = 3, 5, and 7. To evaluate the results, we use 3-fold cross-validation. All instances are divided into three groups. Two of them are used to train the classifier and one to validate it. This step is repeated three times, and each time uses a different group of data. Table 2.2 shows the accuracy and the runtime of each classifier. From Table 2.2, linear SVM, RBF SVM, and k-NN classifiers perform better than others.

Table 2.2 Corrected classification ratio and runtime for different classifiers. © 2018 IEEE. Reprinted with permission from [43].

Classifier	Accuracy (%)	Runtime (ms)
Naïve Bayes	98.31	3
SVM, linear	98.73	3
SVM, poly	98.31	3
SVM, RBF	98.73	4
Decision Trees	97.47	1
3-NN	97.89	2
5-NN	98.73	3
7-NN	98.31	2

Table 2.3 Comparison between C-PIR, Ro-PIR and LAMPIR. © 2019 IEEE. Reprinted with permission from [44].

Sensor	Weight (g)	Size(cm)	Power(W)	Sound level (dBA)	Cost ($) vol. 10000
C-PIR	130	8×6.3×6	1.05	42.6	4.06
Ro-PIR	160	10×6×4.5	1.68	36.0	4.99
LAMPIR	40	6.5×4.3×4.5	0.19	30.2	3.46
Compare with C-PIR	-70 %	-60 %	-82 %	-12	-15 %
Compare with Ro-PIR	-75 %	-55 %	-89 %	-6	-31 %

2.2.3. The Lavet Motor Driven PIR Sensor (LAMPIR)

Compared to C-PIR and Ro-PIR, LAMPIR [44] has a smaller size and lower power consumption, as shown in Table 2.3. The reason is that instead of using a servo motor and stepper motor, LAMPIR uses a Lavet vibrator [80], which is widely used in the quartz clock and wristwatch due to its low power consumption, lower noise level, and high accuracy. Typically, an AA battery could power a quartz clock for several years. A Lavet vibrator is a special single-phase stepping motor consisting of three parts: a stator, a solenoid coil, and a permanent magnet rotor. The structural design of the low-power electromechanical driving mechanism is shown in Figure 2.12.

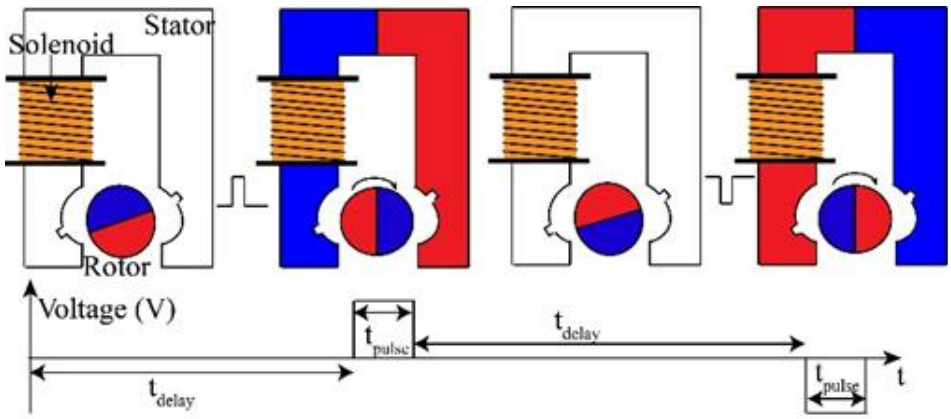

Figure 2.12 Low power electro-mechanical driving mechanism. © 2019 IEEE. Reprinted with permission from [44].

A pulse signal will be applied to the solenoid with the width of the pulse t_{pulse} and the width of zero-current t_{delay}. When the positive pulse is applied to the solenoid, the stator is energized, which forces the rotor to turn to the desired position. When there is no pulse, the stator is in a zero-current state. The rotor will reach a cogging point due to the reluctant force. Cogging point is designed by the shape of the stator, which is the position that minimizes the air volume between the rotor and stator. Next, when the negative pulse is applied, the stator is in an opposite energized state, which pushes the rotor to the opposite position as in the positive state. Thus, a cycle that consists of one positive pulse, one no-current state, one negative pulse, and another no-current state will make the rotor rotate 360° in a cycle. Note that when a pulse is applied, the rotor will rotate to the corresponding position in a very short time (approximately 25 ms). Thus, the pulse width needs to be larger than 25 ms. We choose 50 ms for reliable consideration.

The low-power electromechanical driving approach has several advantages over the traditional servo or stepper motors. Firstly, it has a much simpler structure, consisting of only one solenoid and a pulse signal source. However, a stepper motor needs two or four solenoids with a driving circuit, and a servo motor needs one direct current (DC) motor and a feedback circuit. Secondly, only one pulse signal is required to energize the stator to drive the rotor in the low-power electromechanical vibrator. However, the PWM signals are needed to hold the angular position of the servo motor, and the stepper motor needs four pulse signals to keep the rotor rotating at the designed speed. Thus, the electromechanical vibrator consumes much less power and is much lighter and smaller than the servo or the stepper motor.

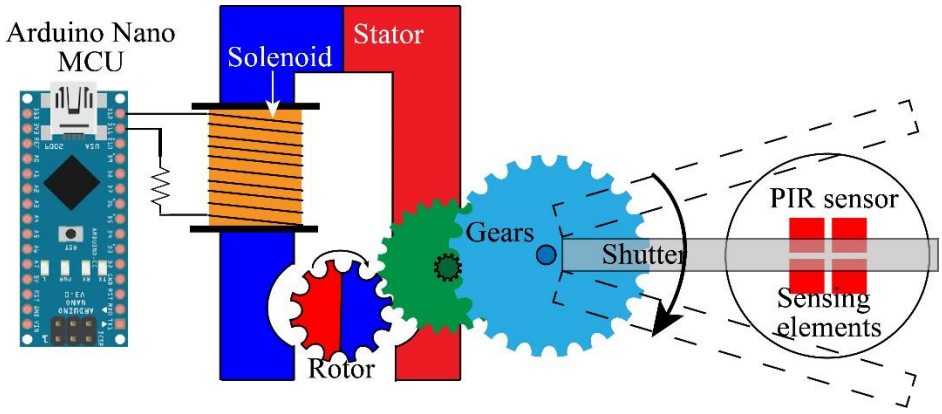

Figure 2.13 Concept design of the LAMPIR sensor. © 2019 IEEE. Reprinted with permission from [44].

Figure 2.13 illustrates the concept design of the LAMPIR sensor. An Arduino Nano MCU powers and controls both the electromechanical vibrator and the PIR sensor

(Panasonic® AMN24112). After receiving radiation energy, the PIR sensor outputs analog signals. MCU samples analog signals through ADC and sends data to a computer by a Bluetooth module. The electromechanical vibrator is placed on a circuit board and connects to the MCU. A gear chain is used to drive the HDPE shutter. The rotor in the electro-mechanical vibrator has 12 teeth. The first gear has a ratio of 6:1, and the second has 60 teeth. The HDPE shutter is attached to the second gear and can shutter across the FOV of the PIR sensor. Figure 2.14 shows the schematic and the prototype of the LAMPIR sensor, respectively.

In [44], I conduct a long-time occupancy detection test that can evaluate the long-term performance of the LAMPIR sensor. This will provide occupancy patterns in offices, homes, or buildings, making smart control strategies for lighting and HVAC systems.

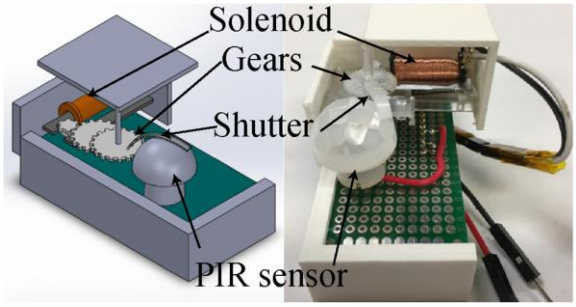

Figure 2.14 The 3D schematic and prototype of the LAMPIR sensor. © 2019 IEEE. Reprinted with permission from [44].

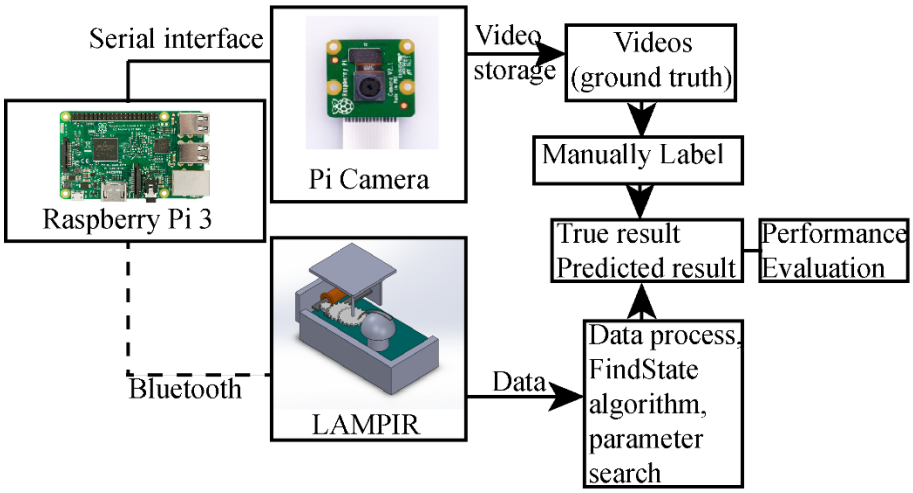

Figure 2.15 Block diagram of long-time occupancy detection platform. © 2019 IEEE. Reprinted with permission from [44].

The block diagram of a long-time occupancy detection platform is shown in Figure 2.15. The Raspberry Pi 3 is a single-board computer with a relatively higher computation power than the MCU. A Raspberry Pi camera module is connected to a Raspberry Pi computer via a camera serial interface (CSI). The camera has a FOV of 62.2° horizontally and 48.8° vertically and is integrated with a Sony® IMX219 CMOS image sensor. In this test, the camera is in video mode and records videos with a resolution of 640×480 to save storage space. Both the LAMPIR and the traditional PIR sensor are powered and sampled by the Arduino Nano MCU to illustrate the advantages of the LAMPIR sensor over traditional PIR sensors. They are placed at the same position and connected to Raspberry Pi via Bluetooth modules. The sampling rate of both the LAMPIR and PIR sensors is 120 Hz. The Raspberry Pi camera records the videos, and the output signals of the LAMPIR and the PIR sensor are recorded in a secured digital (SD) card in the Raspberry Pi 3 as

well. The videos are manually processed. When human objects are detected, the corresponding moment is labeled as an ‘occupied’ state. When no human is in the video, the corresponding moment is labeled as an ‘unoccupied’ state.

Moreover, the ‘occupied’ states can be divided into two subclasses: ‘stationary occupant’ state and ‘moving occupant’ state, which indicates stationary occupants and moving occupants, respectively. The occupancy states, which are manually labeled from videos, are used as ground truth. The output signals from the LAMPIR and the PIR sensor are processed in the following sequence: data preprocessing, FindState algorithm, parameter selection. These processes will be explained in the next section. After processing, the occupancy states are predicted from the LAMPIR and the PIR data. By comparing the predicted states and the true states, performance evaluation is made for the LAMPIR sensor.

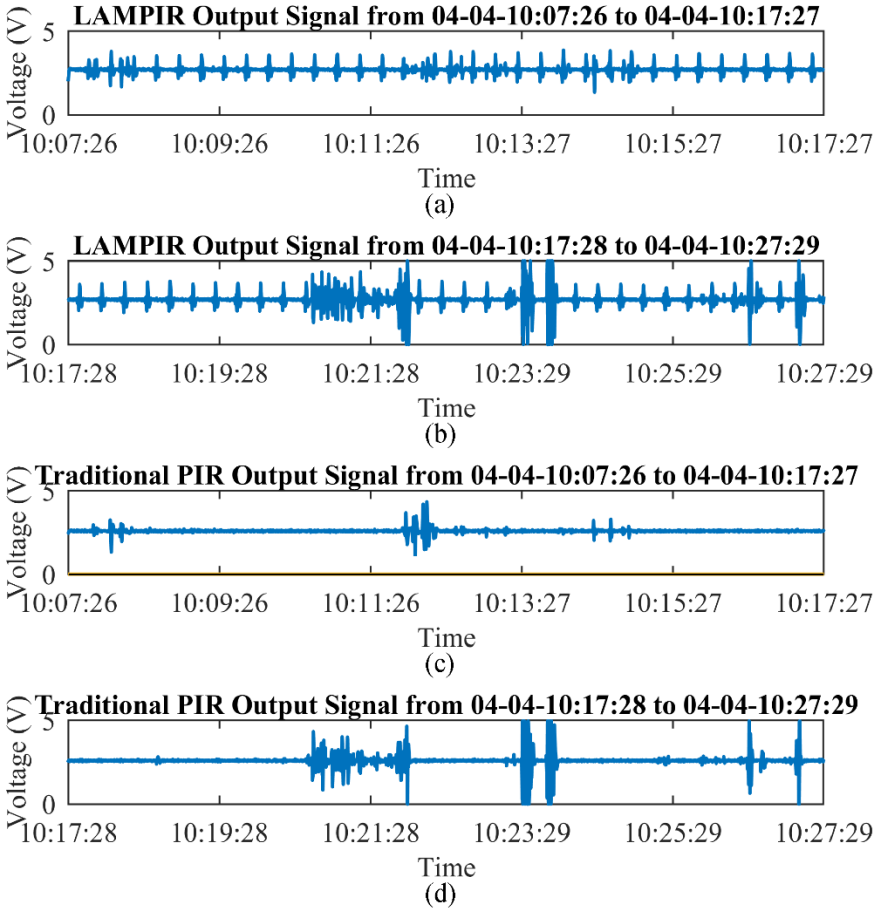

Figure 2.16 Output voltage signals of the LAMPIR sensor ((a), (b)), and traditional PIR sensor ((c), (d)) from Apr. 04, 2018 10:07:26 to 10:27:29. © 2019 IEEE. Reprinted with permission from [44].

Figure 2.16 shows the output signal of the LAMPIR and the traditional PIR sensor within 20 minutes, recorded from 04/04/2018 10:07:26 to 10:27:29. Figure 2.16 (a) and (b) show signals of the LAMPIR sensor, while Figure 2.16 (c) and (d) represent signals from the traditional PIR sensor. After analyzing the videos corresponding to this time, one occupant sits for 20 minutes. Another occupant is walking in and out of the FOV several times, around 10:21:28, 10:23:29, and 10:27:29, respectively. For the moving scenarios,

both the LAMPIR and PIR sensor output signals with high peak-to-peak values and high occurrences of such peak pairs. However, for stationary occupants, the traditional PIR sensor only outputs relatively flat signals, while the LAMPIR sensor gives obvious polarity-shaped peaks with a constant period from each other. Note that the disturbance around 10:07:26 and 10:12:26 is caused by the slight movement of the occupant's arms. Thus, we still label these moments as 'stationary' states.

In preprocessing, collected output signals from the LAMPIR and the PIR sensor are fed to a Python script to extract signals and time stamps. More importantly, the continuous signals are split into sub-signals that each sub-signal has a duration of one minute. We split the signals into a 1-minute interval to predict the coarse states in each time interval. The coarse state is 'moving' as long as there exists one moment that the human is moving in a one-minute interval. The 'unoccupied' state happens when no occupants within the entire one-minute interval. Otherwise, the coarse state is labeled as 'stationary'.

Next, I apply the FindState algorithm for each one-minute sub-signals, as shown in Figure 2.17, based on a peak detection algorithm [81], which can find peaks with a certain minimal peak height and distance. The inputs are the signal and four parameters: $V_{th\text{-}high}$, $V_{th\text{-}low}$, MinPeakHeight (*MPH*), and MinPeakDistance (*MPD*). Firstly, the peaks with *MPH* and *MPD* are found using findpeaks function from [82]. Next, for each peak in the found peaks, find the smallest value within a one-second distance. Here, one second is chosen because this is the time when the HDPE shutter goes across the FOV of the Fresnel

lens. Thus, V_{pp} is calculated for each peak. The maximum V_{pp} is chosen to determine the state by comparing it with $V_{th\text{-}high}$ and $V_{th\text{-}low}$.

Algorithm: FindState

INPUT: Signal, $V_{th\text{-}high}$, $V_{th\text{-}low}$, MPH, MPD
OUTPUT: State

```
Peaks = findpeaks(Signal, MPH, MPD)
for each peak in Peaks do
   Find the smallest value valley within 1 second distance
   V_pp = peak-valley
end for
V_pp = max(V_pp)
if V_pp < V_th-low then
   State = Unoccupied
else if V_pp > V_th-low and V_pp < V_th-high then
   State = Stationary
else
   State = Moving
end if
return State
```

Figure 2.17 FindState algorithm. © 2019 IEEE. Reprinted with permission from [44].

Four parameters in the FindState algorithm are critical for obtaining an excellent detection performance. A grid search method is applied to choose these four parameters with the highest accuracy. The grid search range is predefined as follows: $V_{th\text{-}high} = 0.244 \times i_{th-h}$ V, where $i_{th-h} = 11,12,\dots,20$; $V_{th\text{-}low} = 0.244 \times i_{th-l}$ V, where $i_{th-l} = 1,2,\dots,10$; $MPH = (V_{th} + V_{dd})/2 + 0.049 \times (i_{MPH} - 1)$ V, where V_{th} is the threshold value 0.47 V, V_{dd} is the supply voltage, which is 5 V, and $i_{MPH} = 0,1,2,\dots,11$; $MPD = 0.833 + 0.416 \times i_{MPD}$ seconds, where $i_{MPD} = 1,2,\dots,12$. When setting the searching

range for $V_{th\text{-}high}$ and $V_{th\text{-}low}$, we segment 0V to 4.882 V range into 20 intervals. I choose the higher and lower ten interval values as $V_{th\text{-}high}$ and $V_{th\text{-}low}$, respectively. The lower bound of the *MPD* searching range uses the average peak-to-peak distance when an occupant moves in the FOV.

Next, 50% of the dataset is chosen as the training set. Each combination of these four parameters is used to evaluate the accuracy. Figure 2.18 shows partial of the grid search result of these four parameters. Figure 2.18 (a) and (b) illustrate the 3-state accuracy while Figure 2.18 (c) and (d) indicate the 2-state accuracy. Figure 2.18 (a) and (c) are plotted when fixing *MPH* = 2.734 V and *MPD* = 1.25 seconds. Figure 2.18 (b) and (d) are plotted when fixing $V_{th\text{-}high}$ = 3.906 V and $V_{th\text{-}low}$ = 0.976 V. Within the whole grid search space, when $V_{th\text{-}high}$ = 3.906 V, $V_{th\text{-}low}$ = 0.976 V, *MPH* = 2.734 V, and *MPD* = 1.25 seconds, 3-state accuracy reaches 94.1%. When $V_{th\text{-}low}$ = 0.976 V, and *MPD* = 1.25 seconds, 2-state accuracy reaches 96.88%.

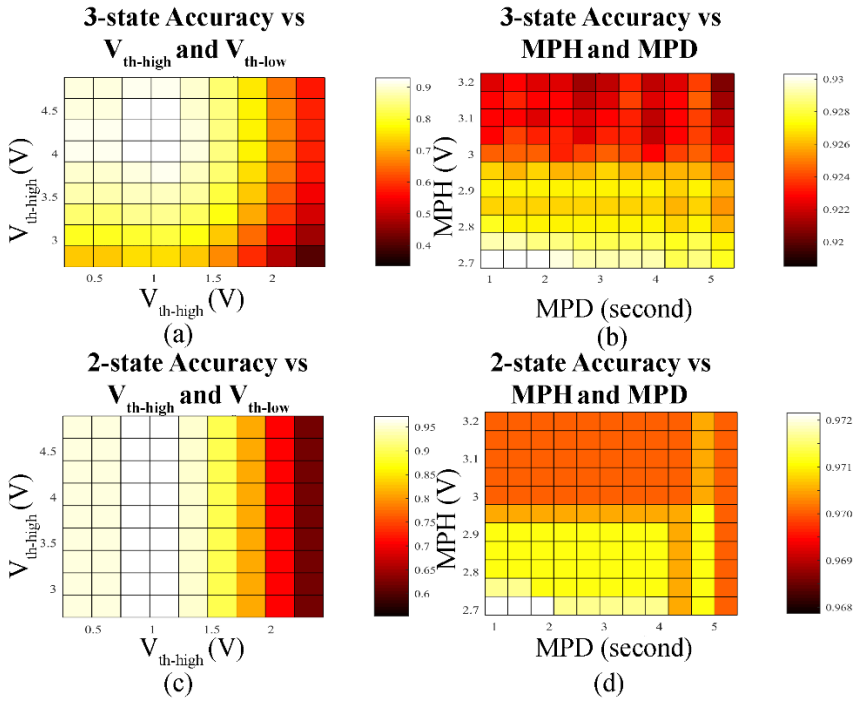

Figure 2.18 Grid search to find optimal parameters in the FindState algorithm. (a) and (c) are 3-state and 2-state accuracy versus Vth-high and Vth-low, respectively, when *MPH* = 2.734 V, and *MPD* = 1.25 seconds. (b) and (d) are 3-state and 2-state accuracy versus MPH and MPD, respectively when $V_{th\text{-}high}$ = 3.906 V, and $V_{th\text{-}low}$ = 0.976 V. © 2019 IEEE. Reprinted with permission from [44].

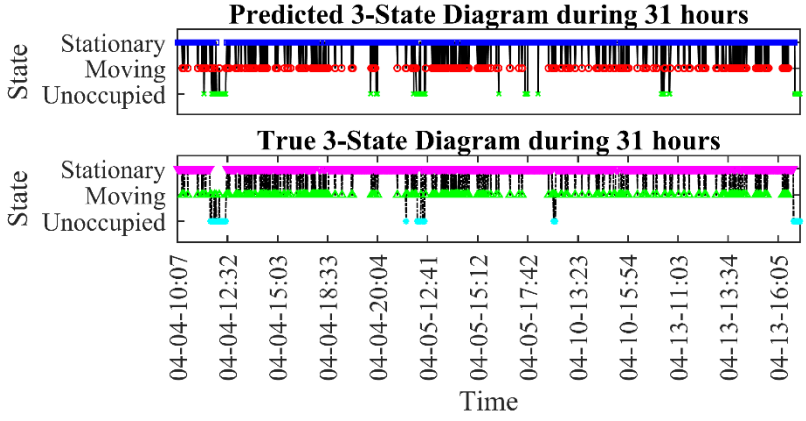

Figure 2.19 Predicted and true 3-state diagram during 31 hours. © 2019 IEEE. Reprinted with permission from [44].

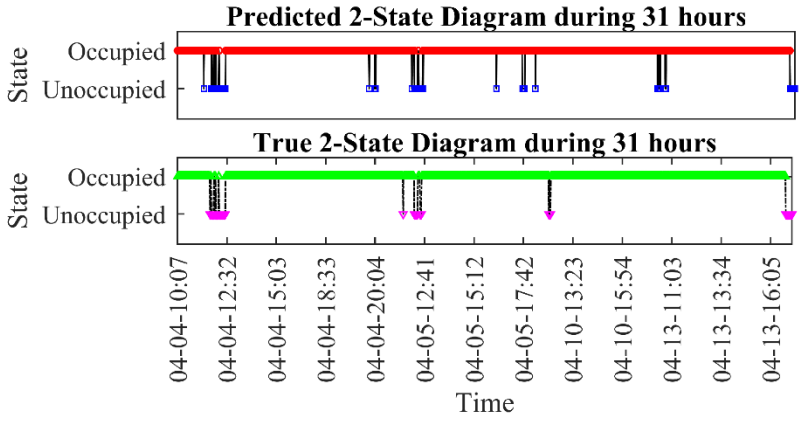

Figure 2.20 Predicted and true 2-state diagram during 31 hours. © 2019 IEEE. Reprinted with permission from [44].

Figure 2.19 and Figure 2.20 illustrate the state diagram within an approximately 31-hour detection period within four workdays, that is from 04/04/2018 10:07 to 04/04/2018 20:07, from 04/05/2018 10:16 to 04/05/2018 17:47, from 04/10/2018 10:58 to 04/10/2018 17:58, and from 04/13/2018 10:58 to 04/13/2018 17:58. We extract one occupancy state for every minute. The total number of states is 1865. The following parameters are chosen: $V_{th\text{-}high}$ = 3.906 V, $V_{th\text{-}low}$ = 0.976 V, *MPH* = 2.734 V, and *MPD* = 1.25 seconds. The 3-state accuracy for the whole dataset is 92.9%, while a 2-state accuracy for the whole dataset is 97.2%.

2.2.4. LWIR LC Shutters

This subsection will review different LWIR LC shutters using materials summarized in Table 1.1. Since invented in 1973 [83], TNLC has been commonly used in LC display industry. Its application in the infrared region (2-14 μm) was first studied by

Wu's group [60, 84]. They developed the LWIR TNLC shutter with two infrared polarizers, two infrared-transparent substrates coated with polyimide (PI). Each PI-coated substrate was rubbed by a cloth in one direction so that their rubbing directions are perpendicular to each other. The directions of the LC molecules will align to the rubbing directions.

When there is no electric field, the direction of the LC molecules at the top is parallel with the top polarizer's direction, which makes the incident light transmit through. After traversing through the LC material, the polarizing direction of the light will rotate for 90°. Similarly, since the rubbing direction of the bottom substrate is parallel with the bottom polarizer, the light could be transmitted through the bottom polarizer. With the presence of the electric field, the LC molecules will align with the direction of the external field, which is perpendicular to the path of the light. When propagating through the LC material, the polarizing direction of the light does not change and will be blocked by the bottom polarizer. TNLC is widely used in display fields within the visible light region [85-87]. The advantage of TNLC is that the contrast ratio is high. However, there are several limitations for the TNLC shutters in the LWIR region: (1) the application in the LWIR region requires a larger cell gap (~46μm), which causes a large response time (4 seconds); (2) two infrared polarizers are required, which increases the cost dramatically; (3) The polarizers will reduce the transmission rate.

FLC material has the property of polarization inversion, which causes the transient light scattering mode (TSM) effect [88, 89]. In the TSM effect, the dipole moment in the LC material is aligned with the direction of the applied electric field. When the polarity of

the electric field is reversed, the dipole moment is oriented to a new direction. The light scattering takes place due to the transient disturbance of the LC material orientation. According to [64, 65], the ferroelectric LC infrared shutter has low transmission difference (6% to 8%) and requires a high driving voltage amplitude (25V or above).

CLC is a reflective display that does not require a backlight system but uses ambient light as the light source [90-92]. CLC does not require polarizers because it does not use the retardation effect. CLC utilizes the Bragg effect that reflects the light with a specific wavelength according to the chiral pitch of the LC in the cell. However, this is also the limitation for infrared applications because they require a wide wavelength range (8-12μm). Also, the fabrication process is complicate. CLC requires ultra-violet (UV) light to stabilize the polymer while the Ge substrates are opaque to UV light.

For AALC shown in Figure 2.21, the LC molecule has two light axes, the long axis and the short one. When no electric field is applied, the plane formed by the long and short axes is perpendicular to the incident light. Then the light in both directions has large absorption. As the electric field increases, the LC molecules will be reoriented along the electric field direction. In this case, the long axis and the incident light share the same polarization, which decreases the absorption. Thus, the external electric field will increase the transmission. The LC material that shows a potential application in the infrared region has been developed [57]. However, compared to other LC types, the modulation is lower, which limits the application.

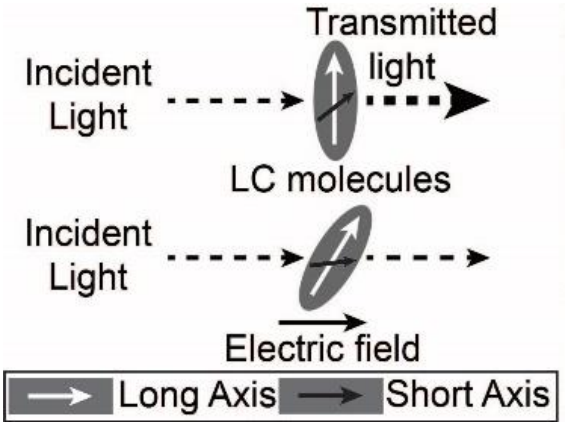

Figure 2.21 Working principle of the anisotropic absorption LC shutter. © 2020 IEEE. Reprinted with permission from [42].

PDLC is also widely used in the LC display industry [58, 59, 93, 94]. As shown in Figure 2.22, a PDLC cell consists of a liquid crystalline material dispersed as droplets in a polymer film and operates on the principle of electrically controlled birefringence [59, 95]. Figure 2.22 illustrates the basic operation principle of the PDLC shutter. When no voltage is applied (E=0), which is called the OFF state, the orientations of the droplets are random. The average refractive index of droplets and polymer film shows a mismatch. Thus, in this state, the incident radiation is scattered. When an electric field is present across the film, which is in the ON state, the droplet director will align with the electric field. When the refractive index of polymer (n_p) is close to the ordinary index of the LC droplet (n_o), the PDLC shutter shows high transmission to the incident light, as shown in Figure 2.22 (b). According to [67, 68], PDLC infrared shutters have higher transmission differences compared to ferroelectric LC, CLC, and AALC shutters. Also, since the PDLC shutter utilizes the scattering effect in the OFF state, no infrared polarizers are required,

which reduces the cost significantly. Thus, the following chapters in the dissertation will mainly focus on the study of PDLC infrared shutters, including building a model based on the modulation and response time, optimizing the performance, and studying their application.

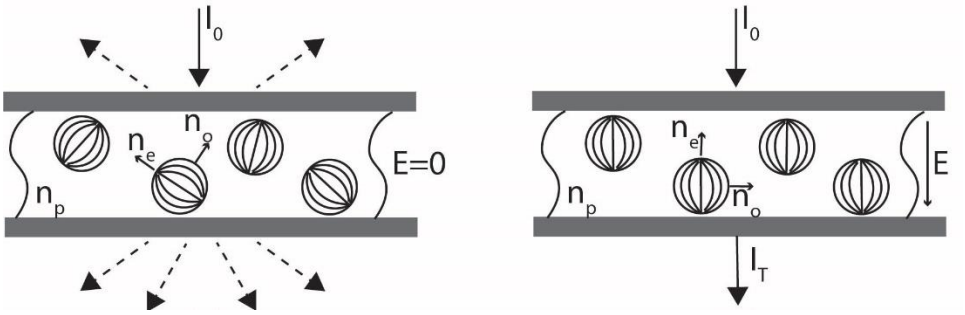

Figure 2.22 Working principle of the PDLC shutter. (a) Scattering mode, and (b) transparent mode. Here, n_p, n_e and n_o represent the refractive index of polymer film, extraordinary index, and ordinary index of LC droplets, respectively. Reprinted with permission from [96].

The material selection for the PDLC infrared shutter is as followed. The substrates are the single side anti-reflection (8-12 μm) coated germaniums. The anti-reflection coating could reduce the reflection of the incident light at the interface between the air and the germanium [69, 97, 98]. I choose E7 as the liquid crystal material for the infrared PDLC shutter due to its high transmission and relative large birefringence in the LWIR region, where $\Delta n = 0.22$ [60, 63]. Meanwhile, I select polyvinylpyrrolidone (PVP) as the polymer since the refractive index $n_p = 1.527$ is close to the ordinary index of the LC n_o =1.5 [99]. This closeness could make the transmission rate be high when the electric

field is present. The difference between n_p and n_e could increase the scattering effect [100, 101].

Compared to the TNLC and the AALC shutter [42], the PDLC shutter's fabrication process is simpler, as shown in Figure 2.23. The PDLC shutter is prepared by solvent-induced phase separation (SIPS) followed by thermally induced phase separation (TIPS) [102]. During SIPS, the nematic LC material E7 (BOC Sciences, Inc.) and the polymer PVP (VWR International) are dissolved in chloroform (VWR International). The mixture is then distributed on one Ge substrate (Shenyang Ebetter Optics Co., Ltd.) and let the chloroform evaporate. After applying the glass beads with the size of the desired cell gap, another Ge substrate is pressed on the top at a high temperature (100°C). The droplet size is controlled by cooling the E7/PVP PDLC shutter at a desired cooling rate. Normally, the cooling rate varies within 0.1 to 4 °C/min [102, 103]. The faster cooling rate will decrease the droplet size for the same mass fraction between the liquid crystal and polymer. The droplet size is observed by a polarized optical microscope on the PDLC shutter prepared under identical fabrication conditions with glass substrates instead of Ge substrates.

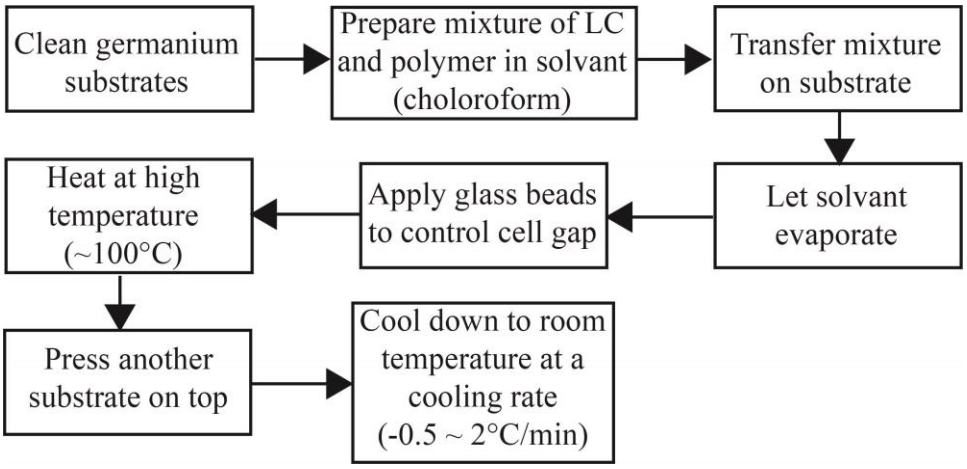

Figure 2.23 Fabrication process of the PDLC infrared shutter.

In the following work, we will characterize the PDLC infrared shutters in terms of their effective modulation and response time. Compared to previously made AALC infrared shutters [42], the optimized PDLC shutters improve the effective modulation by 136%. Compared to the PDLC shutters made by other researchers [67, 68], the optimized PDLC shutters improve the contrast ratio by 16% and transmission difference by 165% as shown in Figure 2.24. Take the wavelength $\lambda = 10\mu m$ as an example, the contrast ratio and the transmission difference are defined by $\xi_{on}(10\mu m)/\xi_{off}(10\mu m)$, and $\xi_{on}(10\mu m) - \xi_{off}(10\mu m)$, respectively. Here, $\xi_{on}(\lambda)$ and $\xi_{off}(\lambda)$ are the wavelength-dependent transmission spectrums in LWIR region (8-12 μm) for ON and OFF state, respectively. The bars in the figure shows the average contrast ratio and the transmission difference of 4 samples from references [67, 68], and 23 samples with the optimal preparation condition, where the mass ratio η of the LC is 80%, the cell gap d is $22\mu m$ and the cooling rate is 1°C/min. The error bars represent the standard deviation. The reason

that our PDLC infrared shutters have better performance is that I systematically optimize the fabrication conditions that yield the best modulations, which will be detailed in Chapter 4.

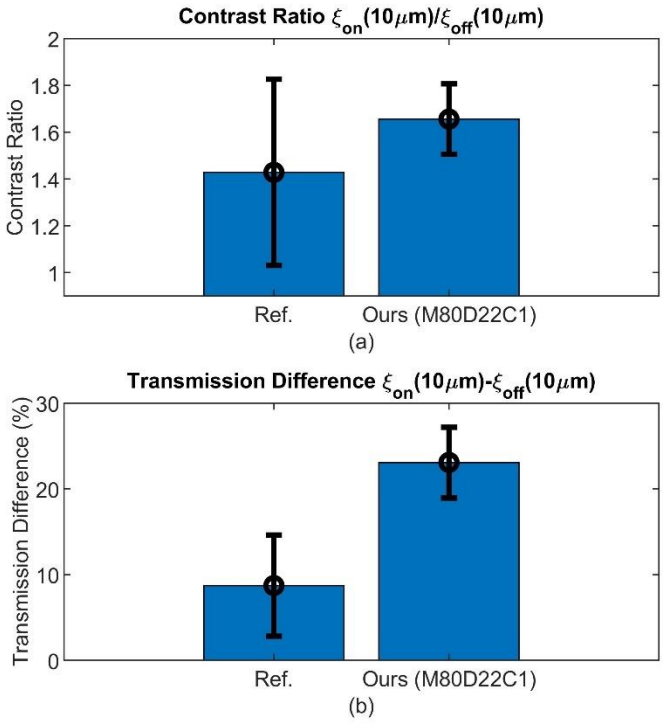

Figure 2.24 The comparison of (a) contrast ratio and (b) transmission difference between the reference [67, 68] and our work.

The PDLC infrared shutters under the optimized fabrication conditions show higher contrast ratios and transmission differences than the reference [67, 68]. In the remaining dissertation, we use another term, effective modulation, to characterize the PDLC infrared shutters. Effective modulation reflects the difference of the transmitted

LWIR radiation between the ON and OFF states. Compared to the contrast ratio and transmission difference at the wavelength of $10\mu m$, the effective modulation over the LWIR region (8-12 μm) better describes the property of the PDLC shutters.

2.3. Summary

In this Chapter, the working principle of the PIR sensor and the mechanically chopped PIR sensors are presented. The C-PIR sensor uses a servo motor to drive a semi-transparent shutter that goes across the PIR sensor's FOV. The Ro-PIR sensor uses a stepper motor to rotate the shutter around the center of the PIR sensor. The LAMPIR uses a Lavet motor to drive the shutter to reduce the power consumption, noise, and size. However, mechanical shutters have several disadvantages: (i) high power consumption, (ii) large noise that will disturb users, and (iii) low reliability that requires frequent maintenance.

Different LWIR LC infrared shutters are reviewed, including TNLC, Ferroelectric LC, CLC, AALC, and PDLC. Among those, PDLC infrared shutters have the advantage of low cost, high modulation, and a simple preparation process.

In this dissertation, the characterization and optimization of the PDLC shutter will be studied. Specifically, the impact of the fabrication and driving conditions on the effective modulation and the response time is studied.

3. DESIGN AND CHARACTERISTICS OF THE SLEEPIR SENSOR MODULE

In this chapter, the SLEEPIR sensor module, which consists of a PDLC infrared shutter and a traditional PIR sensor, is designed and characterized. A theoretical model of the output of the SLEEPIR sensor module is developed as a function of the effective modulation and the response time of the PDLC shutter, and the time constants of the PIR sensor. The time constants of the PIR sensor are measured using a rotating optical chopper.

3.1. Design of the SLEEPIR Module

As aforementioned in Section 2.2.4, the transmission of the PDLC shutter in the LWIR region rises with an electric field applied and will drop after removing the electric field. Typically, the driving voltage that controls the transmission of the PDLC infrared shutter is an alternative current (AC) voltage without DC components to avoid the ionic material being attracted to the substrates and degrade the performance [104]. As shown in Figure 3.1, the blue curve represents the applied voltage on the PDLC shutter.

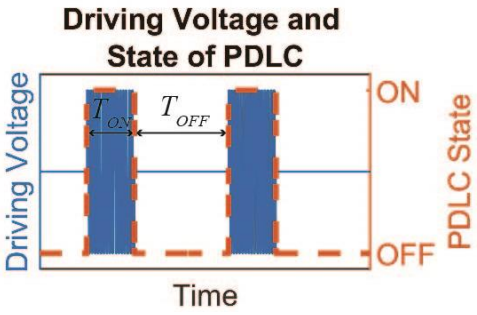

Figure 3.1 The ON-OFF states of the SLEEPIR sensor module vs. the applied driving voltage.

The time period that the AC voltage is turned on and off is T_{ON} and T_{OFF}, respectively. During the T_{ON} state, the AC voltage with the frequency f_{AC} and amplitude V_{rms} is applied. During the T_{OFF} state, the voltage is zero across the PDLC shutter. The orange curve in Figure 3.1 represents the state of the PDLC shutter. We denote the state "ON" to be the state with the presence of the AC voltage, "OFF" to be the state when removing the AC voltage.

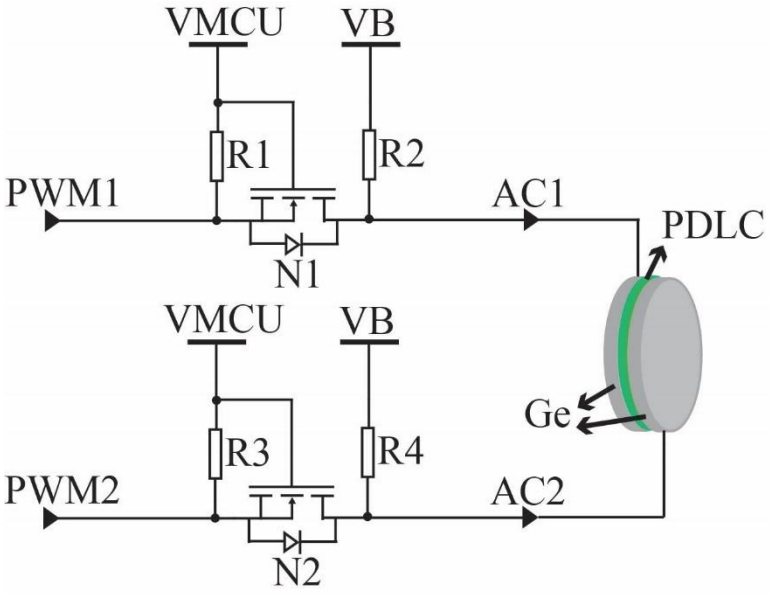

Figure 3.2 The driving circuit of the PDLC shutter.

As aforementioned in Figure 1.3, the SLEEPIR sensor module consists of a PDLC shutter, a PIR sensor, and a driving circuit. The driving circuit is shown in Figure 3.2. PWM1 and PWM2 represent the two channels of the PWM signals sent from the MCU.

VMCU represents the supply voltage of the MCU. Normally, VMCU=3.3V. VB is the output of a DC-DC upconverter. In this study, VB is selected to be 10V, which is enough to maximize the transmission difference. Resistors R1 to R4 are used to limit the current.

PWM1 and PWM2 are PWM signals that have a 50% duty cycle and a frequency of f_{AC}.These two PWM signals are also out of phase, as illustrated in Figure 3.3. Their amplitude is VMCU, which is 3.3V. Each channel of the PWM signal is connected to the source pin of an N-type metal-oxide-semiconductor field-effect transistor (NMOS), N1 and N2, respectively. The gate pin of the NMOS is connected to the VMCU. The output AC voltages, AC1 and AC2, are connected to the drain pin of the NMOS.

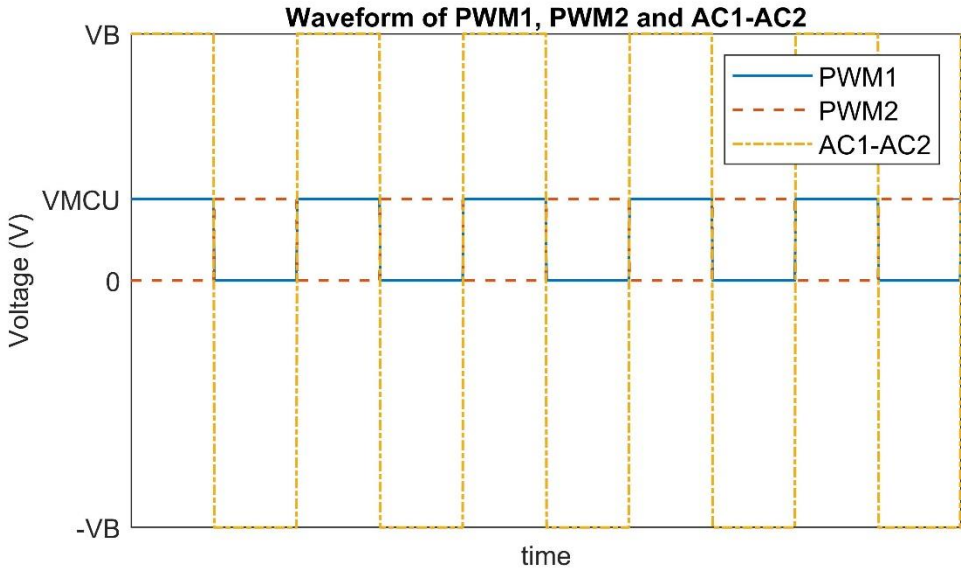

Figure 3.3 Waveform of PWM1, PWM2, and AC1-AC2 in the driving circuit.

Consider the first channel that converts PWM1 to AC1. When PWM1 is high ($PWM1(t) = VMCU$), the voltage difference between the gate and source of NMOS is zero. NMOS is in the cut-off region, where no current flows through it. Then AC1 will be pulled up to VB. When PWM1 is low ($PWM1(t) = 0$), the voltage difference between the gate and the source of NMOS is VMCU, which makes the NMOS function as a closed switch. Thus, AC1 is pulled down to 0.

$$AC1(t) = \begin{cases} VB, & PWM1(t) = VMCU \\ 0, & PWM1(t) = 0 \end{cases} \tag{3.1}$$

Thus, the signal of AC1 and AC2 are also PWM signals with the amplitude of VB and the frequency of f_{AC}. Moreover, their phases are opposite to each other. When connecting AC1 and AC2 to two Ge substrates of the PDLC shutter, the effective voltage applied on the PDLC shutter is AC1-AC2, which is an AC voltage, shown in Figure 3.3.

As aforementioned in Chapter 1, commercial PIR sensors have an even number of sensing elements, typically two or four. Each sensing element has a polarization, which is the opposite direction to its neighboring one [105, 106]. Figure 3.4 shows two types of connections of two types of PIR sensors. The direction of arrows represents the polarization of the sensing elements. Figure 3.4(c) illustrates the PIR sensor with four sensing elements connected in series, which is the case (AMN24112, Panasonic) we are using in this dissertation. Since the environmental changes that affect all sensing elements are identical, the pyroelectric currents from the sensing elements cancel each other. For a SLEEPIR sensor module, although changing the state of the PDLC shutter could change the received radiation of the sensing elements, the compensation effect will lead to a flat output signal. Thus, in this dissertation, we use copper foils, which is opaque in the LWIR

region, to cover two sensing elements in diagonal to cancel the compensation effect. Only the uncovered sensing elements could respond to the infrared radiation variation. The uncovered and covered PIR sensors are shown in Figure 3.5. There is an optical window on the shell of the PIR sensor to make sure the sensing elements encapsulated in the sensor receive the radiation in LWIR region (8-12μm). The copper foils cover two diagonal areas on the optical window to block the radiation received by the two diagonal sensing elements.

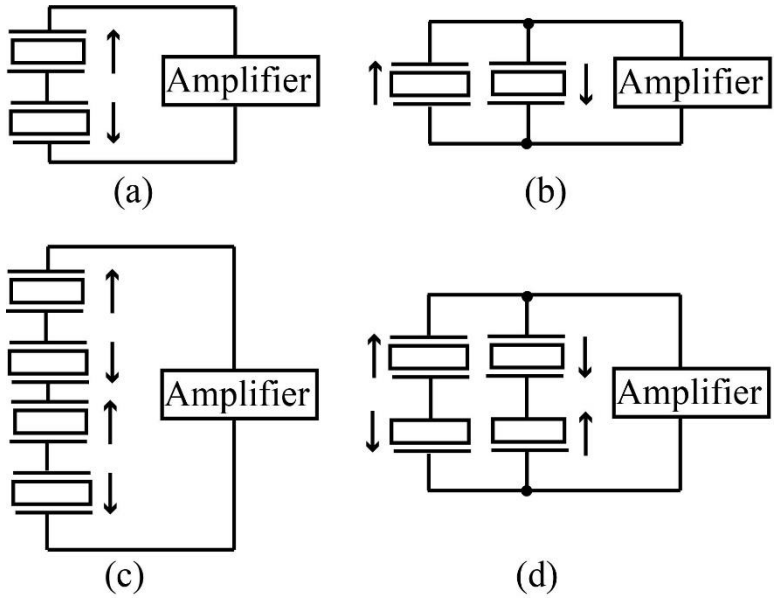

Figure 3.4 (a) Two sensing elements in series. (b) Two sensing elements in parallel. (c) Four sensing elements in series. (d) Four sensing elements in parallel. The arrow next to each sensing element represents the polarization.

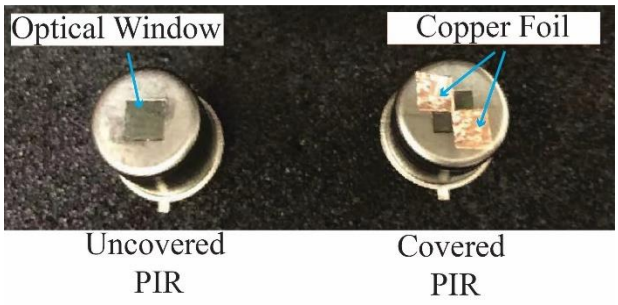

Figure 3.5 The uncovered PIR sensor (left) and the covered PIR sensor (right).

3.2. Model of the SLEEPIR Module

In this subsection, we construct the SLEEPIR sensor module's output model as a function of the incident infrared radiation, the effective modulation and the response time of the PDLC infrared shutter, and the time constants of the PIR sensor. In Chapter 2.1, the output signal of a traditional analog PIR sensor is modeled. Equation (2.7) shows the output of the preamplifier stage of a pyroelectric element when the incident radiation is $W(t) = W_0 \exp(i\omega t)$.

When building the model, we consider a traditional analog PIR sensor with a single pyroelectric element and a second-stage amplifier. If we denote, the gain of the second-stage amplifier is A_{amp}, the output of this analog PIR sensor becomes

$$V_{out}(t) = \frac{K_{PIR}\omega}{(1+\omega^2\tau_T^2)^{1/2}(1+\omega^2\tau_{\mathrm{E}}^2)^{1/2}} W(t) \tag{3.2}$$

where $K_{PIR} = A_{amp}R_{fb}\alpha p' A/G_T$.

Next, we look at the incident radiation power $W(t)$. This represents the infrared radiation transmitted through the PDLC shutter and received by the PIR sensor. Figure 3.6

illustrates the variation of the transmitted infrared radiation when the PDLC shutter changes its operation state between ON and OFF. Before the time instant t_1, the PDLC is in the OFF state, the transmitted infrared radiation after PDLC shutter is denoted as W_{OFF}. After the AC voltage is applied at t_1, the transmission rate of the PDLC shutter starts increasing over time. The transmitted radiation reaches the maxima value, W_{ON} at time t_2. Similarly, from t_3 to t_4, after removing the AC voltage, the transmitted infrared radiation of the PDLC shutter decreases from W_{ON} to W_{OFF}.

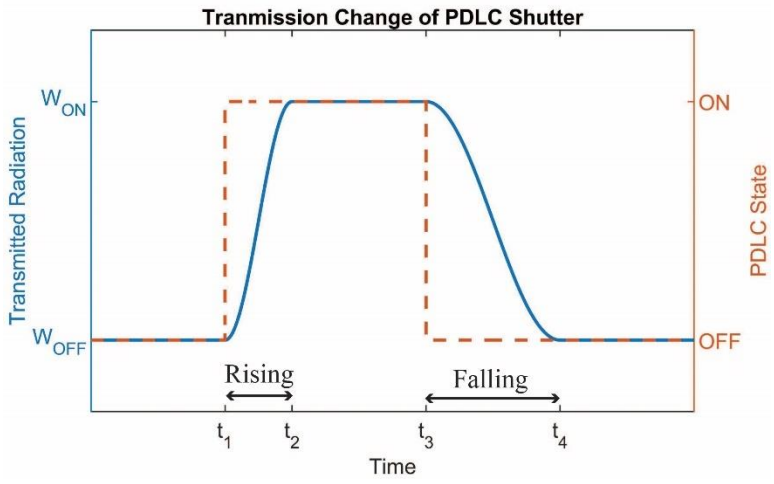

Figure 3.6 Illustration of the variation of the transmitted infrared radiation when PDLC changes its operation state between ON and OFF.

We use "response time" to represent how fast the PDLC shutter changes its transmission. The measurement of the response time will be described in Section 3.4. Here, we define two phases. The "rising phase" corresponds to the time period from t_1 to t_2,

and the "falling phase" corresponds to the time period from t_3 to t_4, as shown in Figure 3.5. To simplify the modeling, we assume that the transmitted radiation within the rising and the falling phase changes in a sinusoidal manner, which can be represented in the following respective forms:

$$W_{rise}(t) = \frac{W_{ON} - W_{OFF}}{2}\exp(i\omega_r t) + \frac{W_{ON} + W_{OFF}}{2} \tag{3.3}$$

$$W_{fall}(t) = \frac{W_{OFF} - W_{ON}}{2}\exp(i\omega_d t) + \frac{W_{ON} + W_{OFF}}{2} \tag{3.4}$$

where $\omega_r = \pi/(t_2 - t_1)$, $\omega_d = \pi/(t_4 - t_3)$. Equation (3.3) and (3.4) indicate that during the rising and the falling phase, the infrared radiation transmitted through the PDLC shutter or received by the PIR sensor, is modulated at the frequency of ω_r and ω_d, respectively. From Chapter 2.1.2, we know that only when the incident radiation is sinusoidally modulated, the output of the PIR sensor could be written in Equation (2.7) or Equation (3.2). If we substitute the term $W(t)$ in Equation (3.2) by Equation (3.3) and (3.4), then the output of the SLEEPIR sensor module during the rising phase and the falling phase yields:

$$V_{out,rise}(t) = \frac{K_{PIR}\omega_r(W_{ON} - W_{OFF})}{2(1 + {\omega_r}^2\tau_T^2)^{\frac{1}{2}}(1 + {\omega_r}^2\tau_E^2)^{\frac{1}{2}}}\exp(i\omega_r t) \tag{3.5}$$

$$V_{out,fall}(t) = \frac{-K_{PIR}\omega_d(W_{ON} - W_{OFF})}{2(1 + {\omega_d}^2\tau_T^2)^{\frac{1}{2}}(1 + {\omega_d}^2\tau_E^2)^{\frac{1}{2}}}\exp(i\omega_d t) \tag{3.6}$$

We could consider K_{PIR} as a constant, which depends only on the internal thermal and electrical parameters of the PIR sensor. Then Equations (3.5) and (3.6) prove that the output of the SLEEPIR sensor module depends only on three factors: the modulation

frequency of the rising and the falling phase ω_r and ω_d, the difference of the transmitted radiation $W_{ON} - W_{OFF}$ of the PDLC shutter, and the time constants of the PIR sensor: the thermal time constant τ_T of the pyroelectric material and the electrical time constant τ_E of the preamplifier circuit.

The difference of the transmitted radiation $W_{ON} - W_{OFF}$ and the modulation frequency, ω_r and ω_d, represent how much and how fast the infrared radiation is transmitted by the PDLC shutter between the ON and the OFF state, respectively. The latter can be calculated by measuring the response time of the PDLC infrared shutter, which will be detailed in Chapter 3.4.

The time constants, τ_T and τ_E, represent how fast the PIR sensor responds to the changes of the infrared radiation. Their values influence the sensitivity of the SLEEPIR sensor module. Their measurement and characteristic analysis are detailed in Chapter 3.3.

The difference of the transmitted radiation and the response time of PDLC shutters and their optimization are introduced in Chapter 3.4.

3.3. Time Constants of the PIR Sensor

As shown in Equation (3.2), the output of an analog PIR sensor $V_{out}(t)$ is a function of the sinusoidal modulation frequency ω of the incident infrared radiation. According to [7], the frequency response of the PIR sensor's output is reasonably flat between τ_T^{-1} and τ_E^{-1}, deviating by -3dB from the maximum value. The time constants τ_T and τ_E could be derived once the frequency response is found.

The experimental setup to measure the time constants of τ_T and τ_E of the PIR sensor is shown in Figure 3.7. A blackbody radiation source (ThermoWorks IR-500) is

used to emit infrared radiation. An optical chopper is placed between the blackbody source and the PIR sensor (AMN24112 Panasonic). The optical chopper is a 3D printed circular plate with different numbers (1 and 5) of chopper blades. The rotation frequency of the chopper ω_c is controlled by a stepper motor. A black cardboard (opaque in the LWIR region) with a circular hole is placed between the chopper and the PIR sensor to limit the FOV of the PIR sensing elements. An oscilloscope reads the output voltage of the PIR sensor.

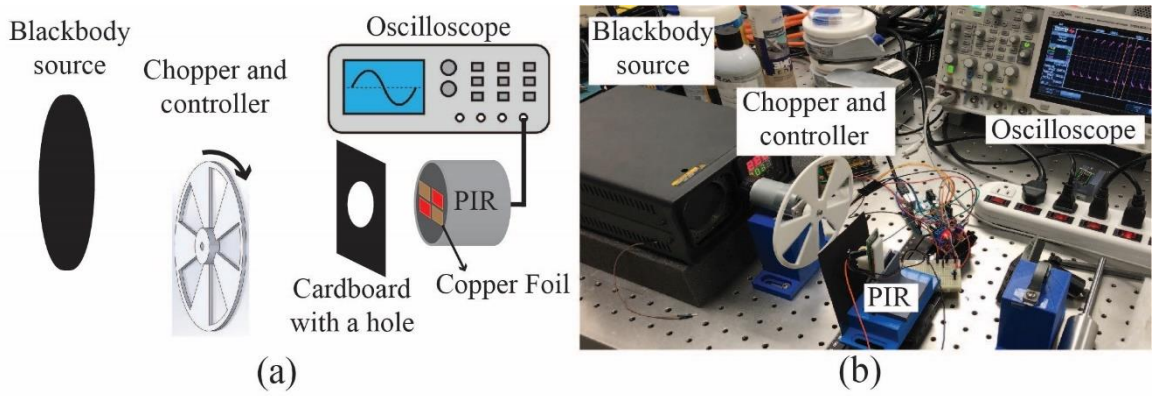

Figure 3.7 (a) The schematic and (b) the photographic representation of the experimental setup to measure the time constants of the PIR sensor.

The infrared radiation from the blackbody is chopped by the rotating optical chopper. The chopped radiation is in the shape of a sector, which has a radius of *R* and rotating at a frequency of ω_c. The cardboard with a hole crops the sensing area of the PIR sensor into a cylinder area. In Figure 3.8, a 3D illustration of the chopped radiation and the effective sensing beam is shown. The orange sector shape represents the chopped

infrared radiation. The blue cylinder area represents the effective sensing beam with a radius of r.

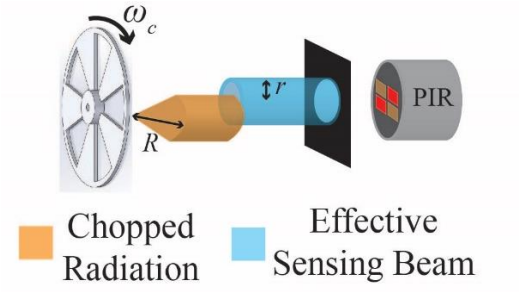

Figure 3.8 The 3D illustration shows the chopped radiation rotating across the effective sensing beam.

As shown in Figure 3.9, if we denote the overlapped area between the chopped radiation and the effective sensing beam to be $S(t)$, and we assume that the intensity of the chopped radiation is uniformly distributed, then the received radiation power of the PIR sensor $W(t)$ is proportional to $S(t)$.

$$W(t) = I_s S(t) \tag{3.7}$$

where I_s represents the intensity of the radiation. When the chopped radiation rotates, the overlapped area $S(t)$ and the received radiation power of the PIR sensor $W(t)$ will change over time.

The next step is to calculate the overlapped area $S(t)$ over time t. I define four time instances t_a, t_b, t_c, t_d to represent the time stamp when the chopped radiation interacts with an effective sensing beam. As shown in Figure 3.10, the chopped radiation

area rotates with a frequency of ω_c. Its bottom edge is firstly tangent with the effective sensing beam at the time instant t_a. At time t_b, the effective sensing beam is fully covered. Here, t_c represents the time when the upper edge of the chopped radiation is tangent with the effective sensing beam. And the effective sensing beam and the chopped radiation are separated at time t_d.

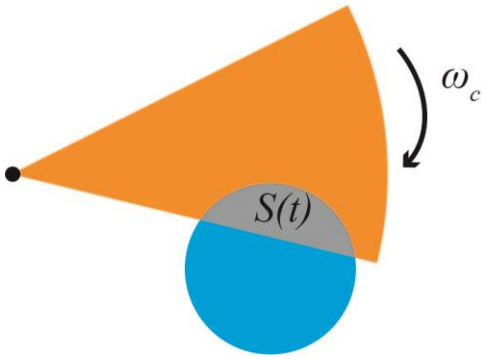

Figure 3.9 The common area between the rotationally chopped radiation and the effective sensing beam.

The overlapped area $S(t)$ could be calculated. Specifically, I denote two phases, the "incoming phase" and the "leaving phase", to represent the time within $[t_a, t_b]$ and $[t_c, t_d]$, respectively.

$$S(t) = \begin{cases} S_{income}(t), t \in [t_a, t_b] \\ S_{leave}(t), t \in [t_c, t_d] \end{cases} \tag{3.8}$$

$S_{income}(t)$ and $S_{leave}(t)$ represent the overlapped area within the incoming phase and the leaving phase, which are in the following forms, respectively:

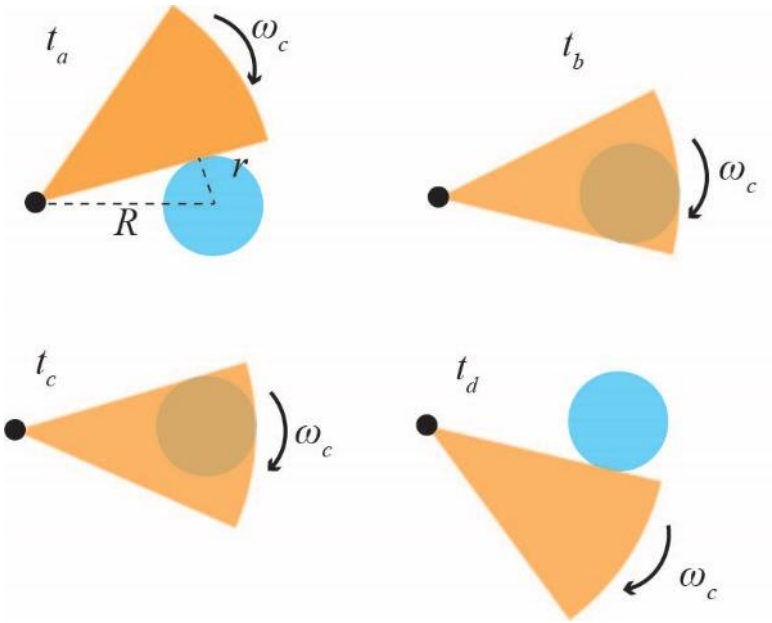

Figure 3.10 Four time instances t_a, t_b, t_c, t_d that represent the time stamp when the chopped radiation interacts with effective sensing beam.

$$S_{income}(t) = \begin{cases} r^2\beta_1 - rd_1 \sin\beta_1 , t \in [t_a, \dfrac{t_a + t_b}{2}] \\ r^2(\pi - \beta_2) + rd_2 \sin\beta_2 , t \in (\dfrac{t_a + t_b}{2}, t_b] \end{cases} \tag{3.9}$$

$$S_{leave}(t) = \begin{cases} r^2(\pi - \beta_3) + rd_3 \sin\beta_3 , t \in [t_c, \dfrac{t_c + t_d}{2}] \\ r^2\beta_4 - rd_4 \sin\beta_4 , t \in (\dfrac{t_c + t_d}{2}, t_d] \end{cases} \tag{3.10}$$

where $d_1, d_2, d_3, d_4, \beta_1, \beta_2, \beta_3, \beta_4$ are functions with the variable t. Their forms are written in Equation (3.11) and (3.12).

$$d_i = \begin{cases} R\sin(\arcsin\frac{r}{R} - \omega_c(t - t_a)), i = 1 \\ R\sin(\omega_c(t - t_a) - \arcsin\frac{r}{R}), i = 2 \\ R\sin(\arcsin\frac{r}{R} - \omega_c(t - t_c)), i = 3 \\ R\sin(\omega_c(t - t_c) - \arcsin\frac{r}{R}), i = 4 \end{cases} \quad (3.11)$$

$$\beta_i = \arccos\frac{d_i}{r}, i = 1,2,3,4 \quad (3.12)$$

Equations (3.9) and (3.10) indicate that during the incoming phase ($t \in [t_a, t_b]$) and the leaving phase ($t \in [t_c, t_d]$), $S_{income}(t)$ and $S_{leave}(t)$ are not sinusoidal functions. Thus, the received radiation of the PIR sensor $W(t)$ is not sinusoidally modulated. Equation (3.2) does not hold. I define a sinusoidal function $S'(t)$ in the form of

$$S'(t) = \begin{cases} \frac{\pi r^2}{2}\left[1 + \sin\left[\frac{\pi\omega_c}{2\arcsin\frac{r}{R}}(t - \frac{t_a + t_b}{2})\right]\right], t \in [t_a, t_b] \\ \frac{\pi r^2}{2}\left[1 - \sin\left[\frac{\pi\omega_c}{2\arcsin\frac{r}{R}}(t - \frac{t_c + t_d}{2})\right]\right], t \in [t_c, t_d] \end{cases} \quad (3.13)$$

The modeling results of $S(t)$, $S'(t)$ and their difference are presented in Figure 3.11, where $\omega_c = 0.6rad/s$, $r = 4mm$, and $R = 10mm$. The left y-axis represents the overlapped area of $S(t)$ and $S'(t)$, respectively. The right y-axis indicates their relative difference compared to the maximum overlapped area πr^2. The difference does not exceed 5%, and thus, we could make an approximation:

$$S(t) \approx S'(t), t \in [t_a, t_b] \cup [t_c, t_d] \quad (3.14)$$

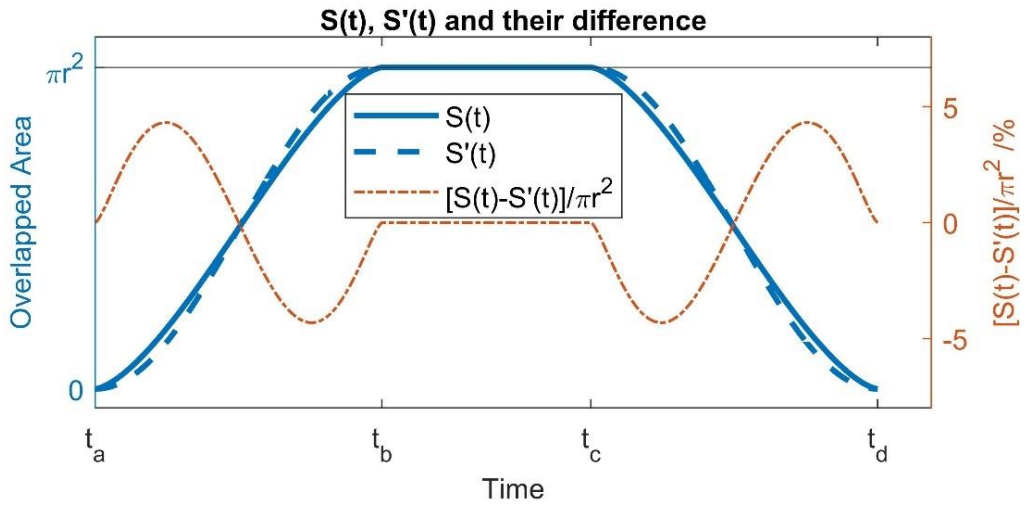

Figure 3.11 The modeling results of *S(t), S'(t)* and their difference when ω_c=0.6rad/s, *r*=4mm, *R*=10mm.

Therefore, the received radiation of the PIR sensor $W(t)$ could be approximated as

$$W(t) \approx I_s S'(t) \tag{3.15}$$

Equation (3.15) indicates that $W(t)$ follows the sinusoidal manner, with a sinusoidal modulation frequency $\omega = \frac{\pi\omega_c}{2\arcsin\frac{r}{R}}$. Thus, the output of the PIR sensor shown in Figure 3.7 follows Equation (3.2). To evaluate the time constants τ_T and τ_E, the relationship between the amplitude of the PIR sensor's output and the sinusoidal modulation frequency ω should be found.

In the experiment, the frequency of the chopper ω_c is in the range of $[0.05, 50.00]$ rad/s. The radius of the chopped radiation is in the range of $R \in [25mm, 45mm]$. The radius of the effective sensing beam is in the range of $r \in [5mm, 8mm]$, respectively.

Thus, the effective modulation frequency ω is in the range of $[0.26, 705.04]$rad/s. Figure 3.12 shows the output $V_{out}(t)$ of the PIR sensor when the chopper rotates at the frequency of $\omega_c = 20.7$rad/s. The curve changes in a sinusoidal manner. The peak-to-peak value is V_{pp}.

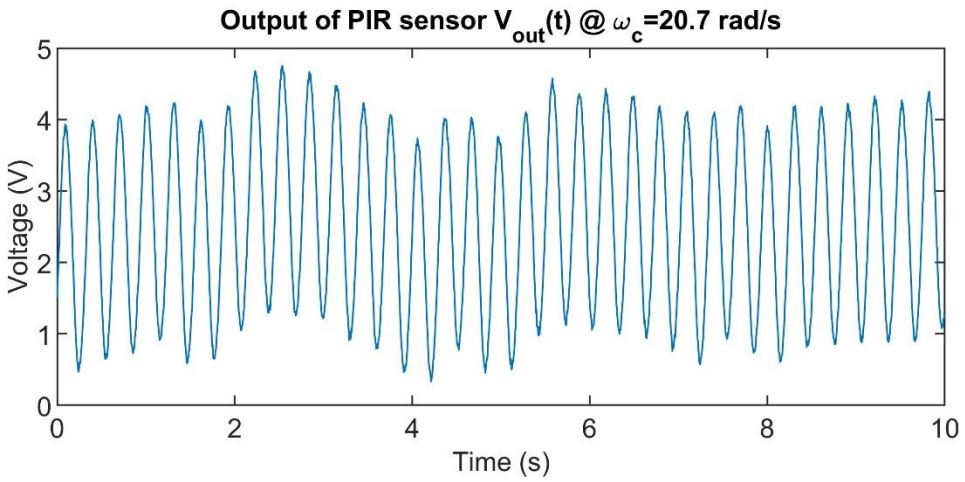

Figure 3.12 The output of the PIR sensor V_{out}(t) when ω_c=20.7 rad/s.

For each ω value, the peak-to-peak value V_{pp} of PIR sensor is recorded. The relationship between the averaged V_{pp} values and the sinusoidal modulation frequency ω is shown in Figure 3.13. The x-axis is on the logarithm scale. The y-axis is in the unit of decibel (dB). The horizontal black line in Figure 3.13 represents the -3dB level from the maximum V_{pp} value. The two intersections between the -3dB level with the V_{pp}-ω curve indicate the values of ω that fullfill $\omega\tau_T = 1$ and $\omega\tau_E = 1$, respectively [7]. Thus, by

determining the value of ω at these two intersections, the corresponding time constants τ_T and τ_E could be derived. As a result,

$$\tau_T \approx 3.6s, \tau_E \approx 3.5ms \tag{3.16}$$

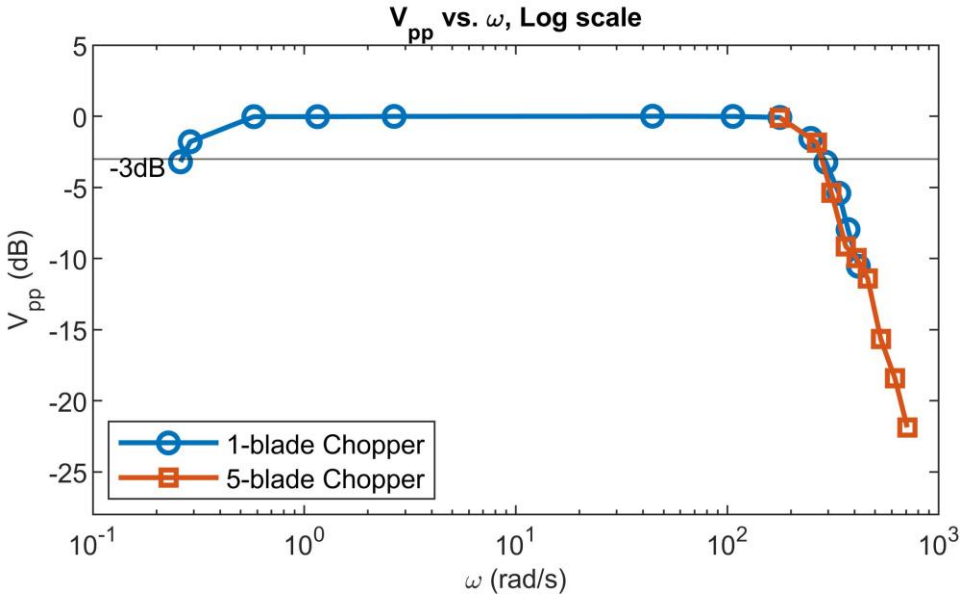

Figure 3.13 The peak-to-peak value of PIR sensor at different sinusoidal chopping frequencies ω.

Now, the time constants of the PIR sensors are evaluated. The next step is to study the remaining two factors in Equation (3.5) and (3.6): $W_{ON} - W_{OFF}$, ω_r and ω_d.

3.4. The Effective Modulation and the Response Time

In this subsection, the measurement methods of the effective modulation and the response time will be introduced.

By observing Equation (3.5) and (3.6), the amplitudes of the sinusoidal function $V_{out,rise}(t)$ and $V_{out,fall}(t)$ are proportional to $W_{ON} - W_{OFF}$. It represents the difference of the infrared radiation transmitted through the PDLC shutter between the ON and the OFF state. The radiation W_{ON} and W_{OFF} can be calculated from the incidental radiation and the transmission rate or contrast ratio of the PDLC shutter $\xi_{ON}(\lambda)$ and $\xi_{OFF}(\lambda)$. The latter can be measured using a Fourier-transform infrared spectroscopy (FTIR) under different driving conditions.

As shown in Figure 3.14 and Figure 3.15, the FTIR spectrometer (Thermo Scientific Nicolet iS5) has a chamber with a light source and a detector placed at both ends. The PDLC shutter is placed at the center of the chamber. The driving signals are connected to the two Ge substrates, respectively. We use a waveform generator and an amplifier to change the frequency and amplitude of the AC voltage signal. The external voltage is provided by a waveform generator (Keysight 33500B) and a voltage amplifier (Trek model 2220). The electric field is in the form of an AC square wave with the frequency f_{AC} and the amplitude V_{rms}, as described in Chapter 3.1.

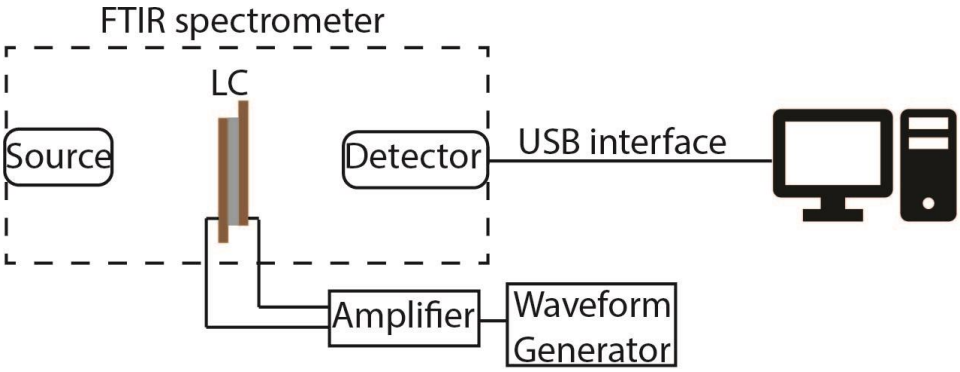

Figure 3.14 FTIR spectrometer measurement setup.

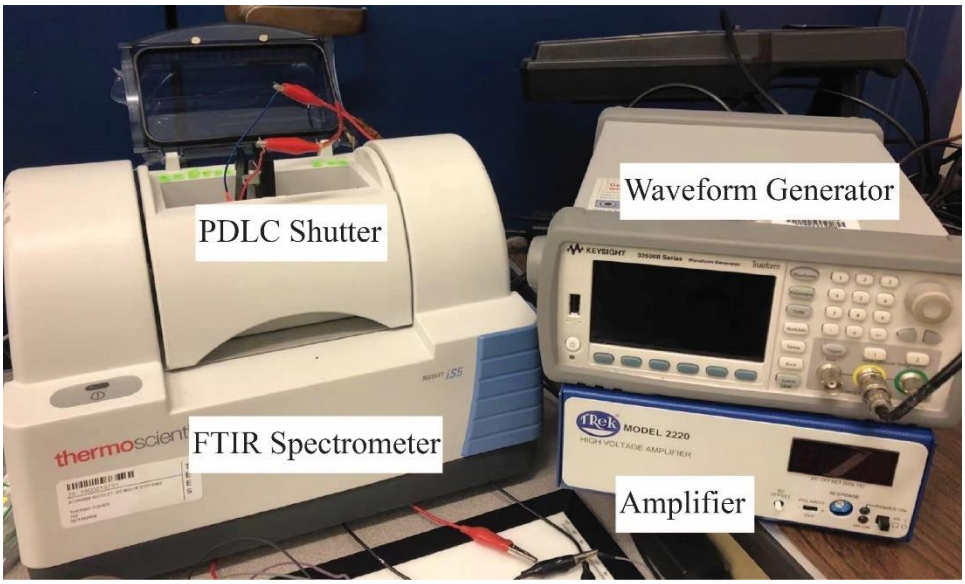

Figure 3.15 The photographic representation of the experimental setup to measure the FTIR spectrums of the PDLC shutter.

The effect of f_{AC} and V_{rms} on the effective modulation is discussed in Chapter 4. Here, we briefly introduce how to measure and calculate the effective modulation. When measuring the FTIR, we first configure the driving frequency f_{AC} from the waveform

generator. Then we start with $V_{rms} = 0$. It takes 18-20 seconds for the FTIR spectrometer to complete and report one measurement of the transmission rate. The reason it takes such a long time is that the spectrometer requires time to change the wavelength by changing the interferometer inside [107, 108] and to compute the measured transmission rate. After the measurement is complete, the wavelength-dependent transmission spectrum will show up on the OMNIC® software, with the range from 2.5μm to 25μm. Next, we control the waveform generator with different voltage amplitudes. Finally, we reduce V_{rms} to zero and repeat the measurement process. Figure 3.16 shows the measured transmission spectrums with different V_{rms} values when the frequency $f_{AC} = 122Hz$. The range on the x-axis is 4-16μm. In the figure, the first five curves in the solid lines with different colors indicate the results with the increasing $V_{rms} = 0V, 2.1V, 5.0V, 9.0V,$ and $10.0V$, respectively. The remaining three curves in the dashed lines represent the spectrums with the decreasing $V_{rms} = 5.0V, 2.1V$ and $0V$, respectively. The LC shutter was fabricated with $\eta = 0.7, d = 26\mu m,$ and the cool rate of 1℃/min. We could observe that, when $V_{rms} = 2.1$V, the transmission rate only changes a little compared to $V_{rms} = 0$V. As the V_{rms} increases, the transmission rate increases until reaches the saturation when V_{rms} is larger than 6.0V. When the amplitude decreases, the transmission rate decreases but are not equal to those when increasing the amplitude. For example, when V_{rms} decreases to zero, the measured transmission rate (dashed blue line) is slightly higher than its initial transmission rate at complete scattering state (solid red line). This might be caused by the hysteresis, the persistence and/or the memory effect, which will be discussed in Chapter 4.2.4 in detail. Here, we could define the transmission rate $\xi_{ON}(\lambda)$ and $\xi_{OFF}(\lambda)$ to be the

transmission spectrums when the transmission rate saturates and when V_{rms} decreases to zero, respectively.

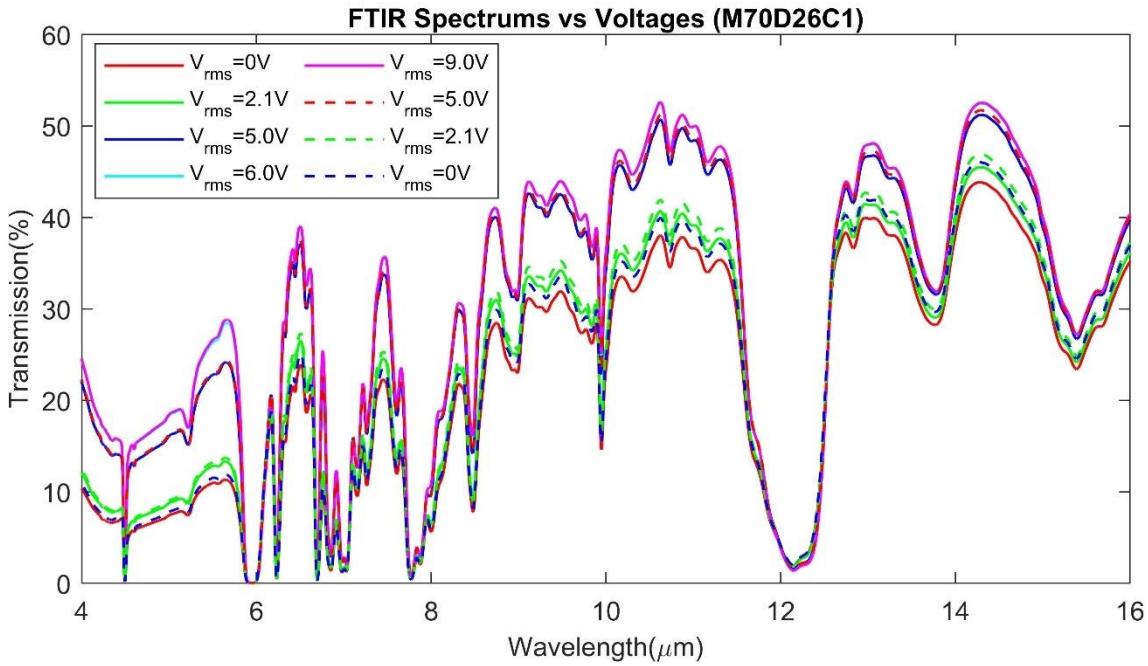

Figure 3.16 The FTIR Spectra of the LC shutters fabricated with η=0.7, d=26μm and the cool rate of 1°C/min at under different driving voltages.

We denote the infrared radiation before and after the PDLC shutter is W and W_T. Based on Planck's law [109], any object in the FOV with a surface temperature of T will emit radiance power (in the unit of watt) per unit area of the body, per unit solid angle of emission, and per unit wavelength:

$$B(\lambda, T) = \frac{hc^2}{\lambda^5} \quad \frac{1}{exp\left(\frac{hc}{\lambda k_B T}\right) - 1} \tag{3.17}$$

where h is the Planck constant; c is the speed of light; k_B is the Boltzmann constant.

The transmitted radiation power W_T in a wavelength range $[\lambda_1, \lambda_2]$ is:

$$W_T = \int_{\lambda_1}^{\lambda_2} B(\lambda)\xi(\lambda)d\lambda \tag{3.18}$$

Here, $\xi(\lambda)$ is the wavelength-dependent transmission spectrum of the PDLC shutter. Specifically, $\xi_{ON}(\lambda)$ and ξ_{OFF} are the transmission spectrums for the ON and the OFF state, respectively.

$$W_{ON} = \int_{\lambda_1}^{\lambda_2} B(\lambda)\xi_{ON}(\lambda)d\lambda$$
$$W_{OFF} = \int_{\lambda_1}^{\lambda_2} B(\lambda)\xi_{OFF}(\lambda)d\lambda \tag{3.19}$$

Due to the hysteresis, the persistence and/or the memory effect of the PDLC shutters [110-113], after removing the electric field for a certain time, the transmission rate will still be slightly higher than that its initial transmission rate at complete scattering state. As illustrated in Figure 3.17 (a), applying the voltage to a PDLC shutter increases W_T from the initial state (marked by the black box) to the ON state (marked by the red circle). After removing the voltage, W_T decreases gradually until it reaches a stable value (marked by the blue triangle). Figure 3.17 (b) illustrates the change of W_T after removing the voltage. The OFF state is determined by the moment when W_T changes less than 1% after the removal of the voltage. The time required to reach the OFF state will be discussed in Chapter 4.2.4.

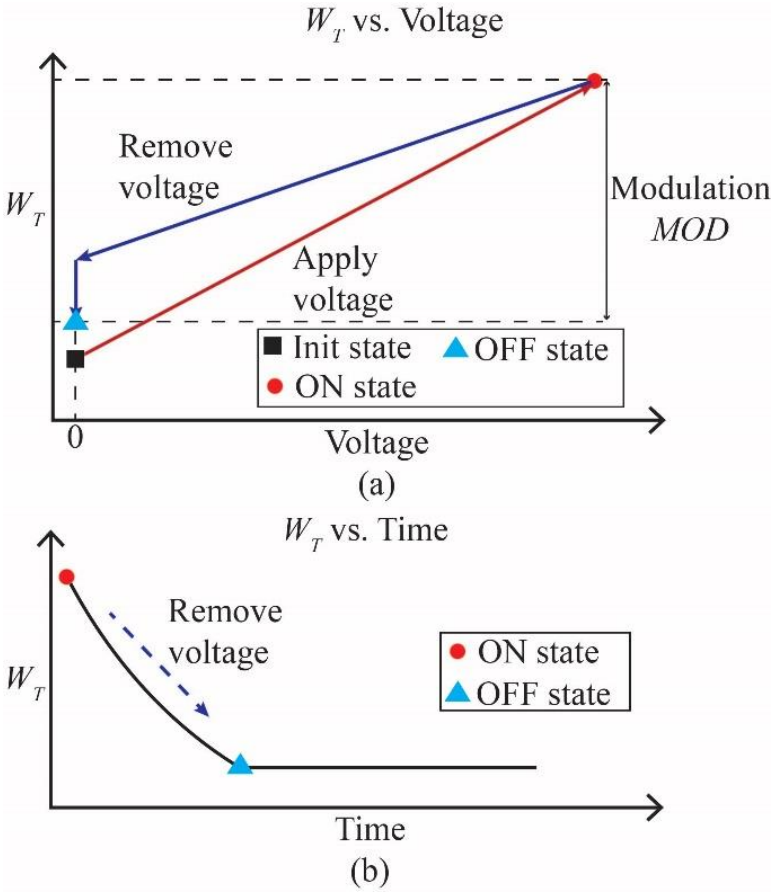

Figure 3.17 The transmitted radiation W_T (a) changes after applying and removing the voltage, and (b) decreases and reaches a relative stable state after removing the voltage for a certain amount of time.

To better quantifying the changes of the transmitted energy, we use the effective modulation, MOD to represent the difference of the transmitted infrared radiation between the ON and the OFF state, as shown in Figure 3.17.

$$MOD = W_{ON} - W_{OFF} = \int_{\lambda_1}^{\lambda_2} B(\lambda)[\xi_{ON}(\lambda) - \xi_{OFF}(\lambda)]d\lambda \tag{3.20}$$

In this dissertation, we use $[\lambda_1, \lambda_2]$ = 8-12μm as the integration bandwidth where the human skin radiates the most [39, 114] like a blackbody in this region [114, 115]. In Chapter 4.2.4, we will characterize the persistence and the memory effect. We use cycling to reduce the time to be stable as well as the transmission difference between the initial and the OFF states.

Next, we discuss the modulation frequency ω_r and ω_d shown in the model described by Equation (3.5) and (3.6). Before that, the response time of the PDLC infrared shutter will be introduced. The response time is the time required for a PDLC shutter to change from one state to another state. For PDLC infrared shutters, two types of response time are defined: the rise time τ_r and the decay time τ_d. The rise time is the time in which transmission rate of the PDLC shutter rises from 10% to 90% after the electric field is applied. Similarly, the decay time is when its transmission rate falls from 90% to 10% after the electric field is removed [58, 59]. The visualization to of the response time is shown in Figure 3.18. The red curve shows the "rising phase", which means the PDLC shutter changes from the OFF to the ON state. The blue curve represents the "falling phase", where the PDLC shutter changes from ON to OFF state. To simplify the model, the relationship between the modulation frequency ω_r and ω_d and response time τ_r and τ_d is shown below:

$$\omega_r = \frac{\pi}{\tau_r}$$
$$\omega_d = \frac{\pi}{\tau_d} \tag{3.21}$$

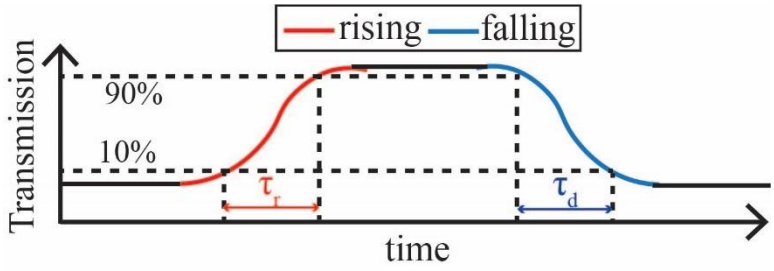

Figure 3.18 Definition of the response time.

Although the FTIR spectrometer could measure the transmission rate with high wavelength resolution, it takes too long (tens of seconds) for one single measurement to calculate the response time. Thus, in this experiment, we use a photovoltaic detector with an amplifier to measure the response time of PDLC infrared shutters [56, 65, 68]. The output of the photodetector is linear to the received infrared radiation and its measurement is much faster (3 nanoseconds) so that its response is concurrent with that of the PDLC shutter.

The experimental setup is shown in Figure 3.19(a) and (b), where the PDLC shutter with the control circuit is placed between a blackbody radiation source (ThermoWorks, IR-500) and the InAsSb photovoltaic detector (P13894-011MA) with an amplifier (C4159-01). The blackbody radiation source has a surface temperature of 80℃. The distance between the blackbody source to the PDLC shutter is set to be 5cm. This setup could help increase the signal-noise ratio by increasing the input radiation power. The AC voltage applied on the PDLC shutter is controlled by a manual push button. An oscilloscope will read the output from the amplifier.

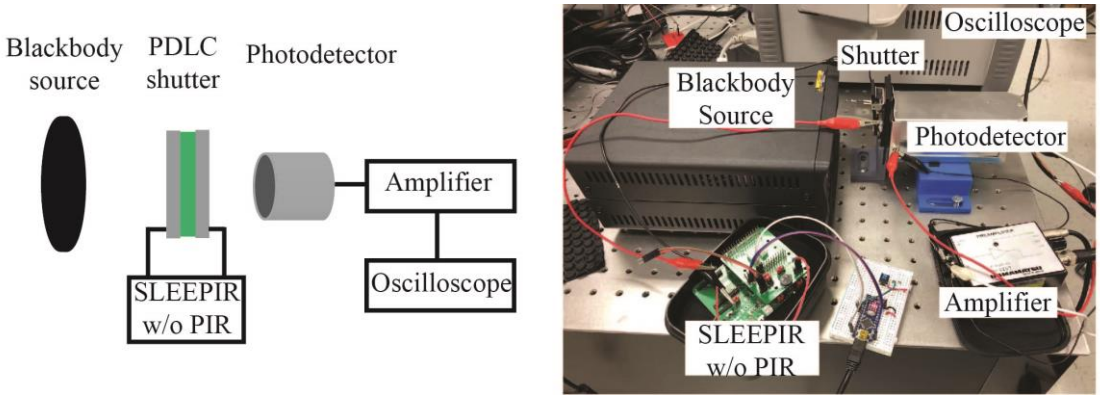

Figure 3.19 Test setup of the photodetector to measure the response time.

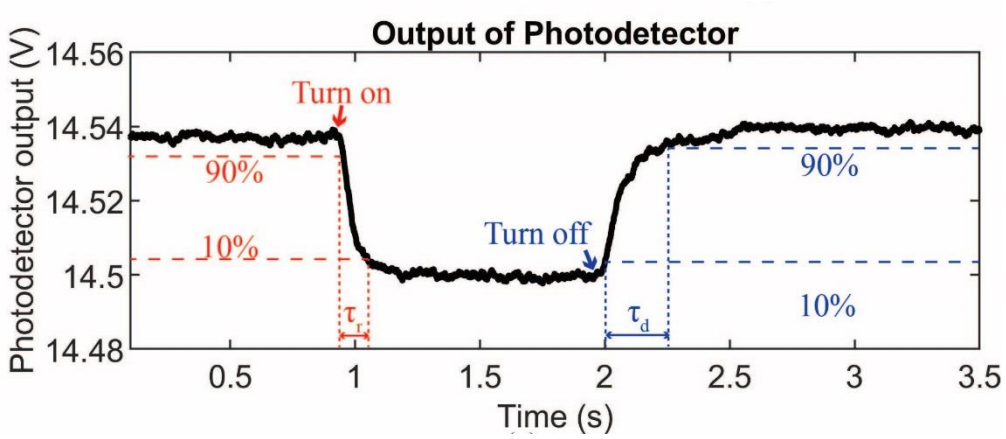

Figure 3.20 Output of the photodetector to calculate the response time.

After turning on and off the AC voltage, the output voltage from the photodetector is shown in Figure 3.20. The label "turn on" and "turn off" indicate the time instances when we change the state of the PDLC shutter by pushing the button. As described earlier, the rise time τ_r and the decay time τ_d are calculate by the 10% and 90% levels of the

photodetector's output, as shown in Figure 3.20. In Chapter 4.3, we will characterize the impact of the driving and the fabrication conditions on the response time.

3.5. Discussion and Summary

In this chapter, the SLEEPIR sensor module is designed by placing a PDLC infrared shutter in front of a traditional analog PIR sensor. The PDLC infrared shutter is driven by an AC voltage. By applying or removing the AC voltage, the transmission of the PDLC shutter will change accordingly.

The SLEEPIR sensor module's output model is developed by analyzing the working principle of the PIR sensor and quantifying the change of transmission of the PDLC shutter. The model shows that the output depends on three factors: the difference of the transmitted radiation between the ON and the OFF state, which is denoted by the effective modulation MOD, the response time of the PDLC shutter, which indicates how fast the radiation changes when changing the state of the PDLC shutter, and the time constants of the analog PIR sensor.

We designed a rotating optical chopper to measure the time constants of the PIR sensors. They are the thermal time constant τ_T of the pyroelectric material and the electrical time constant τ_E of the preamplifier circuit. More specifically, we measure the frequency response of the PIR sensor and determine the time constants by finding out the -3dB level. As a result, $\tau_T = 3.6s, \tau_E = 3.5ms$.

Finally, the measurement methods of the effective modulation MOD and response time are introduced. The effective modulation MOD is calculated by the transmission spectrums of the ON and OFF states. The transmission rate of a PDLC shutter will change

when the amplitude of the AC voltage changes. Specifically, the transmission will increase as V_{rms} increases until it reaches saturation while reduces after removing the applied electrical field. However, it will not reduce to its initial transmission rate at complete scattering state even after a certain time due to the hysteresis, the persistence and/or the memory effect. Note that, here W_{OFF} represents the transmitted power measured when it decreases and reaches a relative stable level. It is slightly higher than the transmitted power at the complete scattering state. The effective modulation MOD is defined to be the difference between the transmitted radiation of the ON and the OFF state. To precisely measure the response time, an infrared photodetector is used. The rise time τ_r and the decay time τ_d are calculated by determining the 10% and the 90% level of the photodetector's output.

From the model of the SLEEPIR sensor module, we know that besides the time constants of the PIR sensor, the effective modulation MOD and the response time will impact the output of the SLEEPIR sensor module. If the object that radiates infrared power does not change, then the effective modulation MOD and the response time only depend on the PDLC infrared shutter itself. To be specific, the morphology of the LC droplets in the PDLC cell will impact the MOD and the response time. The morphology is dependent on the fabrication conditions, which include the mass ratio η of the LC material compared to the PDLC material, the cell gap d of the PDLC shutter, and the cooling rate during the phase separation. When using the PDLC infrared shutter, the driving voltage will also impact the effective modulation. In Chapter 4, we will quantify the impact of these

fabrication and driving conditions to identify the optimal condition that maximizes the SLEEPIR sensor module's output.

4. PERFORMANCE OPTIMIZATION OF THE SLEEPIR SENSOR MODULE

From the model develop in Chapter 3, the output of the SLEEPIR sensor module depends on the effective modulation MOD, and the modulation frequency of the rising and falling phase ω_r and ω_d of the PDLC shutter, and the time constants τ_T and τ_E of the PIR sensor. Here ω_r and ω_d can be calculated from their response time τ_r and τ_d as shown in Equation (3.21). The time constants of the PIR sensor were also characterized in Chapter 3.

In this chapter, we will characterize the effective modulation and the response time of the LC shutter, which represent how much and how fast the transmitted radiation changes when the state of the PDLC shutter changes, respectively.

The effective modulation and the response time of PDLC shutters, were extensively studied by researchers in the past, but mainly focused on the visible region [94, 116]. As introduced in Chapter 2.2.4, their modulation capacity is largely depending on their scattering effect. The LC droplets within the polymer will scatter incident light when no electric field is present. A single-droplet model of a PDLC shutter [117, 118] show that the level of applied voltage will alter the direction of LC droplets, and thus the scattering and propagation of light. The morphology of the droplets, such as their sizes, shape, density, also have impact on their modulation and response time [110, 117, 119-121]. The morphology is determined by the fabrication condition, including the mass ratio, the cell gap, the cooling rate, polymer type, etc. We use TIPS with SIPS, to fabricate our PDLC shutters, as shown in Figure 2.23. Here, three fabrication conditions are studied and

compared: the mass ratio η, cell gap d and the cooling rate (CR). The mass ratio is the mass percentage of E7 LC material within the PDLC mixture, ranging from 0 to 1. The cell gap is controlled by the glass beads with different diameters, which are placed between the Ge substrates. A thermal stage (Instec MK2000) with a resolution of 0.01°C is used to control the cooling rate.

For each PDLC shutter, we define the name convention following the order of the mass ratio, the cell gap, the cooling rate, and the index. For example, M80D22C1.5-3, represents the PDLC shutter prepared with the mass ratio of 80%, the cell gap of 22 μm, and the cooling rate of 1.5℃/min and this is the 3rd sample prepared under such condition.

In this chapter, we firstly show how morphology changes with different fabrication conditions. Next, the effective modulation MOD and the response time of the PDLC shutters are measured and analyzed. Specifically, their dependences on the driving and the fabrication condition are studied. Then, the optimal factors enabling the maximum output of the SLEEPIR sensor module are obtained. Finally, the lifetime of the PDLC shutters is shown.

4.1. Morphology of PDLC Shutters

The morphology, which shows the distribution of the LC droplets within the polymer film, is studied. The substrates must be transparent to visible light so that the polarized image microscope could take images. However, the proposed infrared shutter uses Ge substrates due to its high transmission in the LWIR region but opaque in the visible region [98]. To solve this issue, we prepare the glass-based PDLC shutters at the same time when preparing the Ge-based shutters. The recipe and process are identical,

including the mass ratio η, cell gap d, and cooling rate. The only difference is that we use the indium tin oxide (ITO) coated glasses instead of the Ge substrates. The ITO is widely used as electrodes deposited on surfaces, such as glasses [122, 123].

The polarized microscope images are taken by the LEICA DM 6B microscope system. Figure 4.1 shows the microscope image of 5 glass based PDLC shutters, named M60D22C2-G1, M60D22C1-G1, M70D22C2-G1, M70D22C1-G1, and M80D22C1-G1, respectively. The letter "G" represents that the sample is made with ITO glasses. From these images, we could see that at the same mass ratio, the droplet size will increase with a slower cooling rate. At the same cooling rate, the droplet size will increase when the mass ratio increases.

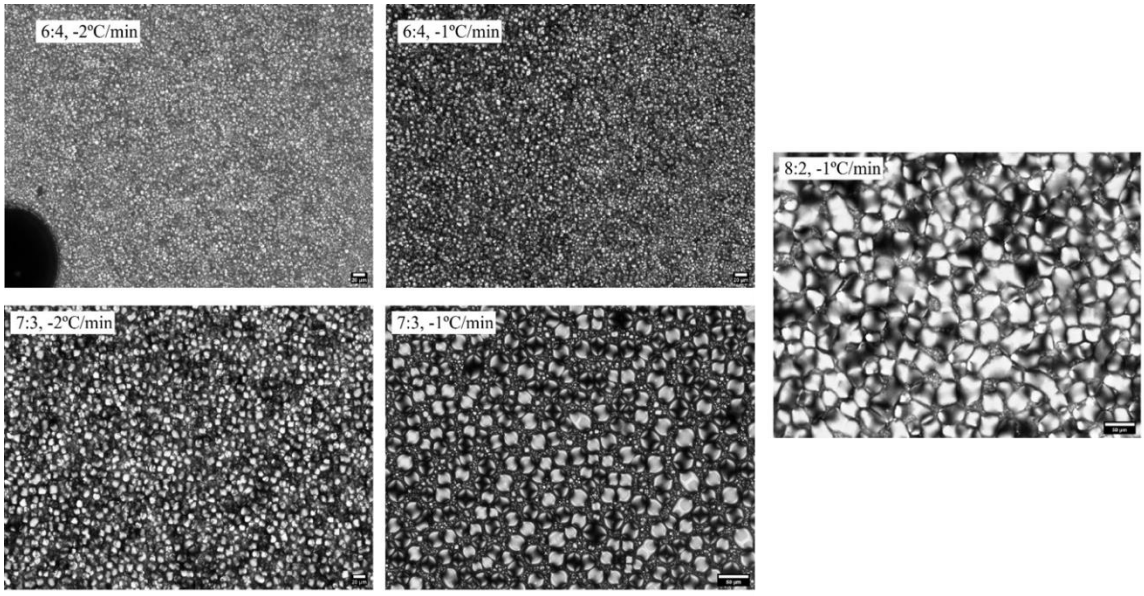

Figure 4.1 Polarized light images of PDLC cells with ITO-glass substrates.

More glass based PDLC shutters are made with different conditions, and the measurement results are shown in Table 4.1. The mass ratio η is from 60% to 80%, while the cell gap d varies from 12-32 μm. For each sample, we measure the diameters of 20 randomly selected droplets. The fifth and the last columns of Table 4.1 show the average droplet size with the standard deviation, respectively. Similarly, the droplet size increases with a slower cooling rate. At the same cooling rate, the droplet size will increase when the mass ratio increases. This observation agrees with the findings in [102, 124].

Table 4.1 The measured droplet size of PDLC cells with glass substrates.

Sample name	η (%)	Cell gap d (μm)	Cooling rate (°C/min)	Average droplet size (μm)	Standard deviation (μm)
M60D22C1	60	22	1	5.01	1.50
M60D22C2	60	22	2	3.52	0.74
M70D22C1	70	22	1	11.71	1.86
M70D22C2	70	22	2	8.56	1.47
M75D22C1	75	22	1	12.78	2.21
M75D22C2	75	22	2	11.83	1.84
M80D22C1	80	22	1	23.31	2.99
M80D22C2	80	22	2	21.71	3.24
M80D12C1	80	12	1	20.06	2.67
M80D32C1	80	32	1	23.83	3.01

4.2. Effective Modulation of PDLC Infrared Shutters

Equations (3.5), (3.6) and (3.20) indicate that the effective modulation $MOD = W_{ON}\text{-}\, W_{OFF}$, plays an important part in determining the output of the SLEEPIR sensor module. Chapter 3.4 introduces the measurement approaches of W_{ON} and W_{OFF}. This subsection will study the impact of the driving and the fabrication conditions on the effective modulation MOD.

4.2.1. Effect of the Driving Voltage Amplitude

At the first step, we will look at the impact of the driving voltage amplitude V_{rms}. The PDLC shutters used here are fabricated with $\eta = 0.8$, CR= 1°C/min and d = 12, 22, 32, and 50 μm. The setup to measure the effective modulation is shown in Figure 3.14. The PDLC shutter is placed in the center of the FTIR spectrometer. The AC voltage is generated by a waveform generator and a voltage amplifier. The frequency of the voltage is chosen at $f_{AC} = 200Hz$ to make sure MOD saturates, which will be introduced in Chapter 4.2.2. We record each FTIR spectrum when decreasing the voltage amplitudes from 7 to 0 Volt at a step of around 1 Volt. The corresponding transmitted radiation W_T, calculated by using Equation (3.18) is shown in Figure 4.2(a). We could observe that W_T values of both the ON and the OFF states decrease with a larger cell gap. The persistence effect of these shutters is very small, which means that W_T reaches a relatively stable level once V_{rms} decreases to zero. The reason is that these shutters have been cycled for a long time (>100,000 cycles). The effect of cycling on the persistence will be introduced in Chapter 4.2.4.

Figure 4.2(b) shows the MOD-V_{rms} curves for difference cell gaps. Each curve is calculated by subtracting W_T when $V_{rms} = 0V$ from the W_T-V_{rms} curve in Figure 4.2(a). We can see MOD decreases when V_{rms} decreases, until reaching zero. Also, MOD will saturate when V_{rms} is larger than a certain value, which is called the saturation voltage V_{sat}. We could observe that the saturated voltage increases with larger cell gaps, as shown in Figure 4.2(c).

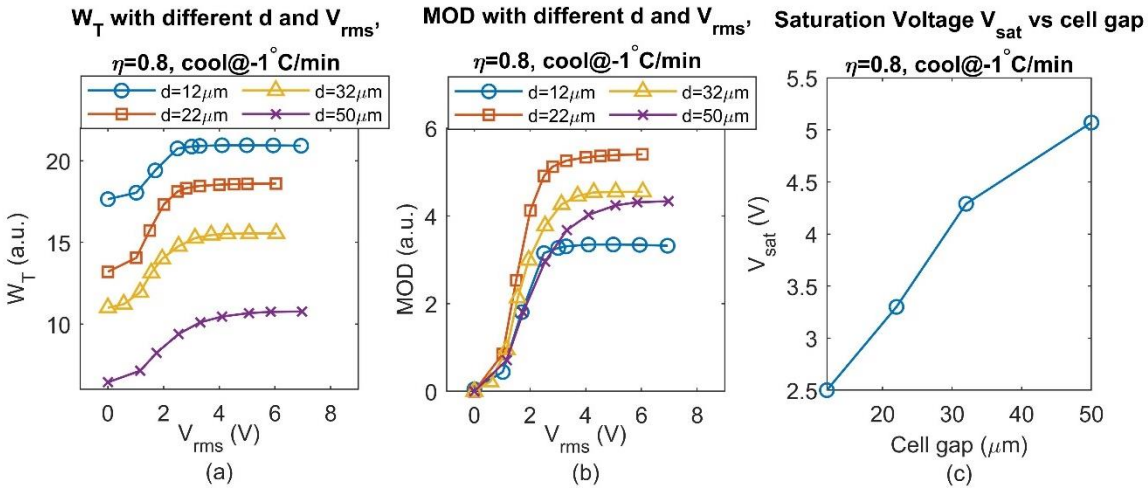

Figure 4.2 (a) The difference of the transmitted radiation W_T and (b) the effective modulation MOD with different driving voltages and cell gaps when the cooling rate is 1°C/min. (c) The relationship between the saturated voltage V_{sat} and the cell gap.

In practice, we use a printed circuit board (PCB), with an MCU, a DC-to-DC converter, and a driving circuit to provide the driving voltage. The MCU will control the frequency f_{AC} and ON-OFF time of the PWM signal. The DC-to-DC converter will boost the battery voltage (3V from 2 AA batteries) to the desired level VB, which is introduced

in Chapter 3.1. The driving circuit, shown in Figure 3.2, will convert the PWM signal from the MCU to the AC voltage connected to the PDLC shutter. The choice of VB is important for the PCB to drive the PDLC shutter. The result shown in Figure 4.2 could help to determine the level of VB. In the end, the VB is chosen to be 10V, which is enough for PDLC shutters to reach the saturation.

4.2.2. Effect of the Driving Frequency

Not only the driving voltage amplitude V_{rms} will affect MOD, the driving frequency f_{AC} will also affect MOD. This is because of the dielectric property of the PDLC shutter. A PDLC film could be modeled as a capacitor and resistor in parallel [125], as shown in Figure 4.3. After considering the resistor of the Ge substrates, we could develop the analogy between the PDLC shutter and a passive electrical circuit. The PDLC composite can be illustrated as a parallel plate capacitor. Here, two substrates (ITO glasses or Ge windows) act as two parallel electrodes. The PDLC composite is a dielectric material.

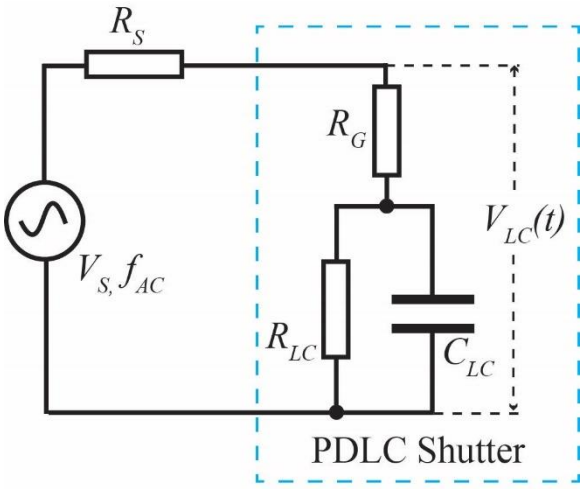

Figure 4.3 The equivalent circuit of the PDLC shutter.

Since the applied voltage on the PDLC shutter is an AC voltage, we only consider the DC phase, where the applied AC voltage increases from zero to V_{rms}. Here V_{rms} is the amplitude of the voltage source. The equivalent resistance of the driving circuit is R_s. The equivalent resistance and capacitance of the PDLC shutter is R_{LC} and C_{LC}, respectively. The equivalent resistance of the Ge substrates is R_G. We denote the effective voltage applied on the PDLC shutter to be $V_{LC}(t)$. After solving the equivalent circuit, $V_{LC}(t)$ can be derived as:

$$V_{LC}(t) = V_1 - V_2 e^{-\frac{t}{\tau_{LC}}} \tag{4.1}$$

Here, V_1 and V_2 are in the forms of

$$V_1 = \frac{R_G + R_{LC}}{R_s + R_G + R_{LC}} V_{rms} \tag{4.2}$$

$$V_2 = \left(\frac{R_s}{R_s + R_G} - \frac{R_s}{R_s + R_G + R_{LC}}\right) V_{rms} \tag{4.3}$$

The time constant of this RC circuit is $\tau_{LC} = (R_s + R_G)R_{LC}C_{LC}/(R_s + R_G + R_{LC})$.

From Equation (4.1), we notice that the voltage between two Ge substrates of the PDLC shutter will show exponential decay. In this section, the driving voltage is provided by an MCU (Arduino), a DC-DC converter (LTC3459) and the driving circuit. We compared the effect of different driving frequency f_{AC} = 31300Hz, 3900Hz, 980Hz, 490Hz, 244Hz, 122Hz and 30Hz. Their corresponding open circuit and closed loop voltage applied on the PDLC shutter are shown in Figure 4.4, respectively. The open circuit is the condition when the PDLC shutter is disconnected physically from the driving circuit. The closed loop is the circuit shown in Figure 4.3. The range on the x-axis is scaled into the same region [0, 0.6 ms] for better visualization. When $t = 0$, we could notice that the $V_{LC}(0)$ is not equal to zero. The reason is that R_G will show a voltage at this time instance. Notice that when f_{AC} =31300Hz, the period is $1/f_{AC} = 0.03ms$, which is much shorter than the scaled range of x-axis. Thus, the closed loop voltage $V_{LC}(t)$ will drop before it could start increasing as Equation (4.1). For slower frequencies, when the switch is closed at $t = 0$, $V_{LC}(t)$ in the closed loop condition will increase in the exponential decay manner until it reaches the maximum value. The maximum value of $V_{LC}(t)$ in the closed loop is equal to the maximum value of open circuit condition. In this experiment, the maximum value is 10V since this is the amplitude of the provided AC voltage. We use the curve fitting to evaluate the parameters in Equation (4.1). The result shows that the

PDLC shutter (M80D22C1-1) used in this experiment has the following curve fitting parameters, $V_1 = 10.22V$, $V_2 = 5.32V$, the time constant $\tau_{LC} = 0.99 \times 10^{-4}s$.

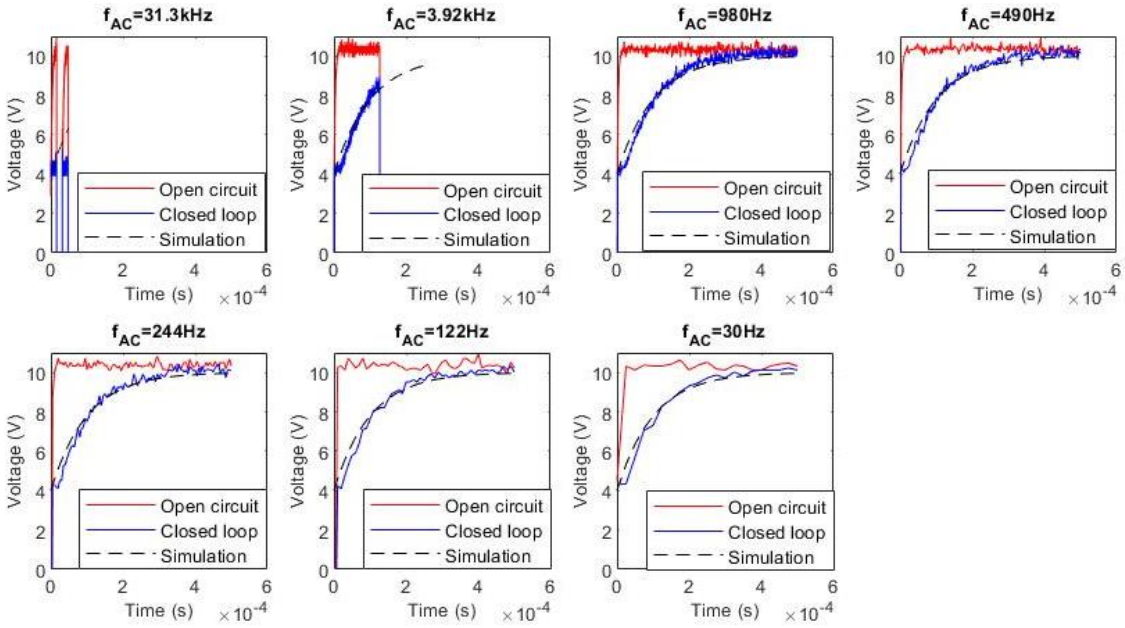

Figure 4.4 The open circuit and the closed-loop voltage with different f_{AC}.

Four more PDLC shutters have been measured with the same procedure and the corresponding curve fitting parameters are shown in Table 4.2. These fitted parameters are similar for multiple PDLC shutters. The differences may come from the different resistance at the interface between the electrodes and the Ge substrates.

Table 4.2 Curve fitting parameters V_1, V_2 and τ_{LC} of four PDLC shutters.

PDLC Shutter	V_1 (V)	V_2 (V)	τ_{LC} (s)
M80D22C1-5	10.30	5.70	0.94×10^{-4}
M80D22C1-6	10.26	5.63	1.01×10^{-4}
M80D22C1-7	10.19	5.69	1.07×10^{-4}
M80D22C1-8	10.18	5.41	0.96×10^{-4}

Next, the effect of f_{AC} on the effective modulation MOD is tested. Four PDLC shutters are used in this experiment. The amplitude of the AC voltage is 10V. The calculated MOD is shown in Figure 4.5 with different driving frequencies. These shutters show small persistence effect and memory effect due to large cycle numbers, which will be discussed in Chapter 4.2.4. From this figure, when f_{AC} decreases, MOD will increase. When f_{AC} is less than 980Hz, MOD will reach saturation.

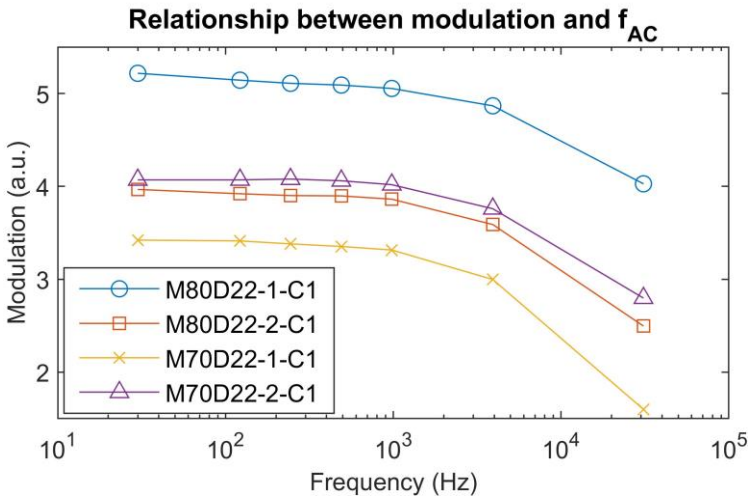

Figure 4.5 The effective modulation *MOD* with different driving frequencies f_{AC} of four PDLC shutters.

One explanation is that the effective voltage $V_{LC}(t)$ shows different maximum values when f_{AC} changes. As shown in Figure 4.4, for each period of AC voltage, $V_{LC}(t)$ cannot reach a large value when the driving frequency is high. From [42, 68, 96], we know that MOD is depending on the V_{rms}. For low V_{rms}, MOD cannot reach the saturated region. For the following study, we choose $f_{AC} = 122Hz$. The reason is that a lower frequency will have longer pulse width. For example, when f_{AC} is 30Hz, the period of one AC pulse is 33ms. This is close to the response time of the PDLC shutter, which will be discussed in Chapter 4.3.

This subsection introduces the equivalent RC model of the PDLC shutter. The effective voltage applied on the PDLC shutter shows exponential decay. A higher frequency f_{AC} will reduce the amplitude of the effective voltage V_{LC}, thus decrease MOD.

From Chapter 4.2.1 and 4.2.2, the driving condition that could maximize MOD for the PDLC shutter is found to be V_{rms} =10V and $f_{AC} = 122Hz$.

4.2.3. Effect of Cell Gap, Mass Ratio, and Cooling Rate

After determining the driving signals' amplitude V_{rms} and frequency f_{AC}, the next step is to study the impact of fabrication conditions on the effective modulation. Mass ratio η is selected from three values 75%, 80%, and 85%. The cell gap d has five options: 12μm, 22 μm, 26 μm, 32 μm, and 50 μm. The cooling rate is from 0.5 to 2.0 ℃/min. We prepared four samples for each combination of the three fabrication factors. The driving signals' amplitude V_{rms} and frequency f_{AC} is 10V and 122Hz, respectively. The reason for choosing η within 75%, 80%, and 85% is that, for lower or higher mass ratio, the effective modulation will be much smaller.

Figure 4.6 shows the effective modulation of PDLC shutters with different fabrication conditions. Each marker represents the average MOD of four samples. The error bar represents the standard deviation of these four samples. For the samples with $\eta = 0.75$ and $\eta = 0.85$, PDLC shutters with four cell gaps are prepared. The cooling rate is from 0.75 to 1.5℃/min. For the samples with $\eta = 0.8$, PDLC shutters with five cell gaps and seven cooling rates (0.5 to 2℃/min) are prepared. The range of the y-axis of all three subplots in Figure 4.6 is scaled to the same range for better visualization.

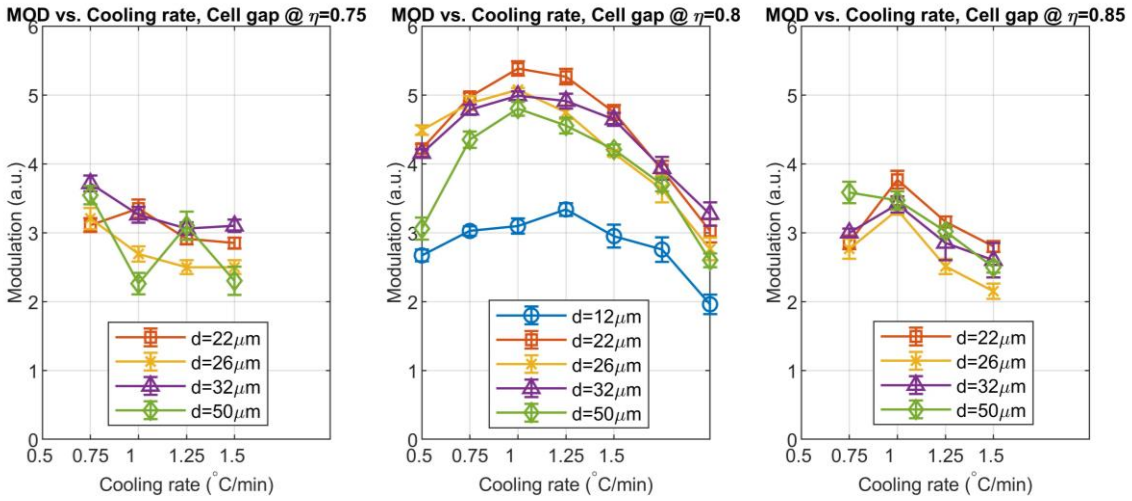

Figure 4.6 Effective modulation *MOD* with different cell gaps, mass ratios, and cooling rates.

Firstly, the highest MOD happens with the condition when $\eta = 0.8$, $d = 22\mu m$, cooling rate equals 1 or 1.25°C/min, which is significantly higher than cooling with lower or higher rates. The average MOD for the PDLC shutters with 1°C/min (5.38±0.10) is slightly higher than those with 1.25°C/min (5.26±0.11). But considering the error bar, these two cooling rates have a similar result.

Secondly, we study the impact of the mass ratio η. Under the same cell gap and the cooling rate, the effective modulation with $\eta = 0.75$ and $\eta = 0.85$ is lower than $\eta = 0.8$. The explanation is that, for a lower mass ratio, the droplet size is small. From Table 4.1, the droplet size is 12.78±2.21μm. The scattering effect of this size is smaller than those with $\eta = 0.8$. Thus, in the OFF state, the overall transmission rate of PDLC shutters with $\eta = 0.75$ is higher than those with $\eta = 0.8$, which reduces the difference in the transmitted radiation between the ON and OFF state. The droplet size is much larger for a

higher mass ratio than the LWIR wavelength (~ 50 μm), which will reduce the efficiency of scattering [101].

Thirdly, for PDLC shutters with $\eta = 0.8$, small or large cell gaps both lead to a low MOD. For small cell gaps, one explanation is because the shape of the droplets is not a sphere. The length that is vertical to the substrates is smaller than the length that is parallel with the substrates. For a large cell gap (d=50μm), the large thickness will decrease the transmitted rate even in the ON state [126]. During the OFF state, the backscattering, which is the energy that radiates back to the incident direction, will increase with a larger cell gap [100]. These two effects will reduce MOD.

Finally, for PDLC shutters with $\eta = 0.8$, the cooling rate will change the droplet size. According to [102], a faster cooling rate will decrease the size of the LC droplets. However, the scattering model based on [101] shows that there exists an optimal droplet size that will maximize the scattering efficiency. The radius of the droplet size R_D and the wave number k_w ($k_w = 2\pi/\lambda$) will impact the scattering cross section σ_s. The model in [101] indicates that when $k_w R_D \approx 19$, the scattering cross-section will be maximized. This result leads to the optimal droplet size for the scattering is $R_D(\lambda) = \frac{8.5}{\pi}\lambda$. In the LWIR region, the optimal droplet size is from 21μm to 32μm. From Table 4.1, the droplet size measured from the glass-based PDLC shutters with the condition of $\eta = 0.8, d = 22\mu m$, cooling rate=1°C/min, is $23\mu m$. Although we could not observe the droplet size of germanium-based PDLC shutters due to the opaque in visible light region, we could imply that the cooling rate of 1 or 1.25°C/min will make the most droplet size within this range.

4.2.4. Effect of Cycling

When characterizing the MOD of the PDLC shutters, we observe that the effective modulation becomes much more stabilized after applying and removing the AC voltage repeatedly (cycling). For instance, the transmitted radiation of a freshly made PDLC shutter does not immediately drop to its original level at the complete scattering as soon as we remove the applied electric field due as aforementioned in Chapter 3.4. The transmitted radiation W_T of this PDLC shutter (M80D22C1-5), calculated by Equation (3.18), will take more than 150 seconds to be relatively stable, as shown in Figure 4.7. The stabilized W_T level is also not equal to the value at the complete scattering state, but higher, due to the hysteresis, the persistence or the memory and persistence effect [110-113].

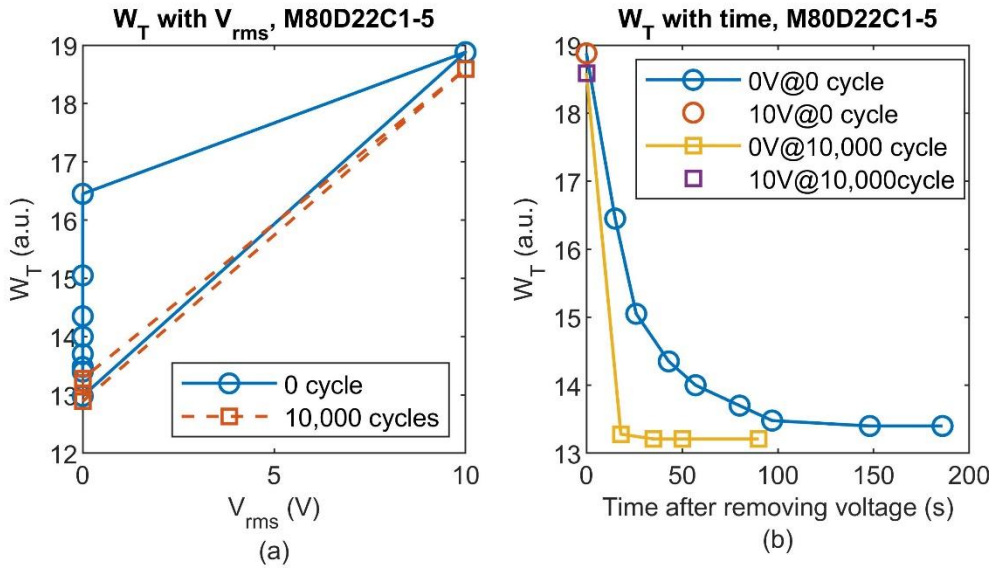

Figure 4.7 (a) Measured W_T when applying and removing the AC voltage for different cycling numbers of a PDLC shutter. (b) W_T changes after removing voltage for different cycling numbers.

The hysteresis effect is mainly caused by the orientation mechanism of the LC droplet direction. When applying or removing the AC voltage, the directions of LC molecules located at the polymer-LC interface and inside the LC droplets, will show difference [112]. Also, the hysteresis may come from the residual electric charge after removing the electrical field [127].

The persistence is mainly caused by the high interconnectivity between LC droplets. For example, during the droplets' reorientation process, when we apply the AC voltage, some distributed droplets will connect and then trapped in the high-field state, which creates the defect structure [103]. After removing the electric field, the connected droplets cannot return to the complete scattering state immediately. That is the W_{OFF} of freshly fabricated PDLC shutters is always higher than the transmitted power at the complete scattering state.

The memory effect or the semi-permanent persistence effect [128] is mainly due to the anchoring force between the boundaries of the polymer network and the LC domain [129].

We observed that cycling could help reduce the time needed to help the PDLC shutter returns to its complete scattering state. As shown in Figure 4.7, after the PDLC shutter has been cycled for 10,000 times, it only takes 18 seconds to reach the stability. Note that the time of 18 seconds is the minimum interval between two FTIR measurements. More samples are shown in Table 4.3. Here, $W_{T,init}$, W_{ON}, and W_{OFF} values, are the calculated transmitted radiation W_T for the initial state, ON state, and OFF state, respectively. The initial state is the state before applying the voltage, as shown in Figure

3.17. It is worth to mention that the last column shows the difference between the W_{OFF} and $W_{T,init}$, which may reflect the persistence or the memory effect. After cycling, the time required to stabilize after removing the voltage decreases significantly. The last four samples in Table 4.3 have been cycled for around 100,000 cycles. The results show that after 100,000 cycles, $W_{OFF} - W_{T,init}$, close to zero, which reveals that cycling may help to reduce either the hysteresis, the persistence, or the memory effect. The reason behind this may be the cycling could reduce the interconnectivity between LC droplets.

Table 4.3 The calculated $W_{T,init}$, W_{ON}, W_{OFF}, the stabilized time, *MOD*, and W_{OFF}-$W_{T,init}$ of eight PDLC shutters.

Sample	Cycle No.	$W_{T,init}$	W_{ON}	W_{OFF}	Stabilized Time (s)	*MOD*	$W_{OFF} - W_{T,init}$
M80D22C1-5	0	12.98	18.88	13.40	148	5.52	0.42
	10,000	12.89	18.59	13.21	18	5.38	0.32
M80D22C1-6	0	12.50	18.30	12.97	152	5.33	0.47
	10,000	12.88	18.5	13.21	18	5.29	0.34
M80D22C1-7	0	13.1	18.95	13.55	160	5.40	0.45
	10,000	13.21	18.78	13.50	20	5.28	0.29
M80D22C1-8	0	12.74	18.69	13.24	160	5.45	0.50
	10,000	13.01	18.78	13.38	19	5.40	0.37
M80D22C1-9	0	12.82	18.38	13.21	310	5.67	0.39
	10,000	12.59	18.15	12.83	20	5.32	0.24
	100,000	12.27	17.88	12.28	18	5.30	0.01
M80D22C1-10	0	12.82	19.04	13.11	281	5.93	0.29
	10,000	12.58	18.60	12.78	32	5.82	0.20
	100,000	12.31	18.16	12.34	19	5.82	0.03
M80D22C1-11	0	12.29	18.61	12.91	187	5.70	0.62
	10,000	12.46	18.21	12.66	22	5.55	0.20
	100,000	12.61	18.22	12.70	18	5.52	0.09
M80D22C1-12	0	12.65	18.65	13.17	202	5.48	0.52
	10,000	12.82	18.46	13.08	30	5.38	0.26
	100,000	12.45	17.85	12.47	20	5.38	0.02

4.3. Response Time of PDLC Infrared Shutters

Response time of the PDLC shutter is another important factor that affects the SLEEPIR output. Response time is the time required by the LC molecules to align along the electric field upon applying the field and relax to their initial orientation at the complete scattering state. As described in Section 3.4, two types of response time, the rise time τ_r and the decay time τ_d, are defined. Mathematically [59],

$$\frac{1}{\tau_r} = \frac{\Delta\varepsilon}{\gamma_1 d^2} V_{rms}^2 + \frac{k(l^2-1)}{\gamma_1 a^2} \tag{4.4}$$

$$\frac{1}{\tau_d} = \frac{k(l^2-1)}{\gamma_1 a^2} \tag{4.5}$$

where $\Delta\varepsilon$ is the dielectric anisotropy of the LC; γ_1 is the rotational viscosity of LC; k is the elastic constant; $l = a/b$ is the aspect ratio of the droplet; a and b are the length of the major and minor axes of the LC droplet, respectively. The properties of the PDLC film morphology, which include droplet size, shape, multiple scattering processes, etc., have a high impact on the response time of the PDLC composite film [112, 130].

4.3.1. Effect of the Driving Voltage Amplitude

Firstly, we will study the effect of the AC voltage amplitude on the response time. According to Equation (4.4) and (4.5), the higher voltage amplitude will decrease the rise time τ_r, but it will not affect the decay time τ_d. By observing these two equations, notice that

$$\Delta\frac{1}{\tau} = \frac{1}{\tau_r} - \frac{1}{\tau_d} = \frac{\Delta\varepsilon}{\gamma_1 d^2} V_{rms}^2 \tag{4.6}$$

The result for the PDLC shutter with the fabrication condition of M80D32C1 is shown in Figure 4.8. The left y-axis represents the response time τ_r and τ_d in the unit of second. The right y-axis is the difference between the reciprocals of τ_r and τ_d, which is defined by $\Delta\frac{1}{\tau}$. The x-axis is the square of the voltage amplitude V_{rms}. The result shows that the rise time will decrease with the increasing voltage amplitude. The decay time τ_d is not change much with different amplitudes. Also, good linearity is found between $\Delta\frac{1}{\tau}$ and V_{rms}^2. The R^2 value of the linear fitting is 0.98.

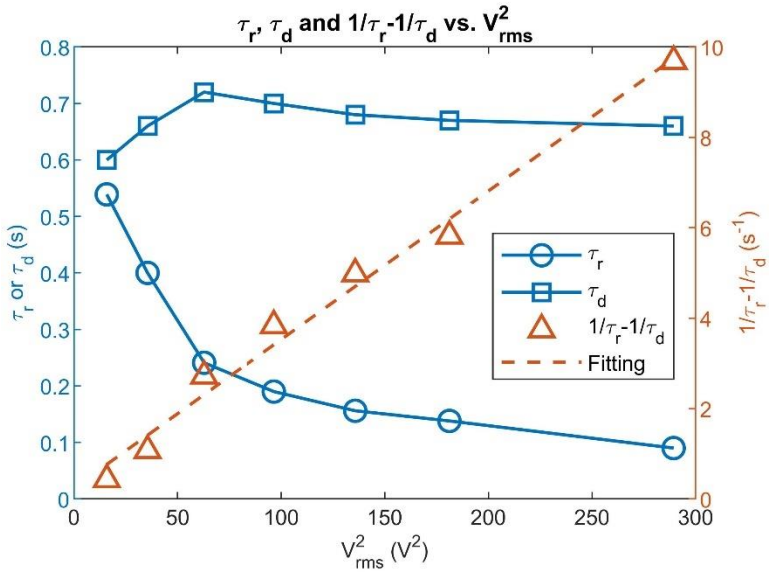

Figure 4.8 The response time τ_r, τ_d, and $1/\tau_r$-$1/\tau_d$ with different V_{rms}. The dash line is the linear fitting. The fabrication condition of the PDLC shutter is η=0.8, d=32μm, cool@1°C/min.

4.3.2. Effect of the Cell Gap, the Mass Ratio, and the Cooling Rate

Next, we study the impact of the fabrication condition of the PDLC shutters on the response time. Similarly, the mass ratio η is selected from three values 75%, 80%, and 85%. The cell gap d has five options: 12μm, 22 μm, 26 μm, 32 μm, and 50 μm. The cooling rate is from 0.5 to 2.0 °C/min. We prepared four samples for each combination of the three conditions. The driving signal' amplitude V_{rms} and frequency f_{AC} is 10V and 122Hz, respectively.

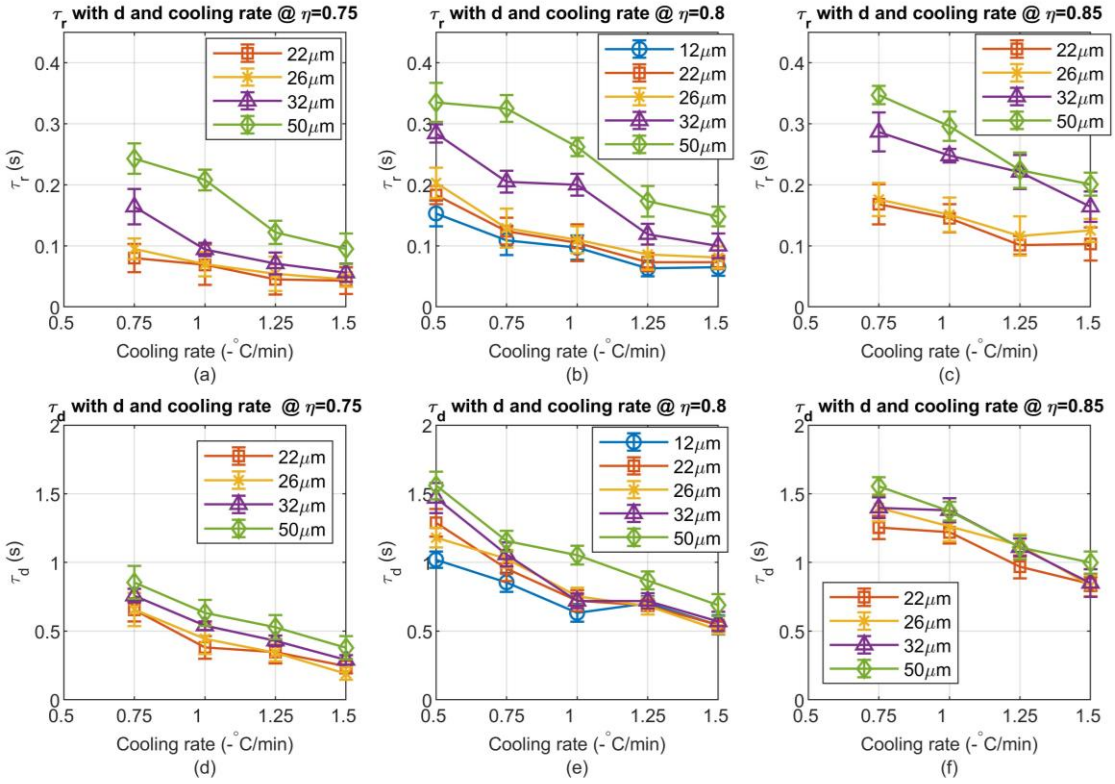

Figure 4.9 Response time with different cell gap, mass ratio, and cooling rate. (a-c) shows the τ_r with mass ratio of 0.75,0.8 and 0.85 respectively. (d-f) shows the τ_d with mass ratio of 0.75, 0.8 and 0.85 respectively.

Figure 4.9 shows the response time of PDLC shutters fabricated under different conditions. The range of the y-axis of all three subplots in Figure 4.9 is scaled to the same range for better visualization.

From the figure, when the mass ratio and the cooling rate are the same, the response time will increase with a larger cell gap. Specifically, the rise time τ_r shows higher dependency than the decay time τ_d. The reason is that from Equation (4.4), τ_r is related with cell gap d. Although τ_d does not depend on the cell gap d in Equation (4.5), it is still affected by the droplet size. From Table 4.1, the droplet size slightly increases with a larger cell gap d, which will increase the decay time τ_d in return. When the cooling rate and the cell gap are the same, both the rise time and the decay time increase with a higher mass ratio η. The reason is that larger η will increase the droplet size significantly, as indicated in Table 4.1. The effect of the cooling rate is also obvious: the faster cooling rate will reduce both the rise and the decay time due to the decrease in the droplet size.

4.4. Optimal Factors of the SLEEPIR Sensor Module

We now have a better understanding on how the effective modulation and the response time of PDLC shutters behave under different fabrication conditions. Our next step is to evaluate the performance of the SLEEPIR sensor module and determine optimal fabrication condition that could maximize the output of the SLEEPIR sensor module.

Figure 4.10 shows the output of a SLEEPIR sensor module when the PDLC shutter changes its state. When the PDLC shutter changes in the rising phase (from OFF to ON), the SLEEPIR sensor module's output will decrease from the baseline to a negative peak. Then the signal goes back to the baseline. During the falling phase (from ON to OFF), the

SLEEPIR sensor module's output will increase from the baseline to a positive peak, then returns to the baseline value. We denote the difference between the baseline and the negative peak to be V_r (<0), the difference between the baseline and the positive peak to be V_d (>0). The sign of V_r and V_d are determined by the polarity of the sensing elements exposed, as shown in Figure 1.3. The difference between the positive peak and the negative value is $V_{pp} = |V_r - V_d|$. The baseline, which is represented by the horizontal black dashed line in Figure 4.10, is select to be 1.14V, which is the average value of the analog PIR sensor's output when there is no motion detected. Notice that according to Equation (3.5) and (3.6), V_r and V_d are the amplitude of $V_{out,rise}(t)$ and $V_{out,decay}(t)$.

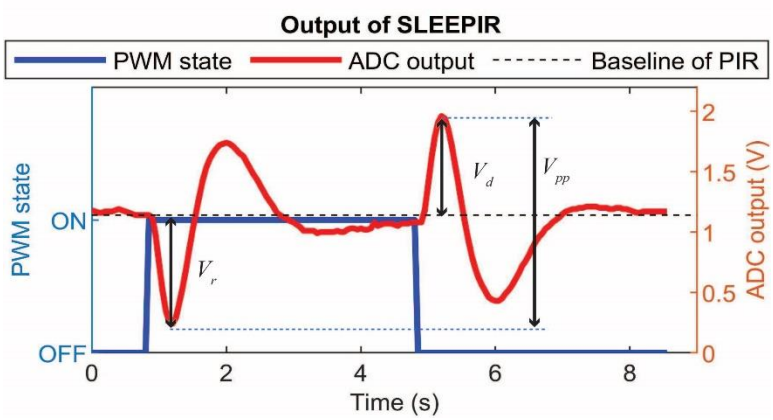

Figure 4.10 Output of the SLEEPIR module.

The objective function to find the optimal fabrication condition is represented by

$$\eta, d, CR = \arg\max V_{pp} \tag{4.7}$$

The next step is to validate the SLEEPIR sensor output model in Equations (3.5) and (3.6), and to find the optimal fabrication condition. We denote two terms $A_{V,r}$ and $A_{V,d}$:

$$A_{V,r} = \frac{\omega_r \cdot MOD}{(1+\omega_r{}^2\tau_T^2)^{\frac{1}{2}}(1+\omega_r{}^2\tau_E^2)^{\frac{1}{2}}} \tag{4.8}$$

$$A_{V,d} = \frac{-\omega_d \cdot MOD}{(1+\omega_d{}^2\tau_T^2)^{\frac{1}{2}}(1+\omega_d{}^2\tau_E^2)^{\frac{1}{2}}} \tag{4.9}$$

Note that, $A_{V,r}$ and $A_{V,d}$ are the theoretical amplitudes of $V_{out,rise}(t)$ and $V_{out,decay}(t)$ indicated by Equation (3.5) and (3.6). Thus, the measured peak-to-peak value V_{pp} should be proportional to $\Delta A_V = A_{V,r} - A_{V,d}$.

$$V_{pp} \propto \Delta A_V \tag{4.10}$$

Equation (4.7) becomes

$$\eta, d, CR = \arg\max\left\{ MOD\left[\frac{\omega_r}{(1+\omega_r{}^2\tau_T^2)^{\frac{1}{2}}(1+\omega_r{}^2\tau_E^2)^{\frac{1}{2}}} + \frac{\omega_d}{(1+\omega_d{}^2\tau_T^2)^{\frac{1}{2}}(1+\omega_d{}^2\tau_E^2)^{\frac{1}{2}}} \right] \right\} \tag{4.11}$$

In the experiment, sixteen PDLC shutters are prepared with eight different fabrication conditions. The mass ratio is $\eta = 0.8$. The cell gap d is from 22 to 32μm. The cooling rate varies from 0.75 to 2°C/min. The reason to choose $\eta = 0.8$ is that compared to other mass ratios (0.75 and 0.85), MOD is at least 30% higher with the same cell gap and the same cooling rate, while the remaining part in Equation (4.11) changes less than 1%. We consider the function $F_\tau(\omega_\tau)$

$$F_\tau(\omega_\tau) = \frac{\omega_\tau}{(1+{\omega_\tau}^2\tau_T^2)^{\frac{1}{2}}(1+{\omega_\tau}^2\tau_E^2)^{\frac{1}{2}}} \tag{4.12}$$

where ω_τ is defined by $\omega_\tau = \pi/\tau$, and response time τ could be either the rise time or the decay time. From all the samples we have prepared under different conditions, the range of the rise time τ_d is from 0.03s to 0.38s. The change on $F_\tau(\omega_\tau)$ when $\tau_r \in [0.03s, 0.38s]$ is from 0.272 to 0.285, with only a 1% difference. The range of the decay time τ_d is from 0.2s to 1.6s. The change on $F_\tau(\omega_\tau)$ for different τ_d is from 0.282 to 0.285, with only a 1% difference. Thus, $A_{V,r}$ and $A_{V,d}$ are dominated by the MOD in comparison with the response time.

The setup to measure V_{pp} of the SLEEPIR sensor module with sixteen different PDLC shutters is shown in Figure 4.11. The SLEEPIR sensor module is placed in front of a blackbody radiation source. The position of the SLEEPIR sensor module and the blackbody source do not change during the test. The surface temperature of the blackbody source is set to be 26°C to make sure that the measured V_{pp} is within the detection range of the PIR sensor. The effective modulation and the response time are measured with the same procedure described in Chapter 3.4. Note that all the sixteen PDLC shutters in this experiment are cycled for more than 10,000 cycles.

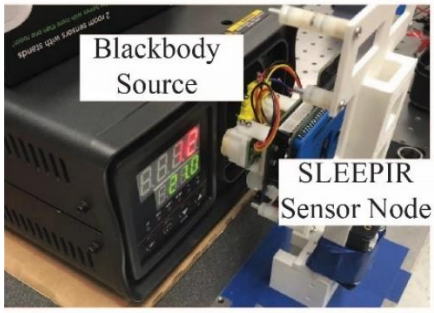

Figure 4.11 The setup to measure the output of the SLEEPIR module.

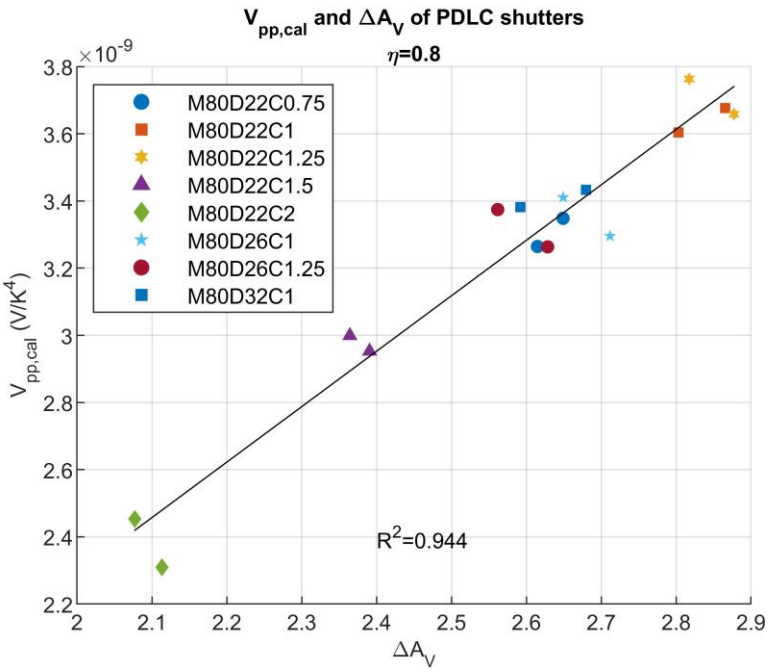

Figure 4.12 Relationship between $V_{pp,cal}$ and ΔA_V for PDLC shutters.

After collecting the measured V_{pp}, the effective modulation MOD and the response time for each PDLC shutter, and their relationship with ΔA_V and V_{pp} could be found.

Before that, the measured V_{pp} should be calibrated by the temperature difference between the sensor and the blackbody. The reason is that the net radiation flux received by the SLEEPIR sensor module is proportional to $T_{bb}^4 - T_s^4$ when the position of the SLEEPIR sensor module and the blackbody source do not change [106]. Here, T_{bb} and T_s are the absolute temperature of the blackbody source and the SLEEPIR sensor module, respectively. The temperature of the SLEEPIR sensor module is collected by an onboard temperature sensor. We calibrate the measured V_{pp} with

$$V_{pp,cal} = \frac{V_{pp}}{T_{bb}^4 - T_s^4} \tag{4.13}$$

The results between $V_{pp,cal}$ and ΔA_V are shown in Figure 4.12. Each point represents the result from one PDLC shutter. The markers with the same color and shape belong to the PDLC shutters with the same fabrication condition.

We could observe that there exists a good linearity between $V_{pp,cal}$ and ΔA_V. The R^2 of the fitting is 0.944. This result verifies that the model for the SLEEPIR sensor module is correct. Then, by observing the $V_{pp,cal}$ of different PDLC shutters, the optimal fabrication condition is found to be $\eta = 0.8$, $d = 22\mu m$, CR=1 or 1.25 °C/min. The reason that CR has two optimal values is that the result of the PDLC shutters cooled at 1 or 1.25 °C/min cannot be separated statistically.

Table 4.4 The measured $V_{pp,cal}$, the linear fitted value and their discrepancy for PDLC shutters under eight fabrication conditions.

Fabrication Conditions	Average Measured $V_{pp,cal}$ $(\frac{10^{-9}V}{K^4})$	Average Fitted $V_{pp,cal}$ $(\frac{10^{-9}V}{K^4})$	Difference $(\frac{10^{-9}V}{K^4})$ and percentage
M80D22C0.75	3.306	3.336	0.030 (1.0%)
M80D22C1	3.640	3.670	0.040 (1.1%)
M80D22C1.25	3.711	3.691	0.020 (0.5%)
M80D22C1.5	2.976	2.915	0.061 (2.1%)
M80D22C2	2.381	2.449	0.068 (2.8%)
M80D26C1	3.353	3.415	0.062 (1.8%)
M80D26C1.25	3.319	3.275	0.044 (1.3%)
M80D32C1	3.407	3.342	0.065 (1.9%)

Table 4.4 shows the average measured $V_{pp,cal}$, the predicted $V_{pp,cal}$ using the linear fitting and their discrepancy of two PDLC shutters under the same fabrication condition. The percentage difference is shown in the last column. From this table, we observed that the linearity between $V_{pp,cal}$ and ΔA_V is good.

4.5. The Lifetime of the PDLC Shutters

Another factor that needs to be considered when evaluating the performance of the PDLC shutter is the lifetime. PDLC films in display applications show excellent stability with more than 3 million cycles [131]. In this section, the lifetime of the PDLC shutters is

studied by evaluating the output of the SLEEPIR sensor module after cycling. In practical application, the SLEEPIR sensor module installed on the SLEEPIR sensor node should be switched frequently. For example, if the measurement period (turn on and off the PDLC shutter once) is 10 minutes, the total switch period in five years is $5 \times 365 \times 24 \times 6 = 262{,}800$ cycles. In this experiment, the PDLC shutter on the SLEEPIR sensor module is cycled for different numbers. The output of the SLEEPIR sensor module is recorded while being placed in front of a blackbody radiation source, as shown in Figure 4.11. The temperature of the blackbody radiation source is 26°C. The temperature of the SLEEPIR sensor module is also recorded. The cycle period is 8 seconds to accelerate the experiment. We calculated the calibrated peak-peak values $V_{pp,cal}$ of several PDLC shutters with different cycle numbers. In this study, a PDLC shutter fails when $V_{pp,cal}$ drops to 90% of its full capacity.

Figure 4.13 shows the measured $V_{pp,cal}$ of six PDLC shutters after different cycle numbers. The result shows that after 250,000 cycles of usage, these shutters do not fail and maintain a relatively stable performance.

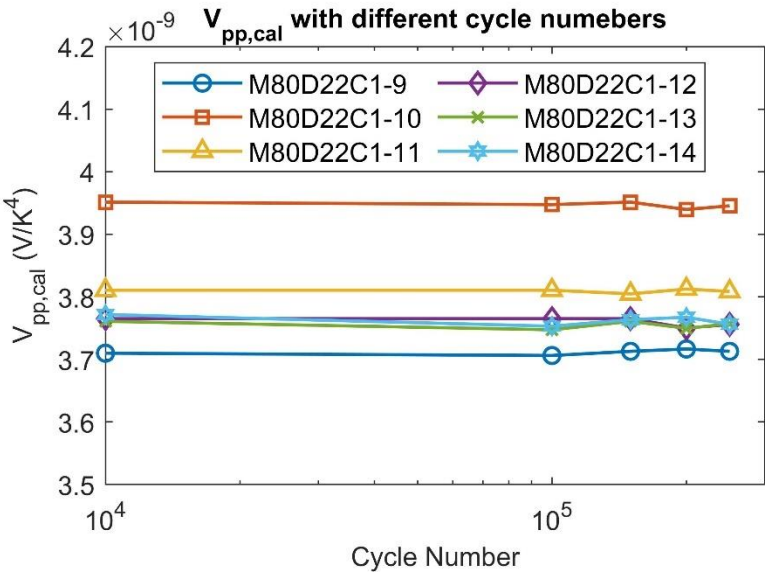

Figure 4.13 $V_{pp,cal}$ with different cycle numbers.

4.6. Discussion and Summary

In this chapter, our goal is to find the optimal fabrication and driving conditions of the PDLC shutter that optimize the output of the SLEEPIR module.

Firstly, the morphology of glass based PDLC shutters is studied via microscope images. The result shows that the droplet size increases with a slower cooling rate and a larger mass ratio.

Next, the effective modulation MOD of the PDLC shutters is studied systematically. The MOD will increase with a larger voltage amplitude until reaching the saturation. The saturated voltage V_{sat} increases with a larger cell gap. The result shows that in practical application, 10V is enough to make the PDLC shutters saturate. Then, the impact on the driving frequency is studied by modeling the PDLC shutter as a capacitor

and a resistor in parallel. The MOD will decrease at a higher frequency f_{AC}. When $f_{AC} < 980Hz$, MOD will saturate. Under the same driving condition, the impact of the fabrication condition, including the cell gap, the mass ratio, and the cooling rate, on MOD is discussed. The result shows that the highest effective modulation is with the fabrication condition when $\eta = 0.8$, $d = 22\mu m$, and the cooling rate equals 1 or 1.25°C/min. The effective modulation with $\eta = 0.75$ and $\eta = 0.85$ is lower than those with $\eta = 0.8$. Also, small or large cell gaps lead to low MOD. PDLC shutter shows the hysteresis, the persistence and/or the memory effect upon removing the AC voltage. The experiment shows that the cycling could reduce the persistence effect and memory effect. Specifically, cycling could reduce the time for the transmission rate to reach a stable level after removing the driving voltage. The difference of the transmission rate between the initial state and the OFF state, also reduces with a larger cycling number.

Then, the response time is studied. The result shows that the rise time will decrease with the increasing voltage amplitude, while the decay time τ_d does not change much, which agrees with Equation (4.4) and (4.5). Also, a good linearity is found between $\Delta\frac{1}{\tau}$ and V_{rms}^2. The impact of the fabrication condition on the response time is studied systematically. Response time will increase with a larger cell gap and a larger mass ratio η.

The optimal factor to fabricate the PDLC shutters is determined in Chapter 4.4. Several PDLC shutters are prepared with different conditions. After measuring V_{pp}, MOD and the response time for each shutter, the relationship between the calibrated $V_{pp,cal}$ and ΔA_V are found. The good linearity indicates the correctness of the model of the SLEEPIR

sensor module described in Chapter 3.2. Meanwhile, the optimal fabrication condition that generates the highest $V_{pp,cal}$, is $\eta = 0.8$, $d = 22\mu m$, CR=1 or 1.25 °C/min.

Finally, the lifetime of the PDLC shutters is discussed. The result shows that the output of the SLEEPIR is stable after 250,000 cycles, which represents five years of usage if the measurement period is 10 minutes.

Some open questions could be discussed for future research.

Firstly, there are several sources of manual error when preparing the PDLC shutters. (1) When moving the mixture of LC, polymer, and chloroform on the Ge substrate, the mixture's actual volume may vary due to the fast evaporation rate of chloroform. (2) The cleanness of the Ge substrates cannot be guaranteed, especially for those substrates recycled from the previous PDLC shutters. (3) The uncertainty of the cell gap. The cell gap is controlled by the glass beads with desired diameters. However, there will be slight differences in the actual diameters.

Secondly, the measurement error from the FTIR spectrometer and the infrared photodetector will cause uncertainty of the result. The position of the PDLC shutter when measuring the FTIR spectrums may differ for each measurement. In the future, we could design a precise holder to make sure each PDLC shutter will be located at the same position for each measurement. When measuring the response time, the photodetector's output that measures the response time is sensitive to electromagnetic disturbance, airflow, and vibration. One solution is to conduct the experiment in an environment with less disturbance, such as an electromagnetic shielding chamber [132]. Another solution is to

increase the signal-noise ratio (SNR) by using an infrared light source with a high power density, such as CO_2 lasers [133].

Thirdly, there is noise and error of the PIR sensor and the ADC converter. When measuring the output of the SLEEPIR, we use the ADC on the microcontroller to read the voltage. There are several solutions. (1) Choose a PIR sensor with high sensitivity. (2) Design a noise filtering circuit after the PIR sensor. (3) Use a separate ADC converter with high resolution and low noise to collect analog signals.

Finally, the persistence effect and memory effect will affect the falling phase if the effective modulation cannot reach the original level shortly. Some researchers suggest that we could alter: (1) the polymer material for the PDLC shutter; (2) Physical properties of LC such as optical and dielectric parameters, rotational viscosity, temporal characteristics, etc. [120, 121, 134, 135].

5. PRESENCE DETECTION USING THE SLEEPIR SENSOR NODE[*†]

The characteristics of the PDLC infrared shutter and optimal condition have been studied in the previous chapters. In this chapter, we characterize the occupancy detection accuracy of the proposed SLEEPIR sensor module. Firstly, the sensor node is designed, consisting of a SLEEPIR sensor module, a digital PIR sensor, a microcontroller, and DC-to-DC converters. Then, the working principle and the power consumption of the SLEEPIR sensor node are introduced. Next, two types of tests are conducted. The first type is the controlled lab test, where the environmental condition is relatively stable during the test. The occupants perform predefined activities. The second type is the uncontrolled test, where the environmental factors and occupants' activities are not controlled. For the lab test, the machine learning approach is introduced and shows a higher accuracy over the traditional threshold method. For the uncontrolled test, environmental factors, especially the room temperature, are considered. A thermal transfer model of the SLEEPIR sensor module is developed. Then, to improve the detection accuracy, an adaptive detection algorithm is introduced. Finally, a comparison between our proposed detection system and commercial products is made.

---

[*] Part of this chapter is reprinted with permission, from L. Wu, Y. Wang, "True Presence Detection via Passive Infrared Sensor Network Using Liquid Crystal Infrared Shutters", *Proceedings of the ASME 2020 Conference on Smart Materials, Adaptive Structures and Intelligent Systems*, 2020.

[†] Part of this chapter is reprinted with permission, from L. Wu, and Y. Wang, "Stationary and moving occupancy detection using the SLEEPIR sensor module and machine learning", *IEEE Sensors Journal*, pp. 1-1, 2021. Copyright © 2021 IEEE.

5.1. Sensor Node Design

A SLEEPIR sensor module consists of a PDLC infrared shutter, an analog PIR sensor, and the driving circuit, as described in Chapter 3.1. The first version of SLEEPIR sensor module is devised as shown in Figure 5.1(a). The frame is 3D printed using Polylactic acid (PLA). The PDLC shutter is hold by two metal screws. The two Ge substrates (20mm diameter, 1mm thickness, Shenyang Ebetter Optics Co., Ltd.) are in contact with the screws, so that these two screws conduct two channels of AC signals generated from the driving circuit.

The devised SLEEPIR sensor node consists of a Bluetooth MCU (EFR32BG13, Silicon Labs), a battery, a DC-DC upconverter (3V to 10V, LTC3459, Analog Devices), a SLEEPIR module, and a traditional PIR sensor (AMN24112, Panasonic), as shown in Figure 5.1(b).

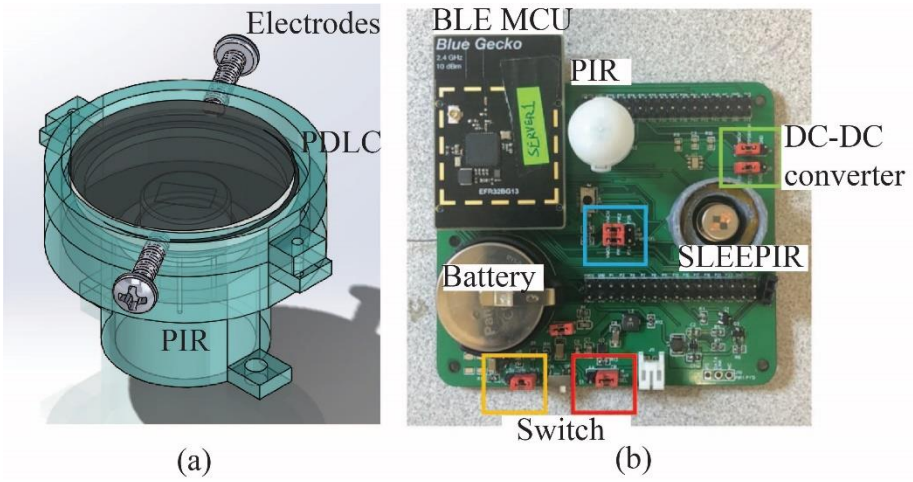

Figure 5.1 (a) The 3D illustration of a SLEEPIR module, and (b) the devised SLEEPIR sensor node.

The block diagram of the SLEEPIR sensor node is shown in Figure 5.2. The battery could be either a coin cell or 2 AA batteries. The battery will power the MCU, the DC-DC upconverter, the SLEEPIR module, and the PIR sensor. In this prototype, the output voltage from DC-DC upconverter is 10V, which is enough to make the PDLC shutter reaches the maximum MOD, as descripted in Chapter 4.2.1. The driving circuit will convert the PWM signal from the MCU to the AC voltage to drive the PDLC shutter. The MCU will also read the analog signals from both the SLEEPIR module and the PIR sensor.

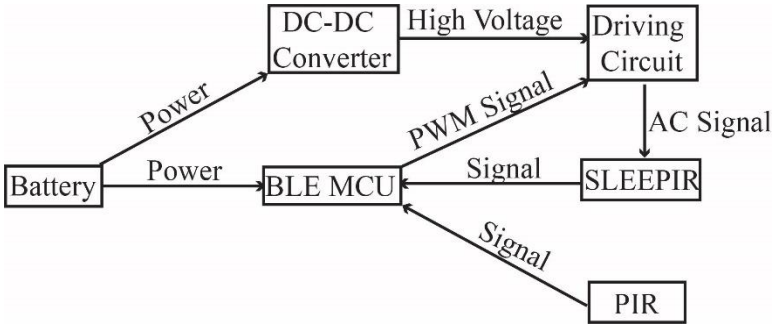

Figure 5.2 Block diagram of the SLEEPIR sensor node.

The operation pipeline of the SLEEPIR sensor node is shown in Figure 5.3. Normally, the MCU stays in the sleep mode to save energy while a timer is running to count the time of sleep. Once the timer reaches a certain value of measurement frequency, such as every 10 mins, or the motion PIR sensor is triggered, the MCU will wake up and start sending PWM signals to drive the PDLC shutter while collecting and transmitting data, which will last for 8 seconds. The collected data will be sent to the hub via a wireless

connection, Bluetooth, in this work. After the communication is complete, the node will go back to the sleep mode and wait for the next wake-up command.

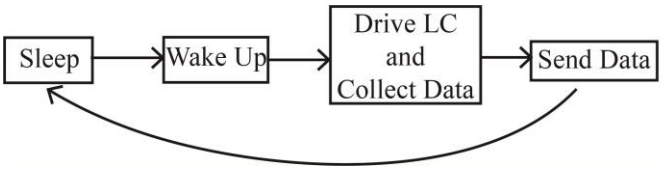

Figure 5.3 The operation pipeline of the SLEEPIR sensor node.

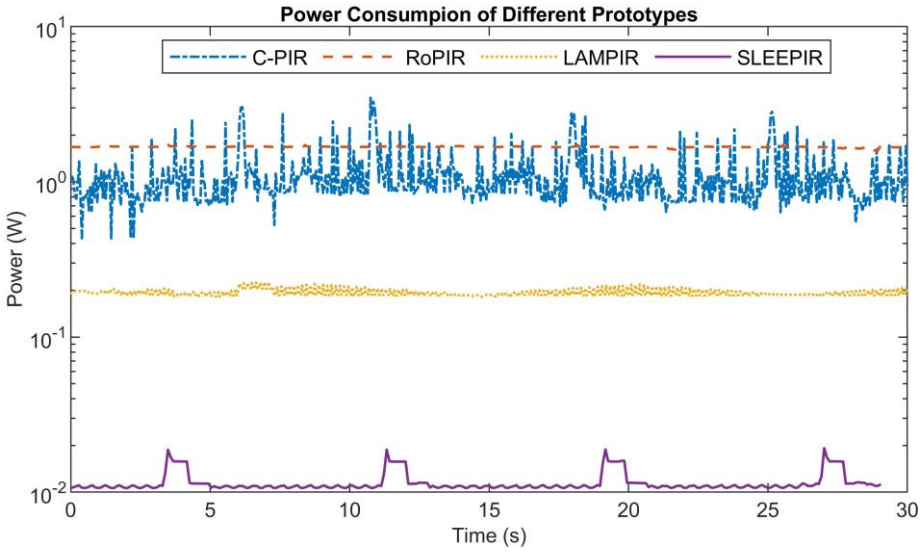

Figure 5.4 Power Consumption of SLEEPIR sensor node and previous prototypes.

The power consumption of the SLEEPIR sensor node, measured by a multimeter is compared with the mechanical shutter prototypes, the C-PIR, the Ro-PIR, and the LAMPIR developed by our group, as shown in Figure 5.4. The result shows that the

average power consumption of this SLEEPIR node is 10.9 mW, which is over 95% reduction compared to the previous prototypes.

5.2. Lab Test with SLEEPIR Sensor Nodes

A SLEEPIR sensor network consists of two SLEEPIR sensor nodes is tested in the lab environment, where the temperature is relatively stable. Each SLEEPIR sensor node has one SLEEPIR module and one traditional PIR sensor. The PDLC shutter on the SLEEPIR module is fabricated with the condition M80D22C1.

5.2.1. Test Overview

The tests are conducted in a room with two types of floor maps, as shown in Figure 5.5. We denote them Floorplan I and Floorplan II, respectively. Figure 5.5 (a) shows Floorplan I, which represents a great room of a single-family house with two functionalities, the left part is the living room (LR), and the right part is the dining room (DR). Figure 5.5 (b) shows Floorplan II, which represents a one-bedroom apartment with a bedroom (BR) and a dining room (DR). The difference between these two floorplans is that there is an additional wall separating two rooms in Floorplan II. The “wall” in this study is replaced by a white curtain for easy implementation, as shown in Figure 5.5 (c). We refer to the installed two sensor modules to be Node 1 and Node 2, respectively.

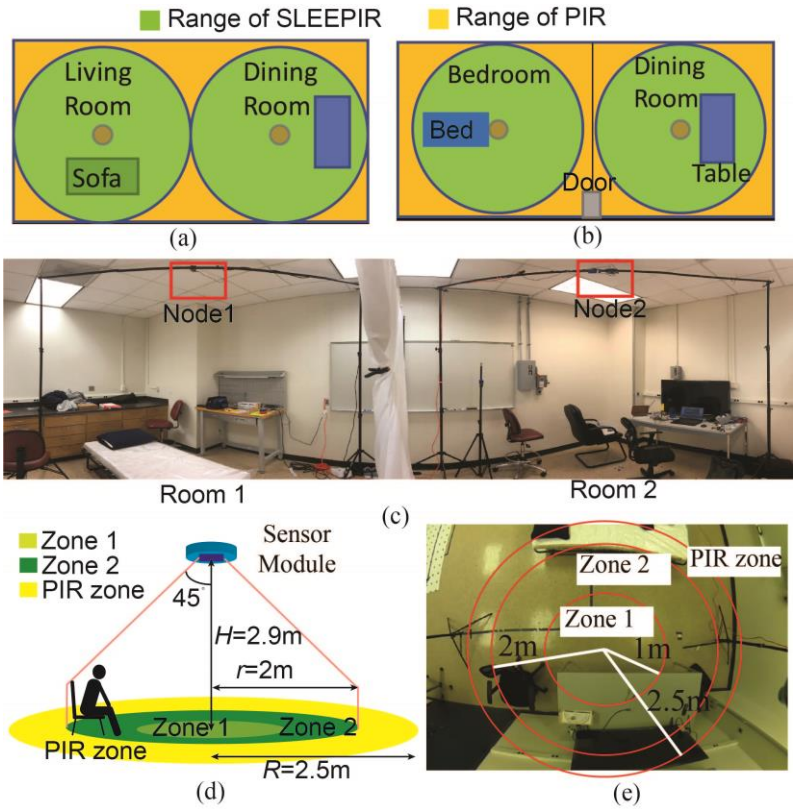

Figure 5.5 (a) Floorplan I (b) Floorplan II (c) The photograph of Floorplan II. (d) The diagram shows that the ceiling-mounted sensor node and the detection range. The detection area of the SLEEPIR is a circular area with a radius of 2 m. We segmented this area into two zones: zone 1 (circular area with 1m radius) and zone 2 (concentric circles). The detection area of the PIR sensor is a circular area with a radius of 2.5m. (e) The photograph of the test area. Reprinted with permission from [96].

The green round area is the detection range of the SLEEPIR sensor module, with a radius of 2m. The yellow area is the detection range of the PIR sensor. The photograph of Floorplan II is shown in Figure 5.5 (c). Two sensor nodes are placed on the two frames in each room's center with a height of 2.9m. For the SLEEPIR sensor module, the field of view is 90° × 90°. The traditional PIR sensor has a FOV of 103°×103°. Here, we assume

the upper body of a human has an average height of 0.9m while performing daily activities. This detection range applies to most standard office rooms, bedrooms, and dining rooms [136]. The covering area of SLEEPIR is segmented into two zones to investigate the zone-level-dependent occupancy, as shown in Figure 5.5 (d) and (e). Zone 1 is a circular area with a radius of 1m, while zone 2 is the remaining concentric circle area.

Three types of tests are conducted to include more complex occupancy scenarios: the action-based test, the continuous activity-based test, and the typical daily routine-based test.

Table 5.1 Typical daily actions. Reprinted with permission from [96].

Actions ID	Action name	Zone	Recorded Time (min)
1	Sitting	Zone1	5
2	Sitting	Zone2	5
3	Sitting, posture change	Zone1	5
4	Sitting, posture change	Zone2	5
5	Lying	Zone1	5
6	Lying	Zone2	5
7	Standing	Zone1	5
8	Standing	Zone2	5
9	Standing, posture change	Zone1	5
10	Standing, posture change	Zone2	5
11	Walking	-	5
Unoccupied	-	-	60

For the action-based test, 12 different actions are selected, as shown in Table 5.1. The first 11 actions are occupied, and the last one is unoccupied. Note that all the tests are done within the detection range of the SLEEPIR sensor node. For Action 1, 2, 5, 6, 7, and 8, the occupant remains almost stationary. For Action 3, 4, 9, and 10, the occupant would change postures not significantly while the main body remains at the same position, such as stretching arms and changing body postures. During the test, the occupant will repeat the same activities in both rooms. Note that the background infrared radiation of different rooms with different floorplans is different.

After collecting data from the action-based test, seven continuous activities are planned, as shown in Figure 5.6. We denote these activities in the alphabetic order, which are Activity A to G. Activity A to E are the activities conducted by only one occupant, while activities F and G are the activities of two occupants performing at different action sequences. In Figure 5.6, the arrows represent the routes of the occupants. The detailed descriptions of each activity are shown below:

Activity A: The occupant stays outside the living room for 5 minutes → sits on the sofa and watches TV for 5 minutes → walks to the dining room and cooking for 5 minutes → sits by the table for 5 minutes.

Activity B: The occupant sits in the dining room for 5 minutes → walks to the living room and sits on the sofa for 5 minutes → walks to the edge of the detection area and makes a phone call → goes back to the sofa and sits for 5 minutes → leaves the living room for 5 minutes.

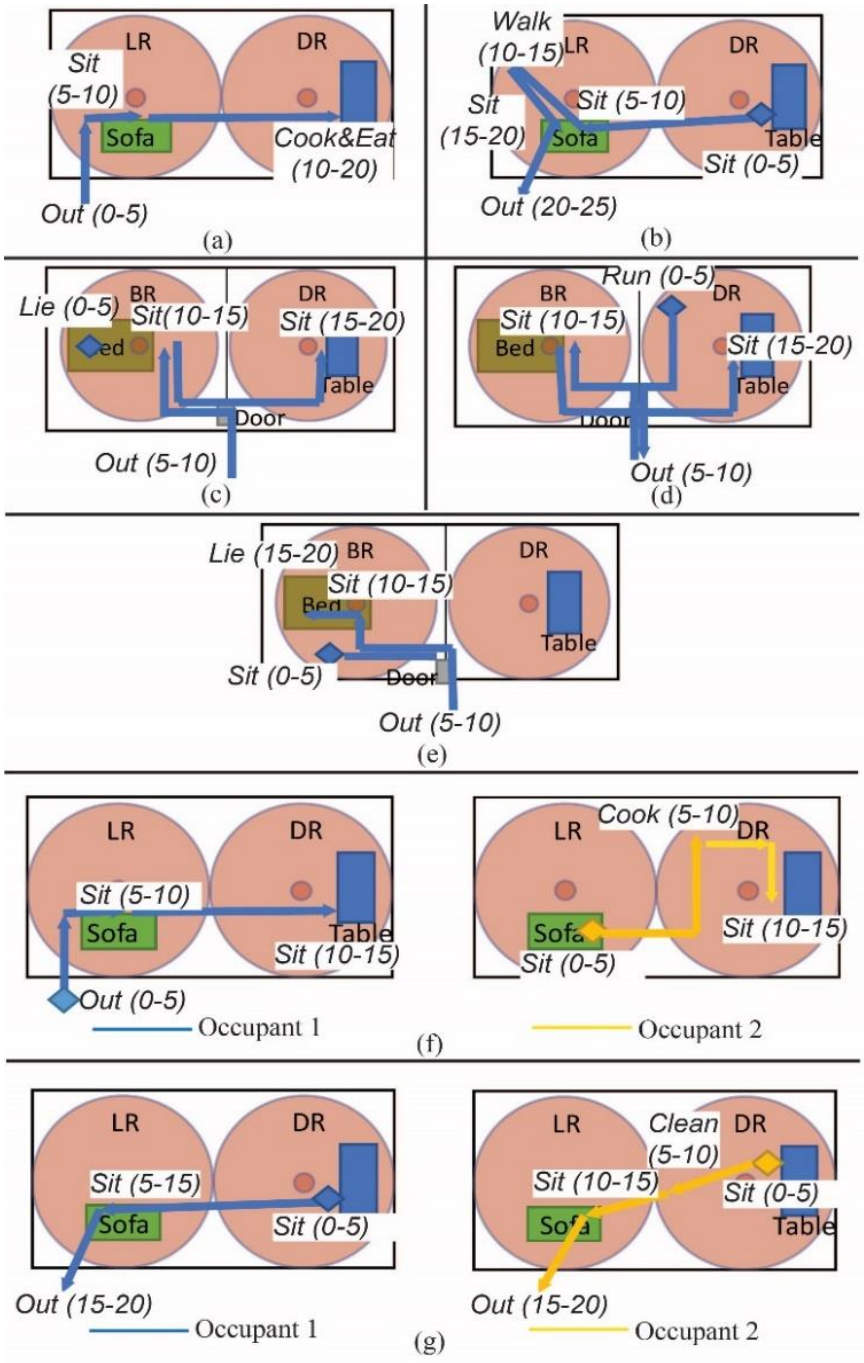

Figure 5.6 The continuous activity sequence for (a) Activity A, (b) Activity B, (c) Activity C, (d) Activity D, (e) Activity E, (f) Activity F, and (g) Activity G. Reprinted with permission from [96].

Activity C: The occupant lies on the bed in the bedroom for 5 minutes → leaves the room for personal care for 5 minutes → goes back to the bedroom for 5 minutes → walks to the dining room for 5 minutes.

Activity D: The occupant works out in the living room for 5 minutes → leaves the room for personal care for 5 minutes → goes to the bedroom for 5 minutes → walks to the living room and sits for 5 minutes.

Activity E: The occupant sits in the bedroom for 5 minutes → leaves the room for personal care for 5 minutes → goes back to the bedroom and sits on the bed for 5 minutes → lies on the bed for 5 minutes.

Activity F: Occupant 1 stays outside the living room for 5 minutes while occupant 2 sits on the sofa for 5 minutes. → Occupant 1 walks into the living room and sits on the sofa for 5 minutes, while occupant 2 goes to the dining room and cooks for 5 minutes. → Both occupants enter the dining room and sit for 5 minutes.

Activity G: Both occupants sit by the table in the dining room for 5 minutes. → Occupant 1 goes to the living room and sits on the sofa for 10 minutes, while occupant 2 cleans the dining room for 5 minutes and goes to the sofa for 5 minutes. → Both occupants leave the room for 5 minutes.

Also, note that Activity A, B, F, and G are performed in rooms with Floorplan I, while Activity C, D, and E are performed in rooms with Floorplan II. Figure 5.7 shows the signals from the SLEEPIR and PIR sensor and the PDLC shutters' state of each node when performing seven continuous activities. The green line, blue line, and red line

indicate the SLEEPIR and PIR sensor signal and the PDLC shutters' state of each node, respectively.

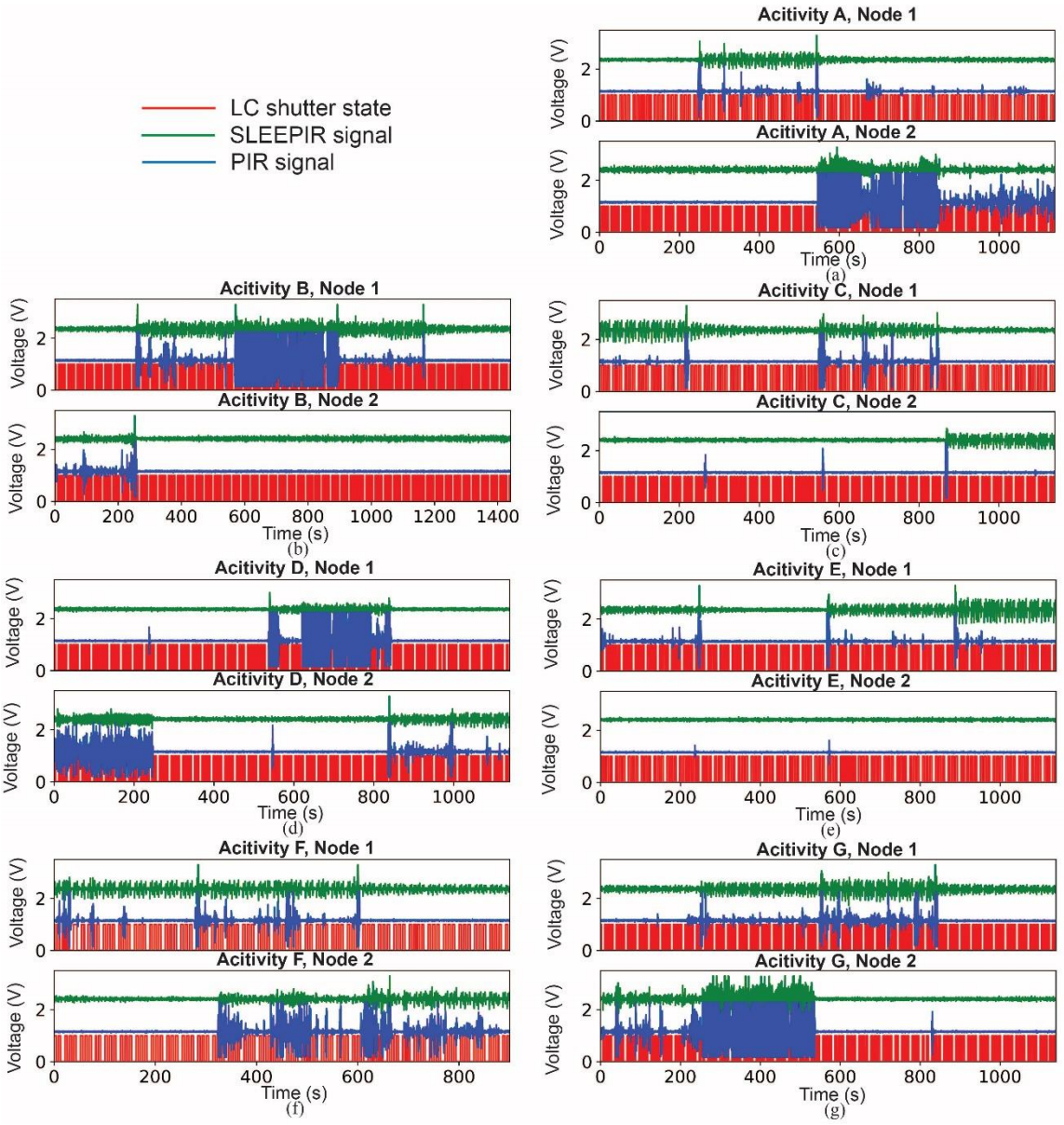

Figure 5.7 Signals from two sensor nodes for 7 different activities. (a) activity A, (b) activity B, (c) activity C, (d) activity D, (e) activity E, (f) activity F, and (g) activity G. Reprinted with permission from [96].

Next, we conduct experiments based on the typical daily routine that one occupant will perform for 24 hours. However, we scaled the test by a factor of 24 due to the limited time for the testing. It means that the duration of the test is 1 hour. In Table 5.2, column 1, column 3, and column 4 show the ideal time duration, the person's action, and the room the person would be in, respectively. The 2nd column shows the actual time duration when performing the test. One person conducts the test to simulate a full-time employee's typical daily routine on a regular weekday living in a one-bedroom apartment with Floorplan II. The original signal from both sensor nodes is shown in Figure 5.8.

Table 5.2 Typical daily routine of a full-time employee on a regular weekday. Reprinted with permission from [96].

Ideal Time	Test time (scaled by 24)	Action	Room
0:00-7:30	18.75min	Sleep	BR
7:30-8:00	1.25min	Personal care	-
8:00-8:30	1.25min	Cook + eat	DR
8:30-18:00	23.75min	Work	-
18:00-19:00	2.5min	Cook + eat + clean	DR
19:00-20:00	2.5min	Workout	-
20:00-22:00	5min	Rest	DR
22:00-22:30	1.25min	Personal care	-
23:00-0:00	2.75min	Sleep	BR

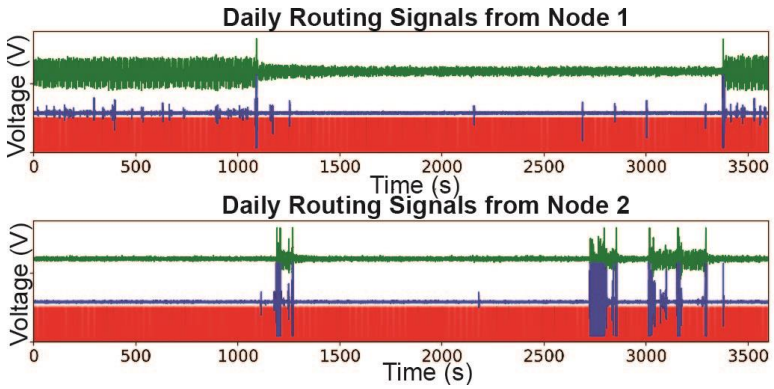

Figure 5.8 Raw signals from both Node 1 and Node 2 for the daily routine dataset. Reprinted with permission from [96].

5.2.2. Threshold Approach

There are three datasets collected from three sets of previous experiments. I denote them as the action-based dataset, the activity-based dataset, and the daily-routine-based dataset. The action-based dataset is used to extract the optimal threshold value we will use to evaluate the presence detection performance of the other two datasets. The threshold value method is commonly used for presence detection [16, 70, 71].

Firstly, I will determine the threshold value from the action-based dataset. When the PDLC shutter turns ON or OFF for stationary occupants, there will be peaks from the SLEEPIR sensor module while the PIR sensor shows a flat output [42]. According to Equation (3.5) and (3.6), the peak-to-peak value depends on the IR radiation received by the SLEEPIR sensor module. Thus, the peak-to-peak value in a period T, which is denoted as V_{pp} can be used to classify the occupied and unoccupied scenarios. For a moving occupant, the motion of the human body results in even higher V_{pp} values. We denote

these threshold values to be $V_{th,sleepir,node1}$, $V_{th,pir,node1}$, $V_{th,sleepir,node2}$, $V_{th,pir,node2}$, which represent the threshold values of the SLEEPIR sensor module and the PIR sensor of node 1 and node 2, respectively.

For the action-based dataset, the first 11 actions are occupied actions, while the last one is unoccupied action. For each action, I extract the V_{pp} values from both the SLEEPIR sensor module and the PIR sensor of both nodes for each period. For occupied actions, we concatenate all V_{pp} values into four arrays, $\boldsymbol{V}_{ppo,sleepir,node1}$, $\boldsymbol{V}_{ppo,pir,node1}$, $\boldsymbol{V}_{ppo,sleepir,node2}$, and $\boldsymbol{V}_{ppo,pir,node2}$. These four arrays represent the V_{pp} from the SLEEPIR and PIR of node 1 and node 2, respectively. Similarly, for the unoccupied action, we have $\boldsymbol{V}_{ppu,sleepir,node1}$, $\boldsymbol{V}_{ppu,pir,node1}$, $\boldsymbol{V}_{ppu,sleepir,node2}$, and $\boldsymbol{V}_{ppu,pir,node2}$. The letters "o" and "u" in the subscript represent the occupied and unoccupied actions, respectively.

To determine the optimal threshold value to classify the occupied and unoccupied scenarios, I first determine the threshold value for the PIR sensor. Due to the nature of motion detection, the threshold value can be known as

$$\begin{aligned} V_{th,pir,node1} &= \max\left(\boldsymbol{V}_{ppu,pir,node1}\right) \\ V_{th,pir,node2} &= \max\left(\boldsymbol{V}_{ppu,pir,node2}\right) \end{aligned} \tag{5.1}$$

To determine the threshold value for the SLEEPIR sensor of both nodes, I define the accuracy on a variable h to be:

$$\begin{aligned} &Acc_{node1}(h) \\ &= \frac{sum\left(\boldsymbol{V}_{ppo,sleepir,node1} \geq h\right) + sum\left(\boldsymbol{V}_{ppu,sleepir,node1} < h\right)}{size\left(\boldsymbol{V}_{ppo,sleepir,node1}\right) + size\left(\boldsymbol{V}_{ppu,sleepir,node1}\right)} \end{aligned} \tag{5.2}$$

$$Acc_{node2}(h)$$

$$= \frac{sum(\boldsymbol{V}_{ppo,sleepir,node2} \geq h) + sum(\boldsymbol{V}_{ppu,sleepir,node2} < h)}{size(\boldsymbol{V}_{ppo,sleepir,node2}) + size(\boldsymbol{V}_{ppu,sleepir,node2})} \quad (5.3)$$

where sum(·) calculates the number of the arguments to be true, and size(·) is the length of the array. Then the threshold value for the SLEEPIR sensor of both nodes can be derived from

$$V_{th,sleepir,node1} = \arg\max_{h} Acc_{node1}(h) \quad (5.4)$$
$$V_{th,sleepir,node2} = \arg\max_{h} Acc_{node2}(h)$$

Table 5.3 shows the optimal threshold value determined from the action-based dataset.

Table 5.3 Threshold values for the SLEEPIR and PIR of Node 1 and Node 2. Reprinted with permission from [96].

$\boldsymbol{V_{th,sleepir,node1}}$	$\boldsymbol{V_{th,pir,node1}}$	$\boldsymbol{V_{th,sleepir,node2}}$	$\boldsymbol{V_{th,pir,node2}}$
0.37V	0.37V	0.17V	0.16V

After extracting the corresponding peak-to-peak values for each period, I use the obtained threshold value from Table 5.3 to determine each activity's occupancy status and then calculate the accuracy. For the values of $V_{pp,sleepir,node(i)}$ and $V_{pp,pir,node(i)}$ from each period of node *i*, where *i* =1 or 2, the determined occupancy state is

$$State\left(V_{pp,sleepir,nodei}, V_{pp,pir,nodei}\right) = \begin{cases} 0, & if\ V_{pp,sleepir} < V_{th,sleepir,nodei}\ \ or\ V_{pp,pir} < V_{th,pir,nodei} \\ 1, & otherwise \end{cases} \quad (5.5)$$

Here, 0 and 1 indicate the unoccupied and occupied state, respectively. Based on Equation (5.5), the accuracies of the detection results are shown in Table 5.4.

Table 5.4 Accuracy for continuous activities and daily routine using fixed threshold values.

Activity	Node 1 Accuracy (%)	Node 2 Accuracy (%)
A	93.07	99.15
B	98.67	96.03
C	98.10	97.46
D	98.35	99.19
E	98.23	98.13
F	97.62	100.00
G	96.69	98.29
Daily Routine	94.93	93.75

5.2.3. Machine Learning Approach

From the previous result, the accuracy of using threshold values extracted from the action-based dataset and predicting on the other two datasets is not high. There are several reasons: (1) Different datasets are collected at different times. Also, the background and placement of furniture may be different. The threshold value extracted from a dataset is not suitable for another dataset. (2) When performing continuous activities, the occupant may change postures or perform actions with large amplitudes than instructed from time to time. For example, the occupant will perform actions when the PDLC shutter is turning

ON or OFF. If the radiation variation from the action and the variation from the PDLC change in the opposite directions, the V_{pp} will decrease. Thus, I explore machine learning models to improve the detection performance further [137].

The overall process of using the machine learning model is as followed. At first, I extract the statistical features from all three datasets. Then, I feed the training dataset to the machine learning models to train and evaluate each model. Finally, the trained models are used on the test dataset.

A total of 34 statistical features are extracted from both the SLEEPIR and the PIR sensing signals during each detection period of T, which is defined in Figure 3.1(b). They include 15 typical features [138] and two additional features from each node: the rising peak to peak value V_{ppr} and the falling peak to peak value V_{ppf}. Both additional features represent the peak-to-peak value that happens when the PDLC shutter switches from OFF to ON and from ON to OFF, respectively. According to Figure 4.10, SLEEPIR will generate polarity peaks for stationary objects. These are critical features distinguishing stationary occupants from the unoccupied environment. When the occupant is moving, there will also be various peaks. Thus, other features, such as peak numbers, signal power, peak-to-peak values, could help detect moving occupants. Note that the abbreviation of features extracted from the SLEEPIR and PIR sensor has subscripts of “s” and “p”, respectively. All features will be normalized in the range of (0,1) before fed to the machine learning models.

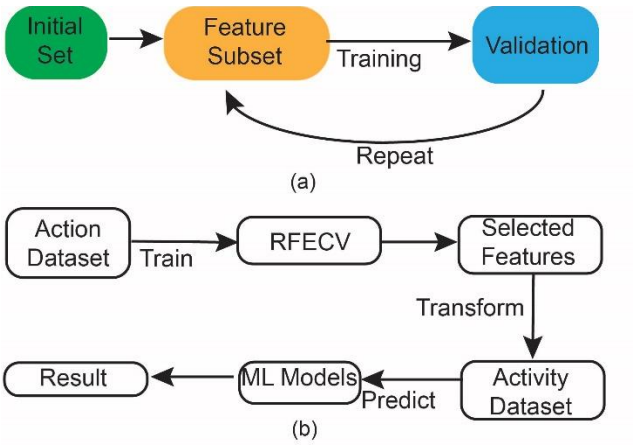

Figure 5.9 (a) The illustration of wrapper feature selection method. (b) The pipeline of feature selection using RFECV algorithm and predict the presence result on various machine learning models. © 2021 IEEE. Reprinted with permission from [137].

However, a large number of features will cause overfitting, which will decrease the accuracy of the test set, and increase the computation complexity. Thus, I use wrapper feature selection to choose key features and form an optimal feature subset, as shown in Figure 5.9(a). I employ recursive feature elimination with cross-validation (RFECV), one of the most popular implementation algorithms, to down select key features [139, 140]. As shown in Figure 5.9 (b), I utilize an open-source machine learning framework, scikit-learn [79], to perform such a down selection. At first, the 34 features extracted from the action-based dataset will be extracted and ranked by their importance for an estimator. The least important feature(s) will be removed. This process will be repeated iteratively until the maximum accuracy is reached (100%) on the action-based dataset. Thus, an optimal subset containing a minimum (eight) number of selected features will be generated: the minimum value of SLEEPIR (min_s), maximum value of SLEEPIR (max_s), standard

deviation of SLEEPIR (sd_s), cross variation of SLEEPIR (cv_s), peak to peak value of SLEEPIR (vpp_s), peak number of SLEEPIR (pks_s), rising peak to peak value of SLEEPIR ($vppr_s$), peak to peak value of PIR (vpp_p). Then, we form another subset from the activity-based dataset and daily routing dataset with the same eight selected key features.

Finally, these eight key features will be applied to six machine learning models, as shown in Figure 5.10. Random forest (RF) is an ensemble learner that constructs a forest of uncorrelated decision trees (week learners) [141]. The k-nearest neighbors (KNN) classifier categorizes new data to the class that is the most common among its k nearest neighbors [77]. Multiple layer perception (MLP) model is a neural network that consists of an input layer, hidden layer(s), and an output layer. The weights of the connections would be updated during backpropagation [142]. Support vector machine (SVM) is a discriminative classifier formally defined by separating hyperplanes [75, 76]. Given the training data, the algorithm gives optical hyperplanes which categorize new data. In Naïve Bayes (NB) classifier, the posterior probability is computed from all input data based on all classes. Then the new data is assigned to the class with the highest posterior probability [143]. Decision tree (DT) is a non-parametric supervised learning method to do classification and regression by making a series of decision rules from input data [78].

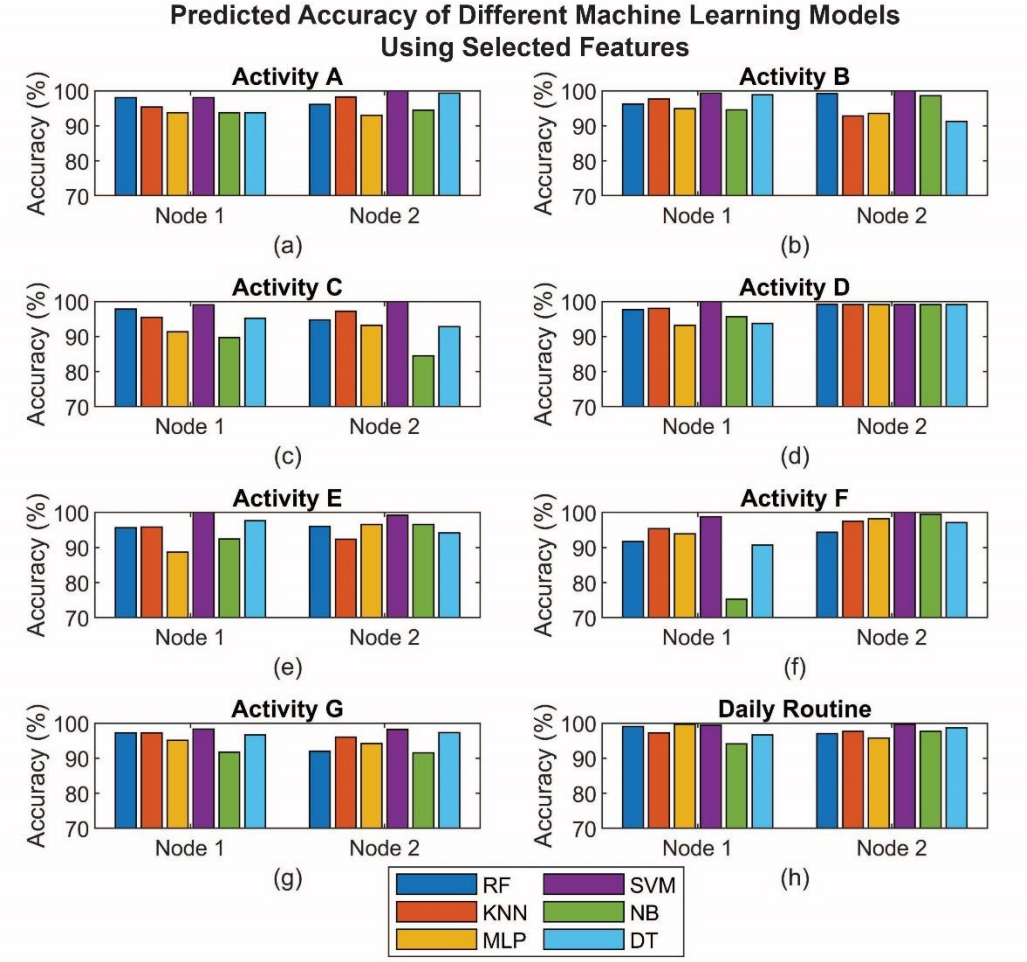

Figure 5.10 The predicted accuracy for presence detection using selected features with six multiple machine learning models for activity-based dataset and daily-routine-based dataset.

From Figure 5.10, we see that although these classifiers show similarly high accuracy over the action-based dataset, the predicted performance over the activity-based dataset is different. For example, the accuracy of Node 1 of activity A is lower than others. One reason is that the overlap detection area of the PIR sensors on both nodes. For example, in Figure 5.7, Activity A, the signal from the PIR sensor of node 1 shows five

peaks even though the person is not in the living room. However, when the person is moving in the dining room, since there is no wall between these two rooms of Floorplan I, the movement of the occupant will still be detected by the PIR sensor in the living room. Thus, in the detection result of Figure 5.11(A) for Activity A, the result of node 1 shows five “occupied” states at the same moment. Similarly, for Floorplan II, although there is a wall between the two rooms, the doorway is shared by the two rooms. When the occupant enters or leaves the doorway, both PIR sensors could still detect the occupant. The potential solutions to address this issue include increasing the segmentation of the PIR Fresnel lens and extracting statistical features from a longer period. Another reason is the noise of the PIR sensor. This can be solved by using a filter circuit or a high-resolution ADC.

Finally, SVM with the radial basis function kernel reports the highest weighted average accuracy for all seven activities and daily routine dataset, which is 99.11% for Node 1, and 99.66% for Node 2. They are 2.53% and 2.81% higher than the threshold approach. In addition, such a machine learning model does not require the system to foresee the data distribution. The predicted results for the activity-based dataset and the daily-routine dataset, as well as the ground truth, are shown in Figure 5.11. The improvement of the machine learning approach than the threshold approach is shown in Table 5.5.

Table 5.5 The result of the machine learning approach than threshold approach.

Dataset		Activity A	Activity B	Activity C	Activity D	Activity E	Activity F	Activity G	Daily Routine
Node 1 Accuracy (%)		98.02	99.33	99.04	100.00	99.11	98.81	98.35	99.44
Node 2 Accuracy (%)		100.00	100.00	99.15	99.19	100.00	100.00	99.15	99.72
Improvement than threshold method (%)	Node 1	4.95	0.66	0.95	1.65	0.89	1.19	1.66	4.51
	Node 2	0.85	3.97	1.69	0	1.87	0	0.86	5.97

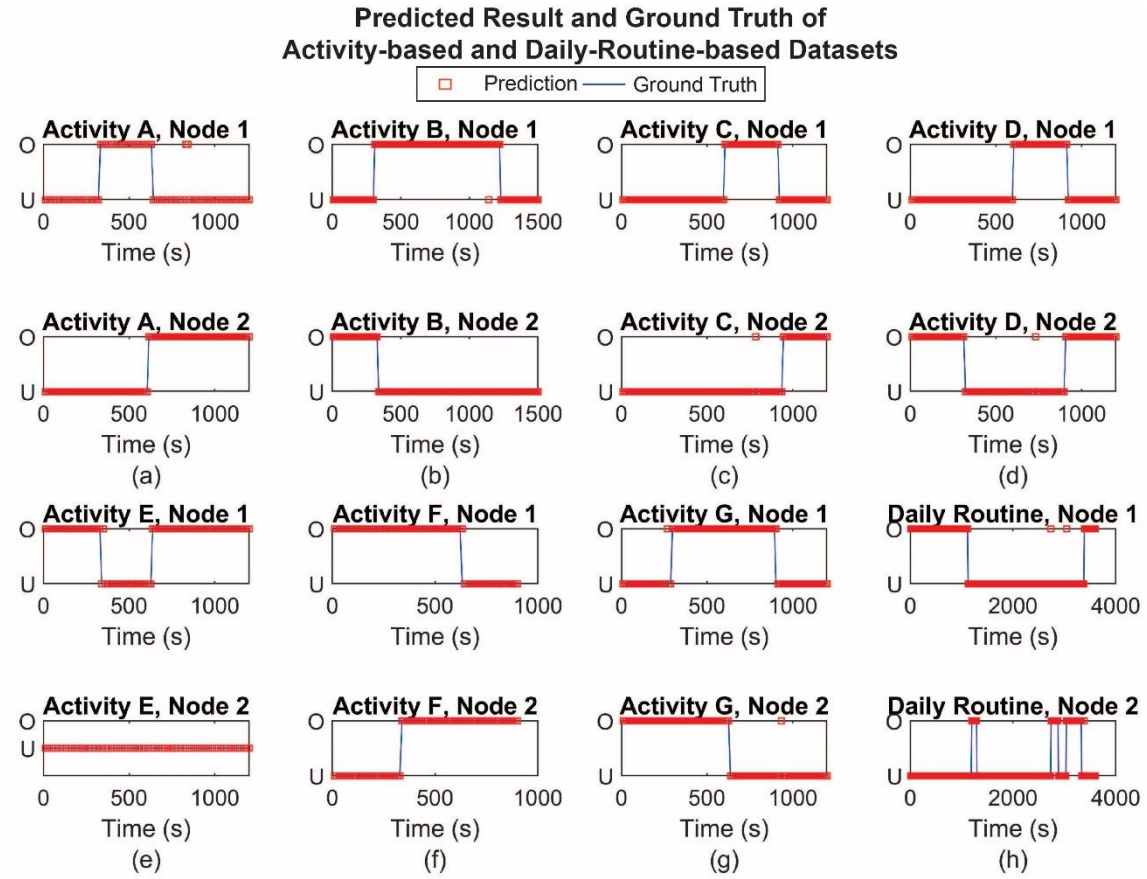

Figure 5.11 The ground truth and predicted results for (a-g) activity A to G and (h) daily-routine-based dataset. The machine learning model is based on the SVM model with the radial basis function kernel and with the selected key features (min_s, max_s, sd_s, cv_s, vpp_s, pks_s, $vppr_s$, and vpp_p).

5.3. Uncontrolled Test with the SLEEPIR Sensor Node

The occupancy detection experiments conducted in controlled environments have been discussed before. It means that the environment has a stable temperature. Also, the person under the test is following the predefined routine to perform different activities. However, these tests may not be suitable for practical application. For example, the indoor room temperature of residential houses that is comfortable for residents varies from 22°C to 26°C [144-146], depends on the location, natural light, clothes, ventilation, etc. In this varying environment, the temperature of the sensor itself, the surface of the floor, the human skin, and the furniture will also change. In this subsection, we study the impact of the temperature of the sensor node and the floor surface on the detection performance of the SLEEPIR sensor node.

5.3.1. Thermal Model of the SLEEPIR Sensor Node

Firstly, the thermal model of the sensor node is developed. A simplified model is shown in Figure 5.12. The SLEEPIR sensor node is placed on the ceiling. Its surface temperature, area and emissivity are T_s, A_s, ε_s, respectively. The floor in the field of view is shown in the circle. The surface temperature, area, and emissivity are T_f, A_f and ε_f, respectively. The air in the room is T_a. Since the sensor node has a small heat capacity, it will reach thermal equilibrium with the air fast. Thus, normally, $T_f = T_a$. The temperature of floor usually is different from the air temperature because of the heat conduction with the ground and ventilation with the air [147, 148].

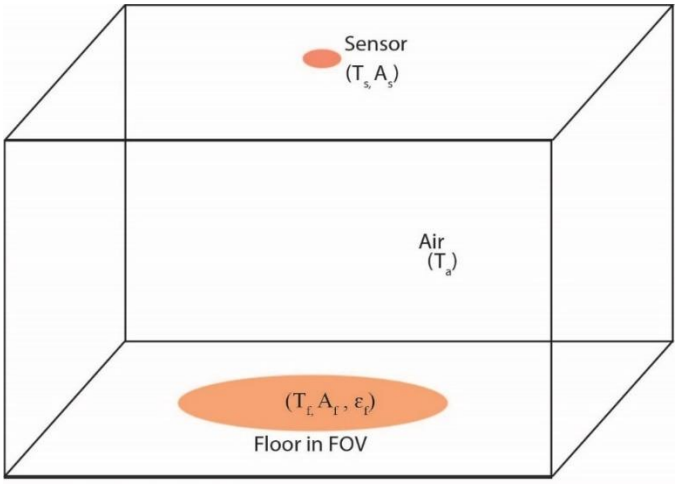

Figure 5.12 The thermal model of the SLEEPIR sensor node placed on the ceiling.

Since there is a temperature difference between the floor surface in the FOV and the sensor node, a radiation flux will transfer between the floor and the sensor. When there are no other objects within the field of view, the net radiation flux from the floor to the SLEEPIR sensor node is [106]

$$W_s = A_f F_{f\to s} \varepsilon_f \varepsilon_s \sigma (T_f^4 - T_s^4) \tag{5.6}$$

where $F_{f\to s}$ is the view factor from the floor to the sensor; σ is the Stefan-Boltzmann constant. Note that, when $T_f > T_s$, the direction of the net heat flux is from the floor to the sensor, which means the SLEEPIR sensor node will receive radiation. When $T_f < T_s$, the direction of the net heat flux is from the sensor to the flow, which means the SLEEPIR will emit radiation.

From the model built in Chapter 3.2, the peak-peak value V_{pp} of the SLEEPIR module is proportional to the incident radiation on the sensor. Thus, we have

$$V_{pp} \propto T_f^4 - T_s^4 \tag{5.7}$$

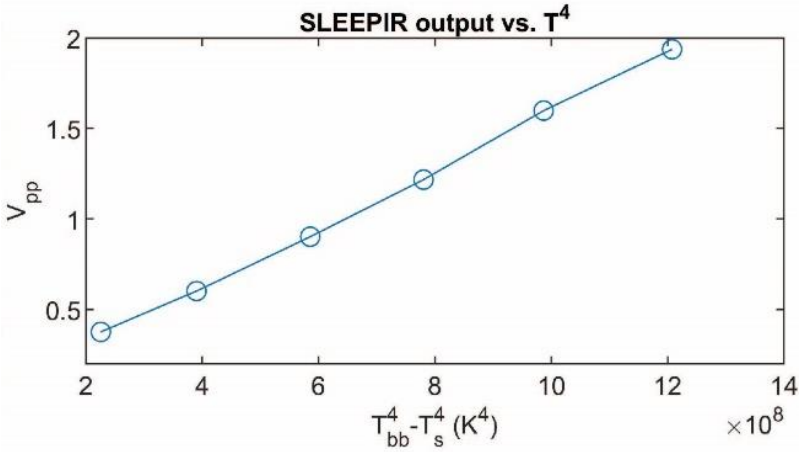

Figure 5.13 The output of the SLEEPIR module with T_{bb}^4-T_s^4. T_{bb} and T_s is the temperature of the blackbody source and SLEEPIR module, respectively.

I design an experiment with the same setup shown in Figure 4.11 to verify the thermal model described by Equation (5.7). The SLEEPIR sensor node is placed in front of a blackbody radiation source. The distance between the sensor and the blackbody is around 1 cm to make sure the blackbody's surface covers the FOV of the SLEEPIR module. The temperature of the sensor T_s is measured by a temperature sensor (Si7021, Silicon Labs). The surface temperature of the blackbody radiation source T_{bb} will change to different values.

T_{bb} is changed with six different values. I plot the relationship between the measured output V_{pp} with $T_{bb}^4 - T_s^4$. The result is shown in Figure 5.13. Good linearity is

found between V_{pp} with $T_{bb}^4 - T_s^4$. Thus, this result verifies the thermal model described by Equations (5.6) and (5.7).

5.3.2. Setup of Uncontrolled Test

Next, I conduct the experiment in an uncontrolled environment. There are two separate tests, the cooling stage test and the uncontrolled presence test. The experiment setup is shown in Figure 5.14. The sensor node is placed on a pole with a height of 2.7 meters. The surface temperature is measured by thermocouples and collected by a data acquisition device (DAQ, National Instrument) at a sampling frequency of 20Hz. A portable air conditioner unit is placed in the room.

Figure 5.14 Experiment setup of the uncontrolled test.

For the cooling stage test, the air conditioner unit is turned on to heat the room temperature to around 28°C. Then the room is naturally cooled down with no occupants inside. The purpose of this test is to find the relationship between the measured V_{pp} values of the SLEEPIR sensor module and the temperature difference $T_{bb}^4 - T_s^4$. The output of the SLEEPIR sensor module, sensor temperature T_s and floor temperature T_f are shown in Figure 5.15. The experiments last 167 minutes, which represents 335 periods of the SLEEPIR sensor module. The result shows that the amplitude of the SLEEPIR sensor module's output decreases when the difference between T_s and T_f decreases.

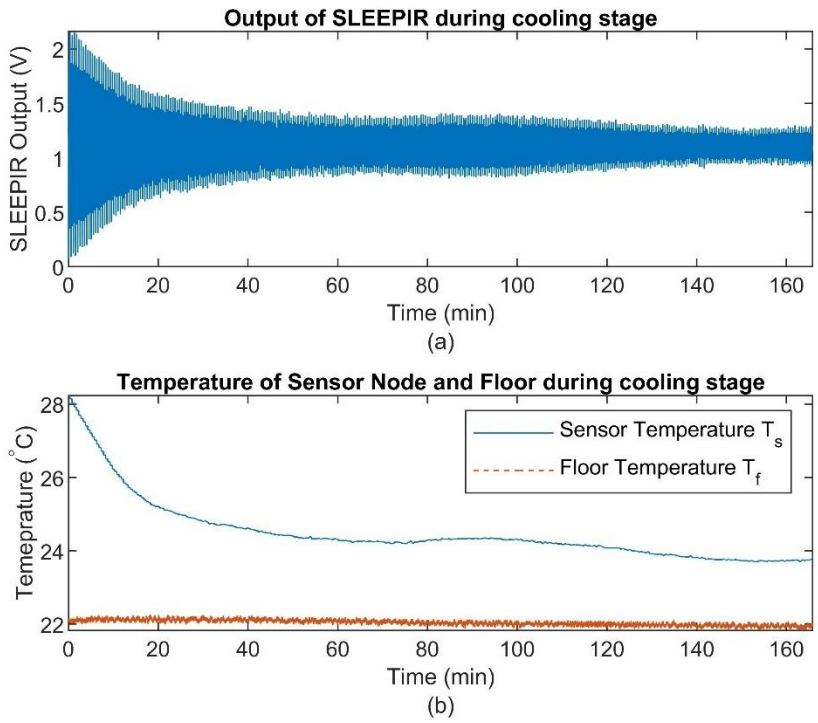

Figure 5.15 (a) The output of the SLEEPIR module during the cooling stage. (b) The temperature of the sensor node T_s and floor surface T_f during the cooling stage.

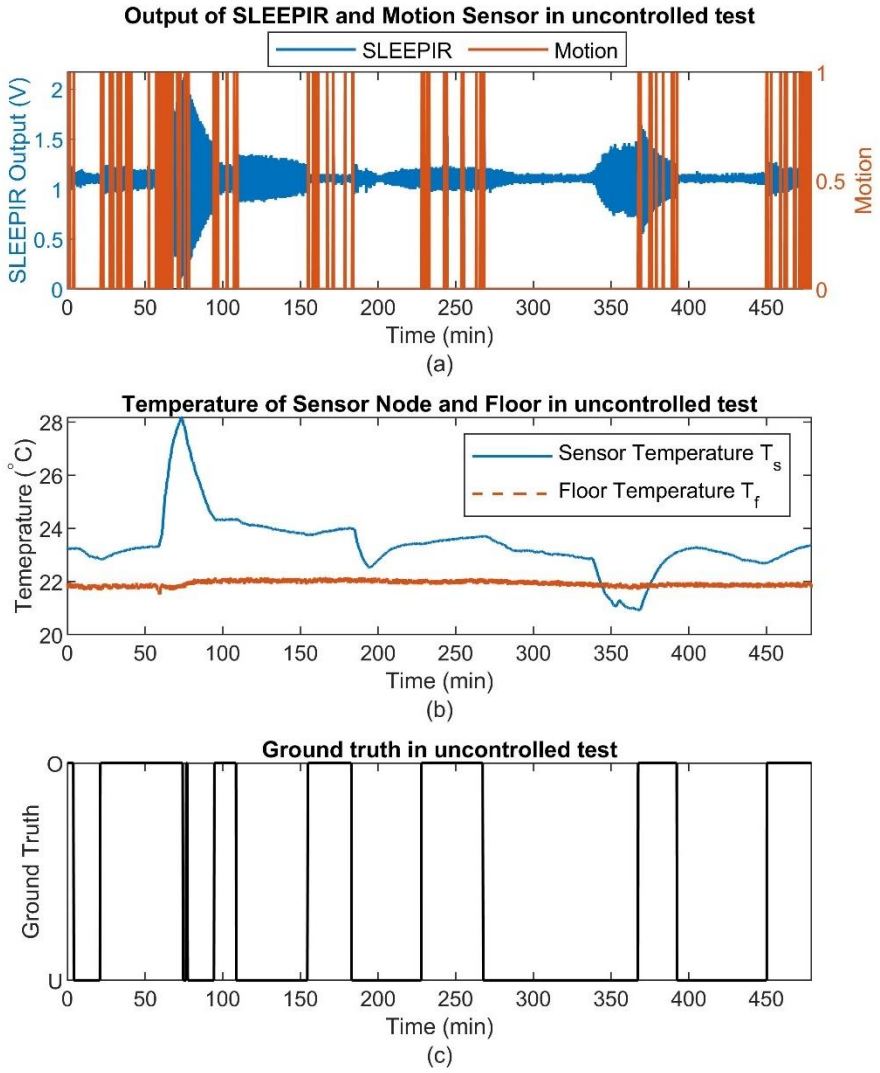

Figure 5.16 (a) The output of the SLEEPIR sensor module and the PIR sensor in the uncontrolled presence test. (b) The temperature of the sensor node T_s and floor surface T_f in the uncontrolled presence test. (c) Ground truth that is recorded manually. "O" and "U" represent the occupied and unoccupied states, respectively.

The second test is the uncontrolled presence test. One occupant goes in and out in an uncontrolled manner. The ground truth is recorded manually. The room temperature is controlled by the air conditioner unit. Besides the SLEEPIR sensor module, a traditional

digital PIR sensor will also output a positive detection result once it is triggered by the motion. The test lasts for around 8 hours, which is 956 periods of the SLEEPIR sensor module. The original data and the ground truth of the uncontrolled presence test are shown in Figure 5.16.

5.3.3. Adaptive Detection Algorithm

Next, I develop the adaptive detection algorithm for uncontrolled presence detection. Firstly, the relationship between the measured V_{pp} and $T_f^4 - T_s^4$ is found. The V_{pp} values are extracted for each period of the SLEEPIR sensor module during the cooling stage test. The scattering plot is shown in Figure 5.17. We fit V_{pp} and $T_f^4 - T_s^4$ linearly. The R^2 value of the linear fitting is 0.987. We denote the linear function of this fitting to be $P_{fit}(T_f, T_s)$, where the input arguments are T_f and T_s. The linear fitting could be written as

$$P_{fit}(T_f, T_s) = 3.738 \times 10^{-9}(T_f^4 - T_s^4) + 0.38V \tag{5.8}$$

We also define another variable δV with

$$\delta V = \max\left|P_{fit}(T_f, T_s) - V_{pp}\right| = 0.165V \tag{5.9}$$

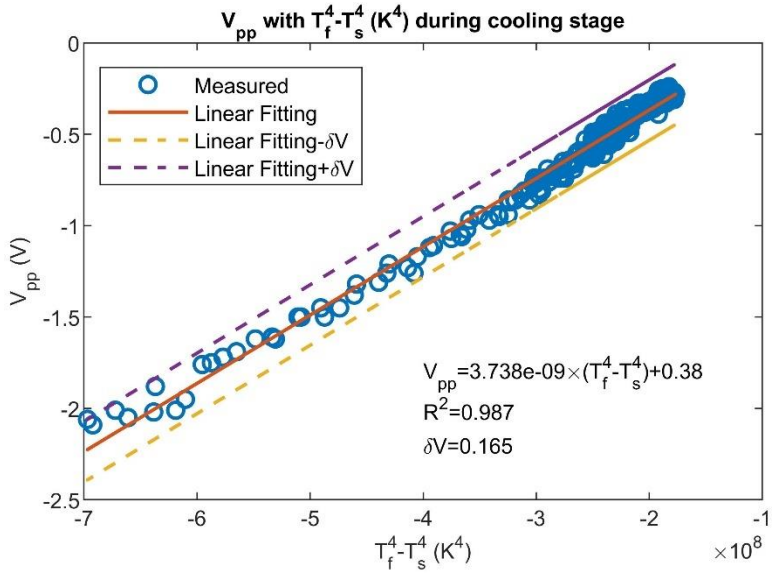

Figure 5.17 Blue dots are the measured V_{pp} and T_f^4-T_s^4. Red curve is the linear fitting. Yellow and purple curves are linear fitting with a margin of δV.

By definition, the δV indicates the margin between all the measured V_{pp} values and the linear fitting $P_{fit}(T_f, T_s)$. The yellow and purple curves in Figure 5.17 are the linear fitting with a margin $\pm\delta V$, which are $P_{fit}(T_f, T_s) - \delta V$ and $P_{fit}(T_f, T_s) + \delta V$, respectively. All the measured V_{pp} values are within the area covered by these two lines.

After getting the linear function $P_{fit}(T_f, T_s)$ and the margin δV, the adaptive detection algorithm is developed, as shown in Figure 5.18. For each period in the uncontrolled presence test, four values will be extracted: the sensor temperature T_s, the floor temperature T_f, the peak-to-peak value V_{pp} from the SLEEPIR sensor module and the result of the motion sensor *motion*. The input of the adaptive detection algorithm is

T_s, T_f, V_{pp}, *motion*, $P_{fit}(T_f, T_s)$, and δV. The adaptive peak-to-peak value $V_{pp,ada}$ is calculated as

$$V_{pp,ada} = V_{pp} - P_{fit}(T_f, T_s) \tag{5.10}$$

Then, the occupancy state of this period could be derived from the adaptive detection algorithm shown in Figure 5.18.

Algorithm: Adaptive Detection Algorithm

INPUT: T_s, T_f, V_{pp}, *motion*, P_{fit}, δV
OUTPUT: *State*

$V_{pp,ada} = V_{pp} - P_{fit}(T_s, T_f)$
if $|V_{pp,ada}| > \delta V$:
    State = 1
else if *motion* = 1:
    State = 1
else:
    State = 0

Figure 5.18 The adaptive detection algorithm.

5.3.4. Presence Detection Result

After applying the adaptive detection algorithm, the corresponding measured V_{pp}, adaptive $V_{pp,ada}$ are shown in Figure 5.19. When the occupant is within the detection area, $V_{pp,ada}$ will exceed the margin $\pm\delta V$ defined by the yellow and purple dotted curves, which represent the level of δV and $-\delta V$, respectively.

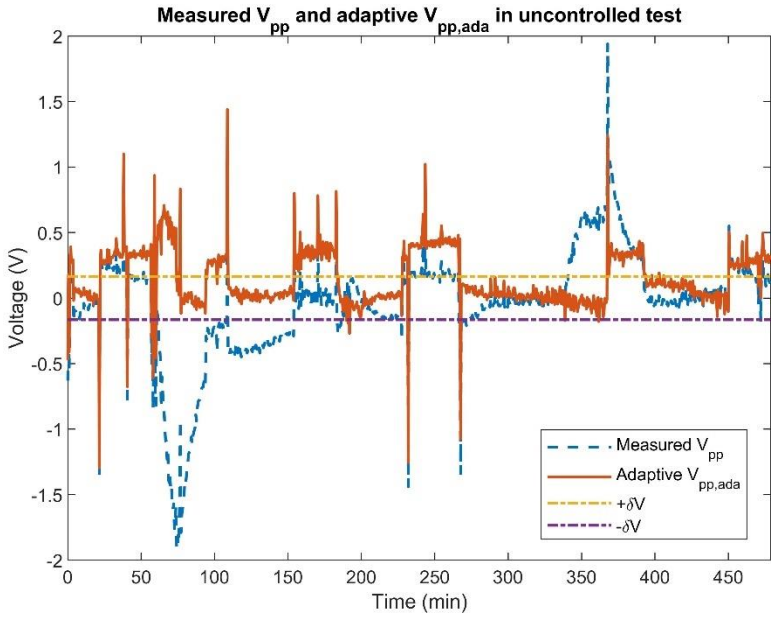

Figure 5.19 The measured V_{pp} and adaptive $V_{pp,ada}$ for the uncontrolled test.

Then, I compare the result of the adaptive detection algorithm with two other methods: using a stand-alone PIR sensor and using the SLEEPIR sensor module with a fixed threshold.

The first method that uses a stand-alone PIR sensor depends on the detection result of the PIR sensor solely, which is widely used in indoor light control [34, 149, 150]. The second method that uses a fixed threshold is also used by some publications with analog PIR sensors to detect occupancy [51]. It follows the detection method

$$State = \begin{cases} 1, & \text{if } V_{pp} > threshold \\ 0, & \text{otherwise} \end{cases} \quad (5.11)$$

The threshold value for this experiment is determined by the first 1 hour of the uncontrolled experiment test, which is 0.25V.

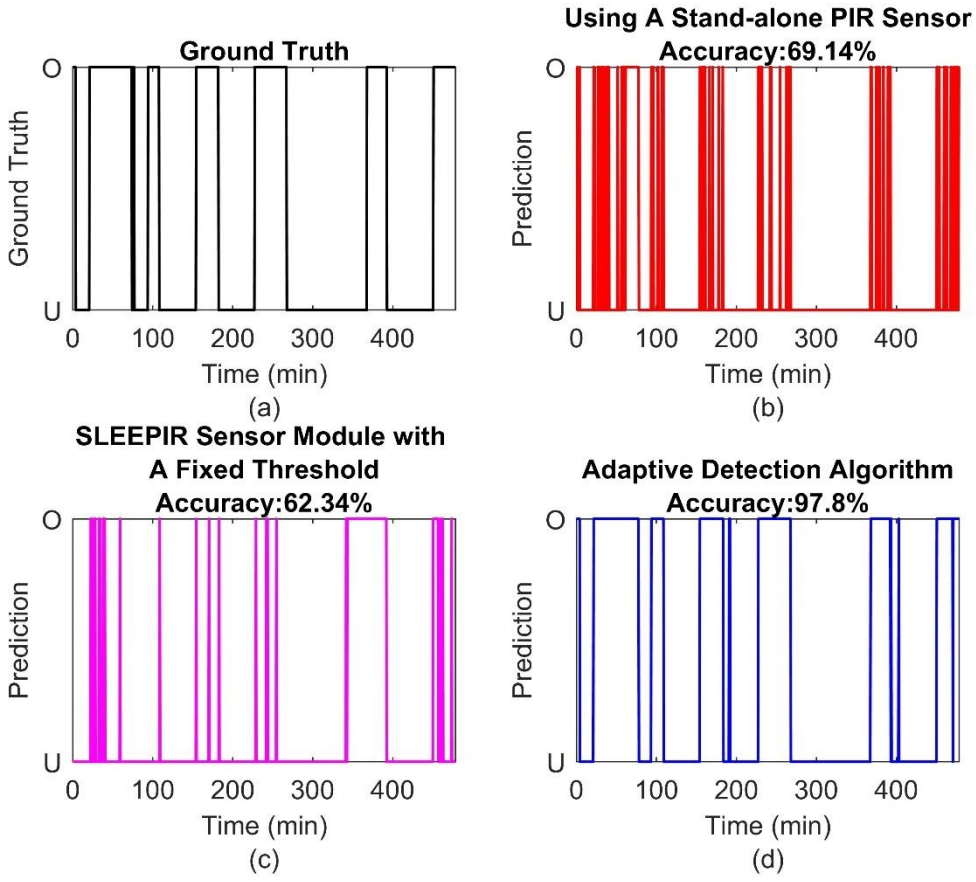

Figure 5.20 (a) The ground truth of the uncontrolled presence test. (b) The prediction results with the method that uses the stand-alone PIR sensor. (c) The prediction results with the method that uses the SLEEPIR sensor module with a fixed threshold. (d) The prediction results with the adaptive detection algorithm.

The prediction result of these three methods are shown in Figure 5.20 (b) (c) and (d), respectively. We could see that the adaptive detection algorithm is much better than

the other two methods. The errors in the result are mainly triggered by the motion sensor. The reason is that the air from the air conditioner unit will make the pole vibrate and cause false-positive detections for the motion sensor. We expect that if we place the sensor far away from the air conditioner outlet, the detection result will improve.

5.3.5. Comparison with Commercial Products

There are a lot of presence detection products on the market. Ecobee is a company that sells smart thermostats and occupancy sensors. The sensor nodes consist of a traditional motion sensor. Each node will send signals to the thermostat once triggered by a motion. From a publication that uses the data collected from Ecobee users, the authors analyzed the data from over 100 thermostats for over a year [151]. In total, there are over 73,000 measurements. However, the accuracy is 85% even it applies a machine learning approach. The reason is that the motion sensor will cause false-negative results when the occupants are not moving.

In this subsection, we introduce a concept called Annual Failure Rate (AFR) to evaluate the performance of our proposed SLEEPIR presence detection system and those in the reference. AFR is a common concept to evaluate the reliability of a device or a component [152, 153]. For a presence detection system, the total measurement number is N_y per year. The detection accuracy is p_T. The AFR in this work is defined to be the minimal number of the failure detection number K, which makes the probability of no more than K failed detections every year to be at least 95%. Mathematically, the probability of no more than K failures per year is

$$P(K) = \sum_{n=0}^{K} \binom{N_y}{n} p_T^{N_y - n} (1 - p_T)^n \tag{5.12}$$

AFR is the minimal value of K that makes $P(K) \geq 0.95$.

I compare the AFR of our proposed detection system and other approaches, such as using a stand-alone PIR sensor, using the SLEEPIR module with a fixed threshold, and the Ecobee products [151]. When calculating AFR, the total number of measurement per year $N_y = 17520$, so that the detection system could report the presence state every 30 minutes. The comparison is shown in Table 5.6. Compared to the Ecobee work, the adaptive detection algorithm run on the SLEEPIR sensor node reduces the AFR by 85%.

Table 5.6 Comparison of AFR between different presence detection approaches.

Presence Detection System	Data Size	Accuracy	AFR
Ecobee [151]	73000	85%	2628
Stand-alone PIR sensor	956	69.14%	5407
SLEEPIR with Fixed Threshold	956	62.34%	6598
Adaptive Detection Algorithm	956	97.80%	385

5.4. Discussion and Summary

In this chapter, the sensor node is designed with a SLEEPIR module, a traditional motion sensor, a wireless microcontroller, and DC-to-DC converters. The sensor node will periodically wake up to drive the PDLC shutter and collect data to reduce the power

consumption. The power consumption of the SLEEPIR sensor node is 10.9mW, which is a 95% reduction compared to previous mechanical shutter approaches.

Next, two types of presence detection experiments are conducted. The first one is the lab test. During the test, the environment temperature is unchanged, and the occupants follow the predefined activities to perform the experiment. A sensor network consists of two sensor nodes are placed in two floorplans. Three types of data are collected to evaluate the detection performance of the constructed sensor network: action-based dataset, continuous activity-based dataset, and daily routine-based dataset. The fixed threshold approach shows low accuracy since the background radiation may change when collecting different datasets. To improve the detection accuracy, we introduce the machine learning approach. Specifically, we use the RFECV algorithm to select optimal feature subsets to reduce overfitting and computing complexity. We use the action-based dataset to select features, train the machine learning models, then predict the accuracy of the realistic activity-based dataset. With a selected optimal subset, the SVM classifier reports the average accuracy for the activity-based dataset and the daily-routine dataset to be 99.11% for Node 1, and 99.66% for Node 2, which is 2.53% and 2.81% higher than the fixed threshold approach.

The second type of test is the uncontrolled test, where the room temperature and the occupant's behavior are uncontrolled. A thermal model is built for the sensor node, which indicates that the peak-peak value V_{pp} of the SLEEPIR sensor module is proportional to $T_f^4 - T_s^4$, where T_f and T_s are the the absolute temperatures of the floor and the sensor, respectively. The linear fitting between V_{pp} and $T_f^4 - T_s^4$ is found when

the room temperature changes. An adaptive detection algorithm is proposed to calibrate the measured V_{pp}. The adaptive detection algorithm shows an accuracy of 97.8%, which is 28.66% and 35.46% higher than the method using a digital PIR sensor and the method using the SLEEPIR sensor module with a fixed threshold, respectively.

Finally, we compare the result of the uncontrolled test with a commercial product, Ecobee. By introducing the concept AFR, the proposed adaptive detection algorithm shows an 85% reduction in AFR compared to Ecobee.

Some future works could improve the performance of the result of the presence detection test. (1) Apply machine learning to the uncontrolled test as well. The temperature of the sensor and the floor surface could be added to the inputs. Then, we could apply a similar process as we do on the controlled test, such as feature selection. (2) Instead of feature selection, feed the original signal of the SLEEPIR module to a deep learning model. This could help observe more information within the signal than statistical features. (3) Improve the thermal model by considering a more complex setup. The reason is that the furniture has different surface temperatures, emissivity, and shapes. By collecting the temperature of the furniture, the thermal model could be more accurate.

6. SUMMARY

This dissertation presents a SLEEPIR sensor module that consists of a PDLC infrared shutter, a PIR sensor, and a driving circuit. Commercial PIR sensors are widely used for automation, intrusion detection, and lighting control. However, PIR sensors only respond to the motion. Adding an infrared shutter that actively changes the transmitted radiation will enable the PIR sensor to detect stationary occupants. PDLC infrared shutters are chosen due to the high modulation, low cost, low power consumption, and simple fabrication process. A SLEEPIR sensor node is made of a SLEEPIR module, a traditional PIR sensor, a microcontroller, batteries, and DC-to-DC converters.

Three topics are studied in this dissertation: (1) the impact of different factors on the performance of the PDLC shutters, (2) the relationship between the SLEEPIR sensor modules' output and the properties of the PDLC infrared shutters, (3) the performance of presence detection using the SLEEPIR sensor nodes for different environmental factors.

6.1. Contribution

Chapter 2 introduces the working principle of the PIR sensor, the result of mechanical shutters, and the comparison between different LWIR LC shutters. The output of the analog PIR sensor is related to the sinusoidally modulated radiation. Mechanical shutters could be used as optical shutters that change the incident radiation of the PIR sensors. Our previously developed prototypes, including the chopped PIR sensor (C-PIR) [51], the rotational chopped PIR sensor (Ro-PIR) [43], and the Lavet motor-driven PIR sensor (LAMPIR) [44] are briefly introduced and show high accuracy for presence

detection, positioning, and tracking. However, they have several disadvantages, such as high power consumption, large size, large noise, and low reliability, which limit their practical applications. The PDLC infrared shutters are chosen as the focus of this dissertation due to their high modulation, low cost, and a simple preparation process. Compared to the reference [67, 68], we improve the contrast ratio and transmission difference of PDLC shutters by 16% and 165%, respectively.

Chapter 3 presents the design and characteristics of a SLEEPIR sensor module. I develop a model of the SLEEPIR sensor module's output, which is related to three factors, the effective modulation, the response time of the PDLC shutter, and the time constants of the PIR sensor. To measure the time constants of the PIR sensor, we design an experiment with a blackbody radiation source, a mechanical chopper, and a controller. The frequency response of the PIR sensor is measured and used to calculate the time constants. Finally, the measurement methods of the effective modulation MOD and the response time are introduced. By introducing the hysteresis, the persistence and the memory effect, the effective modulation MOD is defined to be the difference of the transmitted radiation between the ON and the OFF state. The two types of the response time, the rise time τ_r and the decay time τ_d, are measured by an infrared photodetector.

Chapter 4 presents the impact of the PDLC shutter's fabrication condition and driving condition on the effective modulation, the response time, and the output of the SLEEPIR module. From the microscope images of glass based PDLC shutters, we found that the droplet size will increase when the cooling rate decreases and when the mass ratio increases. Next, we study the impact of the driving and fabrication conditions on the

effective modulation of the PDLC shutters. The MOD will increase with larger voltage amplitude until reaching saturation level. The optimal driving frequency is found to be below than 980Hz. The optimal fabrication condition that maximizes the effective modulation is $\eta = 0.8$, $d = 22\mu m$, cool at 1 or 1.25°C/min. Moreover, cycling could help to reduce the persistence effect and memory effects. In the study of the response time, the result shows that rise time will decrease with the increasing voltage amplitude, while the decay time τ_d does not change much. We also study the impact of the fabrication condition on the response time. The result shows that the response time will increase with a larger cell gap d and a larger mass ratio η. Fourthly, the model of the SLEEPIR sensor module is verified by the good linearity between V_{pp} and ΔA_V, which are measured from PDLC shutters under difference fabrication conditions. Meanwhile, the optimal fabrication condition that generates the highest voltage amplitude is $\eta = 0.8$, $d = 22\mu m$, CR=1 or 1.25 °C/min. Finally, the lifetime of the PDLC shutters is discussed. The result shows that the output of the SLEEPIR sensor module is stable after 250,000cycles, which represents five years of usage if the measurement period is 10 minutes.

Chapter 5 presents the application of the SLEEPIR sensor nodes on presence detection experiments. The sensor node reduces the power consumption by 95% compared to the mechanical shutter prototypes. For the lab tests conducted by a sensor network in a controlled environment, the machine learning approach shows high detection accuracies, which are 99.11% for Node 1, and 99.66% for Node 2. They are 2.53% and 2.81% higher than the fixed threshold approach. For the uncontrolled test, the measured V_{pp} of the SLEEPIR module is proportional to the temperature difference between the floor and the

sensor. An adaptive detection algorithm that adaptively calibrates the measured V_{pp} shows an accuracy of 97.8% on the uncontrolled test, which is 28.66% and 35.46% higher than the method using a digital PIR sensor and the method using the SLEEPIR sensor module with a fixed threshold, respectively.

In summary, the PDLC infrared shutter is studied systematically. The optimal fabrication condition is found to maximize the output of the SLEEPIR sensor module. The proposed SLEEPIR sensor module and sensor node show feasibility and high performance for indoor presence detection.

6.2. Future Work

Throughout the study, we identify three issues that are critical to further improve the reliability and repeatability of the SLEEPIR sensor system: how to further reduce the fabrication variation of the PDLC shutters; how to reduce the error when measuring the FTIR spectrums, the response time and the SLEEPIR sensor module's output; how to further improve the presence detection accuracy in a fully uncontrolled environment in the long term.

Firstly, as described in Chapter 4, when preparing the PDLC shutters, there are several sources leading to the measurement error. (1) The uncertainty when moving the mixture with LC, polymer, and chloroform on the Ge substrate could be addressed by improving the speed of operation, considering the chloroform's evaporation rate, and compensating for the volume of the mixture. (2) Using new Ge substrates with a careful cleaning process could ensure the same quality of the substrates. (3) Using glass beads with smaller variations may help to reduce the uncertainty of the cell gap d.

Secondly, there is also measurement error from the FTIR measurement, response time measurement, and PIR output measurement. (1) At each FTIR measurement, the position of the PDLC shutter may differ. In the future, we could design a precise holder to make sure each PDLC shutter will be located at the same position for each measurement. (2) The infrared photodetector that measures the response time is sensitive to electromagnetic disturbance, airflow, and vibration. Using an electromagnetic shielding chamber may help to reduce the noise during the measurement [132]. Another solution is to increase the signal-noise ratio (SNR) using an infrared light source with high power density, such as CO2 lasers [133]. (3) There is noise when we use a microcontroller to read the voltage from the PIR sensor. In the future, choosing a PIR sensor with high sensitivity, designing a noise filtering circuit, and utilizing a separate high-precision ADC converter could help to reduce the measurement error.

Thirdly, several future works improve the performance of the result for the presence detection test. (1) For the uncontrolled test, we could use the temperature of the sensor and the floor surface in addition to the SLEEPIR module's output, which will provide more information between the voltage signal and the temperature. (2) Use automated feature selection tools, such as tsfresh [154], to extract more features for machine learning models. (3) Instead of selecting features, feed the original signal of the SLEEPIR module to a deep learning model to observe more information within the signal than statistical features. (4) Improve the thermal model by considering a more complex setup. The reason is that the furniture has different surface temperatures, emissivity, and

shapes. By collecting the temperature of the furniture, the thermal model could be more accurate.

REFERENCES

[1] T. A. Nguyen and M. Aiello, "Energy intelligent buildings based on user activity: A survey," *Energy and Buildings,* vol. 56, pp. 244-257, 2013.

[2] M. Mysen, J. Rydock, and P. Tjelflaat, "Demand controlled ventilation for office cubicles—can it be profitable?," *Energy and Buildings,* vol. 35, no. 7, pp. 657-662, 2003.

[3] M. A. ul Haq *et al.*, "A review on lighting control technologies in commercial buildings, their performance and affecting factors," *Renewable and Sustainable Energy Reviews,* vol. 33, pp. 268-279, 2014.

[4] N. Li, G. Calis, and B. Becerik-Gerber, "Measuring and monitoring occupancy with an RFID based system for demand-driven HVAC operations," *Automation in Construction,* vol. 24, pp. 89-99, 2012.

[5] T. Labeodan, W. Zeiler, G. Boxem, and Y. Zhao, "Occupancy measurement in commercial office buildings for demand-driven control applications—A survey and detection system evaluation," *Energy and Buildings,* vol. 93, pp. 303-314, 2015.

[6] C. Martani, D. Lee, P. Robinson, R. Britter, and C. Ratti, "ENERNET: Studying the dynamic relationship between building occupancy and energy consumption," *Energy and Buildings,* vol. 47, pp. 584-591, 2012.

[7] R. Whatmore, "Pyroelectric devices and materials," *Reports on Progress in Physics,* vol. 49, no. 12, p. 1335, 1986.

[8] P. Liu, S.-K. Nguang, and A. Partridge, "Occupancy inference using pyroelectric infrared sensors through hidden Markov models," *IEEE Sensors Journal,* vol. 16, no. 4, pp. 1062-1068, 2016.

[9] Y. P. Raykov, E. Ozer, G. Dasika, A. Boukouvalas, and M. A. Little, "Predicting room occupancy with a single passive infrared (PIR) sensor through behavior extraction," in *Proceedings of the 2016 ACM International Joint Conference on Pervasive and Ubiquitous Computing*, Heidelberg, Germany, 2016, pp. 1016-1027: ACM.

[10] R. H. Dodier, G. P. Henze, D. K. Tiller, and X. Guo, "Building occupancy detection through sensor belief networks," *Energy and Buildings,* vol. 38, no. 9, pp. 1033-1043, 2006.

[11] B. Yang and M. Zhang, "Credit-based multiple human location for passive binary pyroelectric infrared sensor tracking system: Free from region partition and classifier," *IEEE Sensors Journal*, vol. 17, no. 1, pp. 37-45, 2017.

[12] H. H. Kim, K. N. Ha, S. Lee, and K. C. Lee, "Resident location-recognition algorithm using a Bayesian classifier in the PIR sensor-based indoor location-aware system," *IEEE Transactions on Systems, Man, and Cybernetics, Part C (Applications and Reviews)*, vol. 39, no. 2, pp. 240-245, 2009.

[13] T. Miyazaki and Y. Kasama, "Multiple human tracking using binary infrared sensors," *Sensors*, vol. 15, no. 6, p. 13459, 2015.

[14] Q. Hao, F. Hu, and Y. Xiao, "Multiple human tracking and identification with wireless distributed pyroelectric sensor systems," *IEEE Systems Journal*, vol. 3, no. 4, pp. 428-439, 2009.

[15] J. Lu, T. Zhang, F. Hu, and Q. Hao, "Preprocessing design in pyroelectric infrared sensor-based human-tracking system: On sensor selection and calibration," *IEEE Transactions on Systems, Man, and Cybernetics: Systems*, vol. 47, no. 2, pp. 263-275, 2017.

[16] P. Zappi, E. Farella, and L. Benini, "Tracking motion direction and distance with pyroelectric IR sensors," *IEEE Sensors Journal*, vol. 10, no. 9, pp. 1486-1494, 2010.

[17] J.-S. Fang, Q. Hao, D. J. Brady, B. D. Guenther, and K. Y. Hsu, "Real-time human identification using a pyroelectric infrared detector array and hidden Markov models," *Optics Express*, vol. 14, no. 15, pp. 6643-6658, 2006.

[18] N. Nassif, "A robust CO2-based demand-controlled ventilation control strategy for multi-zone HVAC systems," *Energy and buildings*, vol. 45, pp. 72-81, 2012.

[19] S. A. Mumma, "Transient occupancy ventilation by monitoring CO2," *ASHRAE IAQ Applications*, vol. 5, no. 1, pp. 21-23, 2004.

[20] X. Guo, D. Tiller, G. Henze, and C. Waters, "The performance of occupancy-based lighting control systems: A review," *Lighting Research & Technology*, vol. 42, no. 4, pp. 415-431, 2010.

[21] S. P. Tarzia, R. P. Dick, P. A. Dinda, and G. Memik, "Sonar-based measurement of user presence and attention," in *Proceedings of the 11th international conference on Ubiquitous computing*, 2009, pp. 89-92: ACM.

[22] V. L. Erickson, S. Achleitner, and A. E. Cerpa, "POEM: Power-efficient occupancy-based energy management system," in *12th International Conference*

on Information Processing in Sensor Networks, IPSN 2013, Philadelphia, PA, United states, 2013, pp. 203-216: Association for Computing Machinery.

[23] D. Liu, X. Guan, Y. Du, and Q. Zhao, "Measuring indoor occupancy in intelligent buildings using the fusion of vision sensors," *Measurement Science and Technology*, vol. 24, no. 7, p. 074023, 2013.

[24] Y. Benezeth, H. Laurent, B. Emile, and C. Rosenberger, "Towards a sensor for detecting human presence and characterizing activity," *Energy and Buildings*, vol. 43, no. 2-3, pp. 305-314, 2011.

[25] A. Tyndall, R. Cardell-Oliver, and A. Keating, "Occupancy estimation using a low-pixel count thermal imager," *IEEE Sensors Journal*, vol. 16, no. 10, pp. 3784-3791, 2016.

[26] O. Vartanian *et al.*, "Architectural design and the brain: effects of ceiling height and perceived enclosure on beauty judgments and approach-avoidance decisions," *Journal of Environmental Psychology*, vol. 41, pp. 10-18, 2015.

[27] P. Klasnja, S. Consolvo, T. Choudhury, R. Beckwith, and J. Hightower, "Exploring privacy concerns about personal sensing," in *International Conference on Pervasive Computing*, 2009, pp. 176-183: Springer Berlin Heidelberg.

[28] T. J. Seebeck, "Ueber die magnetische Polarisation der Metalle und Erze durch Temperatur ‐ Differenz," *Annalen der Physik*, vol. 82, no. 2, pp. 133-160, 1826.

[29] A. Hossain and M. H. Rashid, "Pyroelectric detectors and their applications," *IEEE Transactions on Industry Applications*, vol. 27, no. 5, pp. 824-829, 1991.

[30] F. Aman and C. Anitha, "Motion sensing and image capturing based smart door system on android platform," in *2017 International Conference on Energy, Communication, Data Analytics and Soft Computing (ICECDS)*, 2017, pp. 2346-2350.

[31] B. Kaur, P. K. Pateriya, and M. K. Rai, "An illustration of making a home automation system using Raspberry Pi and PIR sensor," in *2018 International Conference on Intelligent Circuits and Systems (ICICS)*, 2018, pp. 439-444.

[32] P. N. Saranu, G. Abirami, S. Sivakumar, K. M. Ramesh, U. Arul, and J. Seetha, "Theft detection system using PIR sensor," in *2018 4th International Conference on Electrical Energy Systems (ICEES)*, 2018, pp. 656-660.

[33] K. C. Sahoo and U. C. Pati, "IoT based intrusion detection system using PIR sensor," in *2017 2nd IEEE International Conference on Recent Trends in*

Electronics, Information & Communication Technology (RTEICT), 2017, pp. 1641-1645.

[34] L. Yeh, C. Lu, C. Kou, Y. Tseng, and C. Yi, "Autonomous light control by wireless sensor and actuator networks," *IEEE Sensors Journal*, vol. 10, no. 6, pp. 1029-1041, 2010.

[35] M. Feldmeier and J. A. Paradiso, "Personalized HVAC control system," in *2010 Internet of Things (IOT)*, 2010, pp. 1-8.

[36] A. Beltran, V. L. Erickson, and A. E. Cerpa, "ThermoSense: Occupancy thermal based sensing for HVAC control," in *Proceedings of the 5th ACM Workshop on Embedded Systems For Energy-Efficient Buildings*, Roma, Italy, 2013, pp. 1-8, 2528301: ACM.

[37] S. Narayana, R. V. Prasad, V. S. Rao, T. V. Prabhakar, S. S. Kowshik, and M. S. Iyer, "PIR sensors: Characterization and novel localization technique," in *Proceedings of the 14th International Conference on Information Processing in Sensor Networks*, 2015, pp. 142-153: ACM.

[38] K. Seong Jun, V. B. Samoilov, and Y. Yung Sup, "Low-frequency response of pyroelectric sensors," *IEEE Transactions on Ultrasonics, Ferroelectrics, and Frequency Control*, vol. 45, no. 5, pp. 1255-1260, 1998.

[39] J. Steketee, "Spectral emissivity of skin and pericardium," *Physics in Medicine & Biology*, vol. 18, no. 5, p. 686, 1973.

[40] J. D. Hardy, "The radiation of heat from the human body: III. The human skin as a black-body radiator," *Journal of Clinical Investigation*, vol. 13, no. 4, p. 615, 1934.

[41] S. B. Lang, "Pyroelectricity: From ancient curiosity to modern imaging tool," *Physics Today*, vol. 58, no. 8, p. 31, 2005.

[42] L. Wu, F. Gou, S. Wu, and Y. Wang, "SLEEPIR: Synchronized low-energy electronically chopped PIR sensor for true presence detection," *IEEE Sensors Letters*, vol. 4, no. 3, pp. 1-4, 2020.

[43] L. Wu, Y. Wang, and H. Liu, "Occupancy detection and localization by monitoring nonlinear energy flow of a shuttered passive infrared sensor," *IEEE Sensors Journal*, vol. 18, no. 21, pp. 8656-8666, 2018.

[44] L. Wu and Y. Wang, "A low-power electric-mechanical driving approach for true occupancy detection using a ahuttered passive infrared sensor," *IEEE Sensors Journal*, vol. 19, no. 1, pp. 47-57, 2019.

[45] T. Teixeira, G. Dublon, and A. Savvides, "A survey of human-sensing: Methods for detecting presence, count, location, track, and identity," *ACM Computing Surveys,* vol. 5, no. 1, pp. 59-69, 2010.

[46] U. S. B. o. L. Statistics. (2018, Accessed 03/10/2020). *American time use survey*. Available: https://www.bls.gov/tus/home.htm

[47] T. A. Nguyen and M. Aiello, "Beyond indoor presence monitoring with simple sensors," *PECCS*, vol. 2012, pp. 5-14, 2012.

[48] C. Tsai and M.-S. Young, "Pyroelectric infrared sensor-based thermometer for monitoring indoor objects," *Review of Scientific Instruments,* vol. 74, no. 12, pp. 5267-5273, 2003.

[49] D. E. Dausch, S. H. Goodwin-Johansson, G. McGuire, L. D. Kramer, and M. R. Davidson, "Electrostatic flexible film actuators as IR choppers for pyroelectric detectors or microbolometers," in *Aerospace/Defense Sensing, Simulation, and Controls*, 2001, pp. 372-379: International Society for Optics and Photonics.

[50] D. E. Dausch and S. H. Goodwin-Johansson, "Electrostatic MEMS chopper for uncooled IR detectors," in *International Symposium on Optical Science and Technology*, Seattle, WA, 2003, vol. 4820, pp. 261-269: SPIE.

[51] H. Liu, Y. Wang, K. Wang, and H. Lin, "Turning a pyroelectric infrared motion sensor into a high-accuracy presence detector by using a narrow semi-transparent chopper," *Applied Physics Letters,* vol. 111, no. 24, p. 243901, 2017.

[52] P.-G. De Gennes and J. Prost, *The physics of liquid crystals*. Oxford university press, 1993.

[53] R. H. Chen, *Liquid crystal displays: fundamental physics and technology*. John Wiley & Sons, 2011.

[54] L. N. Thibos, X. Qi, and D. T. Miller, "Vision through a liquid-crystal spatial light modulator," in *Adaptive Optics for Industry and Medicine*, pp. 57-62.

[55] D. A. Dunmur, "Electro-Optical Properties of Liquid Crystals," in *Molecular electro-optics: Electro-optic properties of macromolecules and colloids in solution*, S. Krause, Ed. Boston, MA: Springer US, 1981, pp. 435-471.

[56] S. Brugioni and R. Meucci, "Liquid crystal twisted nematic light modulator for the infrared region," *Journal of Optics A: Pure and Applied Optics,* vol. 6, no. 1, pp. 6-9, 2003.

[57] S. Gauza, H. Wang, C.-H. Wen, S.-T. Wu, A. J. Seed, and D. Roman, "High birefringence isothiocyanato tolane liquid crystals," *Japanese Journal of Applied Physics,* vol. 42, no. 6R, p. 3463, 2003.

[58] J. W. Doane, "Polymer dispersed liquid crystal displays," *Liquid Crystals: Applications and Uses,* vol. 1, pp. 361-396, 1990.

[59] J. Doane, A. Golemme, J. L. West, J. Whitehead Jr, and B.-G. Wu, "Polymer dispersed liquid crystals for display application," *Molecular Crystals and Liquid Crystals,* vol. 165, no. 1, pp. 511-532, 1988.

[60] S. T. Wu, U. Efron, and L. D. Hess, "Infrared birefringence of liquid crystals," *Applied Physics Letters,* vol. 44, no. 11, pp. 1033-1035, 1984.

[61] P. Joffre, G. Illiaquer, and J.-P. Huignard, "Electro-optic properties of nematic liquid crystals for phase modulation in the infrared 10.6 μm," in *Electro-Optic and Magneto-Optic Materials and Applications,* 1989, vol. 1126, pp. 13-21: International Society for Optics and Photonics.

[62] F. Peng *et al.*, "Low absorption chlorinated liquid crystals for infrared applications," *Optical Materials Express,* vol. 5, no. 6, pp. 1281-1288, 2015.

[63] S.-T. Wu, "Infrared properties of nematic liquid crystals: an overview," *Optical Engineering,* vol. 26, no. 2, p. 262120, 1987.

[64] J. Kobayashi, J. Kita, and K. Yoshino, "Application of pyroelectric sensor and IR-chopper with ferroelectric liquid crystal for human detection," *IEEJ Transactions on Sensors and Micromachines,* vol. 117, no. 3, pp. 132-136, 1997.

[65] J. Kobayashi, J. Kita, and K. Yoshino, "A light chopper for infrared detection utilizing ferroelectric liquid crystal," *Electronics and Communications in Japan (Part II: Electronics),* vol. 80, no. 2, pp. 88-97, 1997.

[66] G. J. Choi, H. M. Jung, J. S. Gwag, and S. H. Lee, "Infrared shutter using cholesteric liquid crystal," *Applied Optics,* vol. 55, no. 16, pp. 4436-4440, 2016.

[67] J. W. McCargar, J. W. Doane, J. L. West, and T. W. Anderson, "Polymer-dispersed liquid-crystal shutters for IR imaging," in *Liquid-Crystal Devices and Materials,* 1991, vol. 1455, pp. 54-61: International Society for Optics and Photonics.

[68] J. W. McCargar, R. Ondris-Crawford, and J. L. West, "Polymer dispersed liquid crystal infrared light shutter," *Journal of Electronic Imaging,* vol. 1, no. 1, pp. 22-29, 1992.

[69] H. H. Li, "Refractive index of silicon and germanium and its wavelength and temperature derivatives," *Journal of Physical and Chemical Reference Data,* vol. 9, no. 3, pp. 561-658, 1980.

[70] A. Yazar, F. Erden, and A. E. Cetin, "Multi-sensor ambient assisted living system for fall detection," in *Proceedings of the IEEE International Conference on Acoustics, Speech, and Signal Processing (ICASSP'14)*, 2014, pp. 1-3.

[71] M. Moghavvemi and L. C. Seng, "Pyroelectric infrared sensor for intruder detection," in *2004 IEEE Region 10 Conference TENCON 2004.*, 2004, vol. 4, pp. 656-659.

[72] I. Lienhard and H. John, *A heat transfer textbook*. Phlogiston press, 2005.

[73] InfraTec. (Accessed 3/1/2021). *Basic principles of pyroelectric detectors*. Available: https://www.infratec-infrared.com/downloads/en/sensor-division/application-notes/infratec-application-notes-basics.pdf

[74] R. O. S. Juan, J. S. Kim, Y. H. Sa, H. S. Kim, and H. W. Cha, "Development of a sensing module for standing and moving human body using a shutter and PIR sensor," *International Journal of Multimedia and Ubiquitous Engineering,* vol. 11, no. 7, pp. 47-56, 2016.

[75] R. O. Duda, P. E. Hart, and D. G. Stork, *Pattern classification*. John Wiley & Sons, 2012.

[76] C. J. Burges, "A tutorial on support vector machines for pattern recognition," *Data Mining and Knowledge Discovery,* vol. 2, no. 2, pp. 121-167, 1998.

[77] T. Cover and P. Hart, "Nearest neighbor pattern classification," *IEEE Transactions on Information Theory,* vol. 13, no. 1, pp. 21-27, 1967.

[78] J. R. Quinlan, "Induction of decision trees," *Machine Learning,* vol. 1, no. 1, pp. 81-106, 1986.

[79] F. Pedregosa *et al.*, "Scikit-learn: Machine learning in Python," *Journal of Machine Learning Research,* vol. 12, no. Oct, pp. 2825-2830, 2011.

[80] E. Klein, "Step-by-step motor unit," Patent U.S. Patent No. 4,550,279, 1985.

[81] M. Duarte and R. N. Watanabe. (2021, Accessed 4/1/2021). *Notes on scientific computing for biomechanics and motor control*. Available: http://doi.org/10.5281/zenodo.4599319

[82] R. S. Rakibe and B. D. Patil, "Background subtraction algorithm based human motion detection," *International Journal of Scientific and Research Publications,* vol. 3, no. 5, pp. 2250-3153, 2013.

[83] J. Fergason, "Display devices utilizing liquid crystal light modulation," US Patent 3,731,986, May 8, 1973, 1973.

[84] S. T. Wu, U. Efron, and L. D. Hess, "Optical rotatory power of 90° twisted nematic liquid crystals," *Applied Physics Letters,* vol. 44, no. 9, pp. 842-844, 1984.

[85] M. Schadt, "Liquid crystal materials and liquid crystal displays," *Annual Review of Materials Science,* vol. 27, no. 1, pp. 305-379, 1997.

[86] B. Bahadur, "A brief review of histoty, present status, developments and market overview of liquid crystal displays," *Molecular Crystals and Liquid Crystals,* vol. 99, no. 1, pp. 345-374, 1983.

[87] B. Bahadur, "Liquid crystal displays," *Molecular Crystals and Liquid Crystals,* vol. 109, no. 1, pp. 3-93, 1984.

[88] K. Yoshino and M. Ozaki, "New electro-optic effect of microsecond response utilizing transient light scattering in ferroelectric liquid crystal," *Japanese Journal of Applied Physics,* vol. 23, no. Part 2, No. 6, pp. L385-L387, 1984.

[89] Q. Guo, K. Yan, V. Chigrinov, H. Zhao, and M. Tribelsky, "Ferroelectric liquid crystals: physics and applications," *Crystals,* vol. 9, no. 9, p. 470, 2019.

[90] F. Du, Y.-q. Lu, H.-w. Ren, S. Gauza, and S.-T. Wu, "Polymer-stabilized cholesteric liquid crystal for polarization-independent variable optical attenuator," *Japanese Journal of Applied Physics,* vol. 43, no. 10, pp. 7083-7086, 2004.

[91] K.-H. Kim, H.-J. Jin, K.-H. Park, J.-H. Lee, J. C. Kim, and T.-H. Yoon, "Long-pitch cholesteric liquid crystal cell for switchable achromatic reflection," *Optics Express,* vol. 18, no. 16, pp. 16745-16750, 2010.

[92] N. Tamaoki, "Cholesteric liquid crystals for color information technology," *Advanced Materials,* vol. 13, no. 15, pp. 1135-1147, 2001.

[93] S. Bronnikov, S. Kostromin, and V. Zuev, "Polymer-dispersed liquid crystals: progress in preparation, investigation, and application," *Journal of Macromolecular Science, Part B,* vol. 52, no. 12, pp. 1718-1735, 2013.

[94] A. K. Jain and R. R. Deshmukh, "An overview of polymer-dispersed liquid crystals composite films and their applications," *Liquid Crystals Display Technology,* 2020.

[95] J. W. Doane, N. A. Vaz, B. G. Wu, and S. Žumer, "Field controlled light scattering from nematic microdroplets," *Applied Physics Letters,* vol. 48, no. 4, pp. 269-271, 1986.

[96] L. Wu and Y. Wang, "True presence detection via passive infrared sensor network using liquid crystal infrared shutters," in *Proceedings of the ASME 2020 Conference on Smart Materials, Adaptive Structures and Intelligent Systems*, 2020.

[97] J. T. Cox and G. Hass, "Antireflection coatings for germanium and silicon in the infrared*," *Journal of the Optical Society of America,* vol. 48, no. 10, pp. 677-680, 1958.

[98] A. Ghosh, P. Kant, P. K. Bandyopadhyay, P. Chandra, and O. P. Nijhawan, "Antireflection coating on germanium for dual channel (3–5 and 7.5–10.6 μm) thermal imagers," *Infrared Physics & Technology,* vol. 40, no. 1, pp. 49-53, 1999.

[99] J. Li, S.-T. Wu, S. Brugioni, R. Meucci, and S. Faetti, "Infrared refractive indices of liquid crystals," *Journal of Applied Physics,* vol. 97, no. 7, p. 073501, 2005.

[100] G. P. Montgomery Jr, J. L. West, and W. Tamura‐Lis, "Light scattering from polymer‐dispersed liquid crystal films: Droplet size effects," *Journal of Applied Physics,* vol. 69, no. 3, pp. 1605-1612, 1991.

[101] J. Kelly, W. Wu, and P. Palffy-muhoray, "Wavelength dependence of scattering in PDLC films: droplet size effects," *Molecular Crystals and Liquid Crystals Science and Technology. Section A. Molecular Crystals and Liquid Crystals,* vol. 223, no. 1, pp. 251-261, 1992.

[102] J. L. West, "Phase separation of liquid crystals in polymers," *Molecular Crystals and Liquid Crystals Incorporating Nonlinear Optics,* vol. 157, no. 1, pp. 427-441, 1988.

[103] P. S. Drzaic, *Liquid crystal dispersions* (Series on Liquid Crystals). World Scientific, 1995.

[104] S. Perlmutter, D. Doroski, and G. Moddel, "Degradation of liquid crystal device performance due to selective adsorption of ions," *Applied physics letters,* vol. 69, no. 9, pp. 1182-1184, 1996.

[105] M. Lee, R. Guo, and A. S. Bhalla, "Pyroelectric sensors," *Journal of electroceramics,* vol. 2, no. 4, pp. 229-242, 1998.

[106] J. Fraden, *Handbook of modern sensors*. Springer, 2010.

[107] O. Faix, "Fourier transform infrared spectroscopy," in *Methods in Lignin Chemistry*, S. Y. Lin and C. W. Dence, Eds. Berlin, Heidelberg: Springer Berlin Heidelberg, 1992, pp. 83-109.

[108] W. Perkins, "Fourier transform-infrared spectroscopy: Part l. Instrumentation," *Journal of Chemical Education*, vol. 63, no. 1, p. A5, 1986.

[109] R. H. Kingston, *Detection of optical and infrared radiation*. Springer, 2013.

[110] A. K. Kalkar and V. V. Kunte, "Electro-optical studies on polymer dispersed liquid crystal composite films. II. Composite of PVB/E44 and PMMABA/E44," *Molecular Crystals and Liquid Crystals*, vol. 383, no. 1, pp. 1-25, 2002.

[111] M. Malik, P. Bhatia, and R. Deshmukh, "Effect of nematic liquid crystals on optical properties of solvent induced phase separated PDLC composite films," *Indian Journal of Science and Technology*, vol. 5, pp. 3440-3452, 2012.

[112] P. S. Drzaic, "Reorientation dynamics of polymer dispersed nematic liquid crystal films," *Liquid Crystals*, vol. 3, no. 11, pp. 1543-1559, 1988.

[113] R. R. Deshmukh and M. K. Malik, "Effect of temperature on the optical and electro-optical properties of poly(methyl methacrylate)/E7 polymer-dispersed liquid crystal composites," *Journal of applied polymer science*, vol. 109, no. 1, pp. 627-637, 2008.

[114] F. Sanchez-Marin, S. Calixto-Carrera, and C. Villaseñor-Mora, "Novel approach to assess the emissivity of the human skin," *Journal of Biomedical Optics*, vol. 14, no. 2, p. 024006, 2009.

[115] D. Mitchell, C. H. Wyndham, T. Hodgson, and F. R. N. Nabarro, "Measurement of the Total Normal Emissivity of Skin Without The Need For Measuring Skin Temperature," *Physics in Medicine and Biology*, vol. 12, no. 3, pp. 359-366, 1967.

[116] S. Jain and D. Rout, "Electro‐optic response of polymer dispersed liquid‐crystal films," *Journal of Applied Physics*, vol. 70, no. 11, pp. 6988-6992, 1991.

[117] R. R. Deshmukh, "Electro-optic and dielectric responses in PDLC composite systems," in *Liquid Crystalline Polymers: Volume 2--Processing and Applications*, V. K. Thakur and M. R. Kessler, Eds. Cham: Springer International Publishing, 2015, pp. 169-195.

[118] J. He, B. Yan, B. Yu, S. Wang, Y. Zeng, and Y. Wang, "The effect of molecular weight of polymer matrix on properties of polymer-dispersed liquid crystals," *European Polymer Journal*, vol. 43, no. 6, pp. 2745-2749, 2007.

[119] W. Li, Y. Cao, H. Cao, M. Kashima, L. Kong, and H. Yang, "Effects of the structures of polymerizable monomers on the electro-optical properties of UV cured polymer dispersed liquid crystal films," *Journal of Polymer Science Part B: Polymer Physics*, vol. 46, no. 13, pp. 1369-1375, 2008.

[120] F. Liu, H. Cao, Q. Mao, P. Song, and H. Yang, "Effects of monomer structure on the morphology of polymer networks and the electro-optical properties of polymer-dispersed liquid crystal films," *Liquid Crystals*, vol. 39, no. 4, pp. 419-424, 2012.

[121] Y. Lu, J. Wei, Y. Shi, O. Jin, and J. Guo, "Effects of fabrication condition on the network morphology and electro-optical characteristics of polymer-dispersed bistable smectic A liquid crystal device," *Liquid Crystals*, vol. 40, no. 5, pp. 581-588, 2013.

[122] M. Mizuhashi, "Electrical properties of vacuum-deposited indium oxide and indium tin oxide films," *Thin Solid Films*, vol. 70, no. 1, pp. 91-100, 1980.

[123] X. W. Sun, H. C. Huang, and H. S. Kwok, "On the initial growth of indium tin oxide on glass," *Applied Physics Letters*, vol. 68, no. 19, pp. 2663-2665, 1996.

[124] L. Bouteiller and P. L. Barny, "Polymer-dispersed liquid crystals: Preparation, operation and application," *Liquid Crystals*, vol. 21, no. 2, pp. 157-174, 1996.

[125] A. Sawada, K. Tarumi, and S. Naemura, "Novel characterization method of ions in liquid crystal materials by complex dielectric constant measurements," *Japanese Journal of Applied Physics*, vol. 38, no. 3R, p. 1423, 1999.

[126] P. S. Drzaic, "Droplet density, droplet size, and wavelength effects in PDLC light scattering," *Molecular Crystals and Liquid Crystals Science and Technology. Section A. Molecular Crystals and Liquid Crystals*, vol. 261, no. 1, pp. 383-392, 1995.

[127] R. R. Deshmukh and M. K. Malik, "Effects of the composition and nematic–isotropic phase transition on the electro-optical responses of unaligned polymer-dispersed liquid crystals. I. Composites of poly(methyl methacrylate) and E8," *Journal of Applied Polymer Science*, vol. 108, no. 5, pp. 3063-3072, 2008.

[128] F. Yamagishi, L. Miller, and C. van Ast, "Morphological control In polymer-dispersed liquid crystal film matrices," in *Proceedings SPIE, Liquid Crystal Chemistry, Physics, and Applications*, 1989, vol. 1080: SPIE.

[129] R. Yamaguchi and S. Sato, "Highly transparent memory states by phase transition with a field in polymer dispersed liquid crystal films," *Japanese Journal of Applied Physics*, vol. 31, no. Part 2, No. 3A, pp. L254-L256, 1992.

[130] B.-G. Wu, J. H. Erdmann, and J. W. Doane, "Response times and voltages for PDLC light shutters," *Liquid Crystals,* vol. 5, no. 5, pp. 1453-1465, 1989.

[131] S. Park and J. W. Hong, "Polymer dispersed liquid crystal film for variable-transparency glazing," *Thin Solid Films,* vol. 517, no. 10, pp. 3183-3186, 2009.

[132] J. Dřínovský and Z. Kejik, "Electromagnetic shielding efficiency measurement of composite materials," *Measurement Science Review,* vol. 9, no. 4, pp. 109-112, 2009.

[133] T. A. S. Srinivas, P. J. Timans, R. J. Butcher, and H. Ahmed, "Room‐temperature CO2 laser radiation detector," *Applied Physics Letters,* vol. 59, no. 13, pp. 1529-1531, 1991.

[134] N. J. Crawford, M. D. Dadmun, T. J. Bunning, and L. V. Natarajan, "Time-resolved light scattering of the phase separation in polymer-dispersed liquid crystals formed by photo-polymerization induced phase separation," *Polymer,* vol. 47, no. 18, pp. 6311-6321, 2006.

[135] S. A. Bulgakova *et al.*, "Influence of the composition of the polymer matrix on the electrooptical properties of films with a dispersed liquid crystal," *Russian Journal of Applied Chemistry,* vol. 81, no. 8, p. 1446, 2008.

[136] P. Emrath. (2019, Accessed 5/22/2020). *Spaces in new homes*. Available: https://nahbclassic.org/generic.aspx?genericContentID=216616

[137] L. Wu and Y. Wang, "Stationary and moving occupancy detection using the SLEEPIR sensor module and machine learning," *IEEE Sensors Journal,* pp. 1-1, 2021.

[138] M. Janidarmian, A. Roshan Fekr, K. Radecka, and Z. Zilic, "A comprehensive analysis on wearable acceleration sensors in human activity recognition," *Sensors,* vol. 17, no. 3, p. 529, 2017.

[139] I. Guyon, J. Weston, S. Barnhill, and V. Vapnik, "Gene selection for cancer classification using support vector machines," *Machine Learning,* vol. 46, no. 1, pp. 389-422, 2002.

[140] P. M. Granitto, C. Furlanello, F. Biasioli, and F. Gasperi, "Recursive feature elimination with random forest for PTR-MS analysis of agroindustrial products," *Chemometrics and Intelligent Laboratory Systems,* vol. 83, no. 2, pp. 83-90, 2006.

[141] M. Pal, "Random forest classifier for remote sensing classification," *International Journal of Remote Sensing,* vol. 26, no. 1, pp. 217-222, 2005.

[142] T. Hastie, R. Tibshirani, and J. Friedman, *The elements of statistical learning: data mining, inference, and prediction*. Springer Science & Business Media, 2009.

[143] I. Rish, "An empirical study of the naive Bayes classifier," in *IJCAI 2001 Workshop on Empirical Methods in Artificial Intelligence*, 2001, vol. 3, no. 22, pp. 41-46.

[144] W. Cui, G. Cao, J. H. Park, Q. Ouyang, and Y. Zhu, "Influence of indoor air temperature on human thermal comfort, motivation and performance," *Building and Environment,* vol. 68, pp. 114-122, 2013.

[145] R. D. Pepler, "Temperature and learning: an experimental study," *ASHRAE Transactions,* vol. 74, no. 2, pp. 211-224, 1968.

[146] S.-i. Tanabe, N. Nishihara, and M. Haneda, "Performance evaluation measures for workplace productivity," in *6th International Conference on Indoor Air Quality, Ventilation and Energy Conservation in Buildings: Sustainable Built Environment*, 2007, pp. 663-670.

[147] B. W. Olesen, "Radiant floor heating in theory and practice," *ASHRAE Journal,* vol. 44, no. 7, pp. 19-26, 2002.

[148] C. Isaksson and F. Karlsson, "Indoor climate in low-energy houses—an interdisciplinary investigation," *Building and Environment,* vol. 41, no. 12, pp. 1678-1690, 2006.

[149] K. Kobayashi, M. Tsukahara, A. Tokumasu, K. Okuyama, K. Saitou, and Y. Nakauchi, "Ambient intelligence for energy conservation," in *2011 IEEE/SICE International Symposium on System Integration (SII)*, 2011, pp. 375-380.

[150] A. D. Paola, M. Ortolani, G. L. Re, G. Anastasi, and S. K. Das, "Intelligent management systems for energy efficiency in buildings: A survey," *ACM Computing Surveys*, vol. 47, no. 1, p. Article 13, 2014.

[151] B. Huchuk, S. Sanner, and W. O'Brien, "Comparison of machine learning models for occupancy prediction in residential buildings using connected thermostat data," *Building and Environment,* vol. 160, p. 106177, 2019.

[152] S. Engelhardt, P. Papacosta, F. Rathe, J. Özen, J. A. Jansen, and R. Junker, "Annual failure rates and marginal bone-level changes of immediate compared to conventional loading of dental implants. A systematic review of the literature and meta-analysis," *Clinical Oral Implants Research,* vol. 26, no. 6, pp. 671-687, 2015.

[153] S. Shah and J. G. Elerath, "Reliability analysis of disk drive failure mechanisms," in *Annual Reliability and Maintainability Symposium, 2005. Proceedings.*, 2005, pp. 226-231.

[154] M. Christ, N. Braun, J. Neuffer, and A. W. Kempa-Liehr, "Time series feature extraction on basis of scalable hypothesis tests (tsfresh – A Python package)," *Neurocomputing*, vol. 307, pp. 72-77, 2018.